Application of Raman and surface enhanced Raman spectroscopy in probing biomolecular interactions

A Thesis
Submitted for the Degree of
DOCTOR OF PHILOSOPHY

by

SOUMIK SIDDHANTA

CHEMISTRY AND PHYSICS OF MATERIALS UNIT
JAWAHARLAL NEHRU CENTRE FOR ADVANCED SCIENTIFIC RESEARCH
(A Deemed University)
Bangalore – 560 064

JULY 2014

DECLARATION

I hereby declare that the matter embodied in the thesis entitled "**Application of Raman and surface enhanced Raman spectroscopy in probing biomolecular interactions**" is the result of investigations carried out by me at the Chemistry and Physics of Materials Unit, Jawaharlal Nehru Centre for Advanced Scientific Research, Bangalore, India under the supervision of Prof. Chandrabhas Narayana and that it has not been submitted elsewhere for the award of any degree or diploma.

In keeping with the general practice in reporting scientific observations, due acknowledgment has been made whenever the work described is based on the findings of other investigators.

Soumik Siddhanta

CERTIFICATE

I hereby certify that the matter embodied in this thesis entitled "**Application of Raman and surface enhanced Raman spectroscopy in probing biomolecular interactions**" has been carried out by Mr. Soumik Siddhanta at the Chemistry and Physics of Materials Unit, Jawaharlal Nehru Centre for Advanced Scientific Research, Bangalore, India under my supervision and that it has not been submitted elsewhere for the award of any degree or diploma.

Prof. Chandrabhas Narayana
(Research Supervisor)

Acknowledgments

My journey as a PhD student has been influenced by many people who have made the past few years of my life so memorable.

I would like to thank my guide Prof. Chandrabhas for all the support and encouragement. I am grateful to him for providing me enormous freedom at workplace. I also admire his openness, willingness to discuss new ideas and also his precious advice in science as well as in life in general.

I would like to acknowledge Prof. C. N. R. Rao for being a huge source of inspiration. I feel very fortunate to be able to listen to his inspirational talks.

It has been a pleasure to collaborate with Prof. Tapas K. Kundu. I am thankful for his constant encouragement and support. I also thank Dr. Karthigeyan for being so helpful in every aspect in the kinase work.

I would also like to acknowledge my collaborators Prof. Shivaprasad, Prof. Kulkarni, Dr. Maji, Prof. Ranga, Prof. Sanyal, Dr. Sudip, Dr. Jayaprakash, Dr. Minu Mathen, Prof. Harish, Gangaiah, Dr. Ritu, Dr. Sathya Perumal, Prof. Hans Agren, Varun and Gangaiah. It has been a pleasure to work and learn from them.

I thank all my teachers in JNC, Prof. Bala, Prof. Kulkarni, Dr. Maji, Prof. Eswaramoorthy, Prof. Waghmare, Prof. Sundaresan, Prof. Narayan, Prof. Pati, Prof. Shobhana, Prof. Shivaprasad, Prof. Ranganathan, Dr. Vidyadhiraja, Dr. Subi George, Dr. Govindaraju for their valuable courseworks and guidance.

I would like thank Integrated PhD coordinators Prof. Bala and Prof. Kulkarni.

The technical staff in JNC have been very helpful. Special thanks to Vasu and Usha madam. I would also like to thank all the admin and support staff of JNC.

I learnt a lot from my labmates Dr. Gopal, Dr. Pavan, Dr. Kavitha, Partha, Srinu, Gayatri, Dhanya, Shantanu, Rajaji, Jyoti, Dr. Sorb, Dr. Dipti, Dr. Santosh, the summer students I have mentored and the lab visitors. I thank them for the good time we had in lab and for their help.

I have gained more than just a PhD here in JNC. I have made friends who are dear to me. Special thanks to my Int. PhD 2007 batchmates Abhay, Ritu, Nitesh, Urmi, Piyush, Bivas, Nisha and Vini. I was fortunate enough to have practiced music with many talented people. Thanks to Subhroda, Anshuman, Adina, Nisha, Sairam, Manohar, Monojit, Piyush, Arpit, Jithesh and many others. It has been a pleasure to have performed together so many times. I also thank all my friends in JNC who have made my stay pleasurable.

I would like to thank BASF for sponsoring my trip to the BASF industries and hosting me in Ludwigshafen, Germany. I would also like to acknowledge the ESONN committee for providing me an opportunity to attend the summer school in Grenoble, France. Both these trips have been great learning experiences for me.

I am deeply thankful to my sister Surja for being there and taking great care of me. I thank my family for their encouragement, love and support.

Preface

This thesis shows the utility of vibrational spectroscopy to study biomolecular interactions, including protein-small molecule interactions which have important implications in drug development process and in pharmaceutical industries. The vibrational spectroscopic techniques discussed in the chapters of the thesis are mainly Raman spectroscopy and Surface enhanced Raman spectroscopy (SERS) whose detailed descriptions are given in **Chapter 1** and the details of the experimental techniques and important steps in sample preparation are discussed in **Chapter 2**. This work highlights the importance of these techniques in the field of biology to understand different molecular mechanisms involved when small molecules interact with different kinds of proteins like catalytic proteins as well as fibrous and structural proteins. Although Raman spectroscopy and related techniques like resonance Raman spectroscopy had been used for studying protein-ligand interactions for a long time, the use of SERS is relatively new in this field. Since its discovery in 1977, SERS has been used extensively for trace detection of molecules, biomolecule sensing and characterization. But, it is relatively unexplored in the area of protein-ligand interactions. In this thesis, we use SERS to study the structural aspects of an important member of kinase family of proteins, Aurora kinases (Aurora A and Aurora B) which are oncogenic proteins and are potential targets of anticancer drugs. In **Chapter 3** of the thesis, we analyze the SERS data and attempt to interpret the nature of interaction of the kinase proteins to the plasmonic nanoparticle surfaces and to distinguish between two homologous proteins with similar structures. We use this basic understanding of protein-nanoparticle interactions to study both competitive and non-competitive mode of binding of drug molecules (or inhibitors) with these kinase proteins which forms the **Chapter 4** of this thesis. The SERS based interpretation of protein-drug binding was validated through molecular docking and molecular dynamics simulations using the available crystal structure of the proteins and also biochemical assays. In **chapter 5**, we studied a different family of proteins belonging to transcriptional co-activators, namely p300 whose full length crystal structure is still unknown. Through SERS studies we could detect the structural changes which were responsible for the inhibitory activity of small molecule inhibitors and the results were consistent with the biochemical assays performed. In **Chapter 6**, we study the interaction of small molecules with a different class of proteins, that is, structural proteins found in basement membranes by fourier transformed Raman spectroscopy. We demonstrate the molecular mechanisms behind the mechanical changes which occur when human eye capsules are stained with trypan blue dye. Trypan blue is used for visualization of eye lens capsules during capsulorhexis, prior to the extraction and replacement of cataractous lens in the eye. The dye induced mechanical changes can cause complications in cataract surgery. Through our Raman studies we could find the optimum concentration of the dye and also the exposure time within which there are minimum detectable structural changes and therefore these results have implications in cataract surgery. In **Chapter 7**, we devise a strategy for SERS studies of small protein like Lysozyme, which is known to undergo structural alterations on binding to oppositely charged nanoparticles thus limiting the use of SERS. This involves the use of sugar based molecules which are known to be exceptional protein stabilizers and we use this stabilizing property

to prevent protein aggregation and maintain the protein in folded state even in the presence of nanoparticles, thus facilitating SERS studies. This thesis is concluded with a discussion on the advantages and limitations of SERS. An overview on future prospects of Raman and SERS in biomolecular interaction studies is also included.

Publications

1. *Surface enhanced Raman spectroscopy of Aurora Kinases: direct, ultrasensitive detection of autophosphorylation*
   Soumik Siddhanta, Dhanasekaran karthigeyan, Partha P, Kundu, Tapas K. Kundu and Chandrabhas Narayana
   RSC Advances 3, 4221-4230 (2013).

2. *Napthoquinones Mediated Inhibition of Lysine Acetyltransferase KAT3B/p300, Basis for Non-toxic Inhibitor Synthesis*
   Mohankrishna Dalvoy Vasudevarao, Pushpak Mizhar, Sujata Kumari, Somnath Mandal, **Soumik Siddhanta**, Mahadeva M. M. Swamy, Stephanie kaypee, Ravindra C. Kodihalli, Amrita Bannerjee, Chandrabhas Narayana, Dipak Dasgupta and Tapas K. Kundu
   The Journal of Biological Chemistry (2014), doi: 10.1074/jbc.M113.486522.

3. *SERS and MD Simulation studies of a specific inhibitor for Aurora Kinase A shows the emergence of a potential drug discovery tool.*
   Dhanasekaran Karthigeyan, **Soumik Siddhanta**, Annavarapu Hari Kishore, Sathya S R R Perumal, Hans A Agren, Surabhi Sudevan, Akshay V. Bhat, Karanam Balasubramanyam, Rangappa Kanchugarakoppal Subbegowda, Tapas K Kundu and Chandrabhas Narayana

Proceedings of National Academy of Sciences, USA. doi: 10.1073/pnas.1402695111.

4. *Trypan blue induced structural alterations of the human anterior lens capsule of cataractous lens: A Raman spectroscopic investigation*

   Soumik Siddhanta, Minu M. Mathen, Mathew Kurian and Chandrabhas Narayana

   (Manuscript under preparation).

5. *Effect of trehalose on protein-nanoparticle interaction*

   Soumik Siddhanta and Chandrabhas Narayana

   (Manuscript under preparation).

6. *Surface Enhanced Raman Spectroscopy of Proteins: Implications in Drug Designing*

   Soumik Siddhanta and Chandrabhas Narayana.

   Nanomaterials and Nanotechnology 2, 1-13 (2012).

7. *Analysis of Protein Acetyltransferase Structure-Function Relation by Surface-Enhanced Raman Scattering (SERS): A Tool to Screen and Characterize Small Molecule Modulators.*

   Mohammed Arif, Dhanasekaran Karthigeyan, **Soumik Siddhanta**, G. V. Pavan Kumar, Chandrabhas Narayana and Tapas .K. Kundu

   Methods in Molecular Biology 981, 239-26 (2013)

Other miscellaneous publications:

1. *Universal Metal-Semiconductor Hybrid Nanostructured SERS Substrate for Biosensing*

   Soumik Siddhanta, Varun Thakur, Chandrabhas Narayana and S. M. Shivaprasad

   ACS Applied Materials and Interfaces, 4, 5807-5812 (2012).

2. *Facile and Green Synthesis of SERS Active and Ferromagnetic Silver Nanorods*

   Sudip Mohapatra, **Soumik Siddhanta**, D. Ravinder Kumar, Chandrabhas Narayana and Tapas Kumar Maji

   European Journal of Inorganic Chemistry, 31, 4969-4974 (2010).

3. *Superparamagnetic nanoparticle based platforms for genomic DNA extraction*

   Soumik Siddhanta, Manasa N., Sumana Bhat, Jayprakash Targolli and Chandrabhas Narayana

   (Manuscript under preparation).

4. *Nanocrystalline Ag microflowers as versatile SERS platform*

   Gangaiah Mettela, **Soumik Siddhanta**, Chandrabhas Narayana and G. U. Kulkarni

   Nanoscale (2014), doi: 10.1039/c4nr01120a.

5. *Nanohole arrays as SERS substrates*

   Ritu Gupta, Gangaiah Mettela, **Soumik Siddhanta**, Chandrabhas Narayana and G. U. Kulkarni

   (Manuscript under preparation).

6. *Spectroscopic studies on interaction of Amlodipine and Nimodipine with serum albumins*

Soumik Siddhanta, Shantanu Aggarwal, Sathya S. R. R. Perumal, Dhanasekaran Karthigeyan, Tapas K. Kundu and Chandrabhas Narayana
(Manuscript under preparation).

7. *Thermally stable plasmonic nanocermets sputtered on micro-engineered surfaces as versatile SERS substrates for multi-analyte detection*
Nitant Gupta, Disha Gupta, Shantanu Aggarwal, **Soumik Siddhanta**, Chandrabhas Narayana and Harish C. Barshilia
(Manuscript under preparation).

Contents

3 SERS studies on Aurora A and Aurora B kinases 35

CHAPTER 1

INTRODUCTION

Historically, light scattering by small particles and related discussions can be traced back to the era of Leonardo da Vinci. He correctly predicted that the blue color of the sky was due to light scattered off macroparticles in the atmosphere consisting of dust, water droplets or ice crystals. Subsequently, scattering of light from suspensions of transparent fluids was studied by Leroy Tyndall. In 1873 Maxwell postulated that the scattered radiation carries information about the molecule's properties and the molecule itself acts as the scattering center. Shortly later, Lord Rayleigh theoretically analyzed the scattering of light from suspended particles [1]. In 1923, the existence of inelastic or frequency modified light scattering was reported by Smekal through his theoretical work [2]. The experimental verification of this phenomenon was given by C. V. Raman in 1928. For this discovery he was awarded the Nobel prize. This phenomenon was also independently observed and proven by Landsberg and Mendelstam [3; 4]. This shift of frequency of scattered light from molecules is known as Raman effect [5].

Raman spectroscopy is based on Raman effect and is a type of molecular spectroscopy. There are several molecular spectroscopic techniques. They deal with scattering, emission or absorption of electromagnetic radiation. All these techniques have undergone huge developments due to the advancements in optical instrumentation, laser technology and nanosciences in the last few decades. Molecular spectroscopy can be classified into electronic, vibrational or rotational depending upon the energy scales probed. In electronic spectroscopy, the electronic energy states of a molecule are probed by ultraviolet or visible radiation. Vibrational spectroscopy deals with the probing of the vibrational energy states lying coupled in between the electronic energy states by inelastic Raman scattering or by infrared radiation. The rotational energy states which are concurrent with the vibrational energy states can be probed by microwave radiation. The development of lasers has provided a source of highly monochromatic light source with a high degree of spatial and temporal coherence and have lead to the increased sensitivity and high resolution of these molecular spectroscopic techniques.

Molecular spectroscopy is one of the widely researched fields with a huge range of applications from physical, chemical and biological sciences to astronomy. Of the various spectroscopic techniques used, vibrational spectroscopy has become an effective tool to study the structure and dynamics of molecules in a wide range of environments and phases. Every molecule has a characteristic signature in the vibrational spectrum. This unique spectrum is called the fingerprint of the molecule and is used for molecular sensing, detection and characterization of various functional groups present in the molecule. The two popular vibrational spectroscopic techniques used are Infrared and Raman scattering. In this thesis we will concentrate only on the use of the latter as a molecular probe in the present work.

1.1 Raman scattering

When light interacts with molecules, several pathways exist for the molecules to get excited to higher energy states. After the excitation process, the molecule makes a transition to higher energy states and comes back to the ground state by emitting photons (Figure 1.1). These emitted photons might have the same energy or may lose or gain energy after interaction with the molecules. The type of scattering where there is no change in energy is known as Rayleigh scattering or elastic scattering. In the inelastic scattering process, commonly known as Raman scattering, there is a change in energy of the scattered photons. The Raman scattered photons can be classified as either Stokes or anti-Stokes. The Stokes radiation has lower energy and the anti-Stokes has higher energy than the incident radiation.

In case of Infrared absorption, the photon gets absorbed by the molecule and the molecule undergoes a transition to higher vibrational energy levels. So, in comparison, the Raman scattering is a two-photon process. The incoming radiation induces a dipole due to the polarizability of the molecule. The induced dipole oscillates with the same frequency as the exciting radiation and with modulated frequency due to the effect of molecular vibrations on polarizability. The scattered light thus consists of both Raman as well as Rayleigh scattered photons. The polarizability tensor consists of two cartesian components corresponding to the incident photon and the scattered photon respectively. The two photons are connected by a single coherent event which is a quantum mechanical process. Thus Rayleigh and Raman scattering are different from two one-photon processes of absorption and subsequent emission. In the subsequent sections, the classical and quantum pictures of Raman scattering are discussed in detail.

1.1.1 Classical picture of Raman scattering

The classical approach to Raman scattering is based on the first order of induced electric dipoles. When a molecule is placed in static electric field E, charge

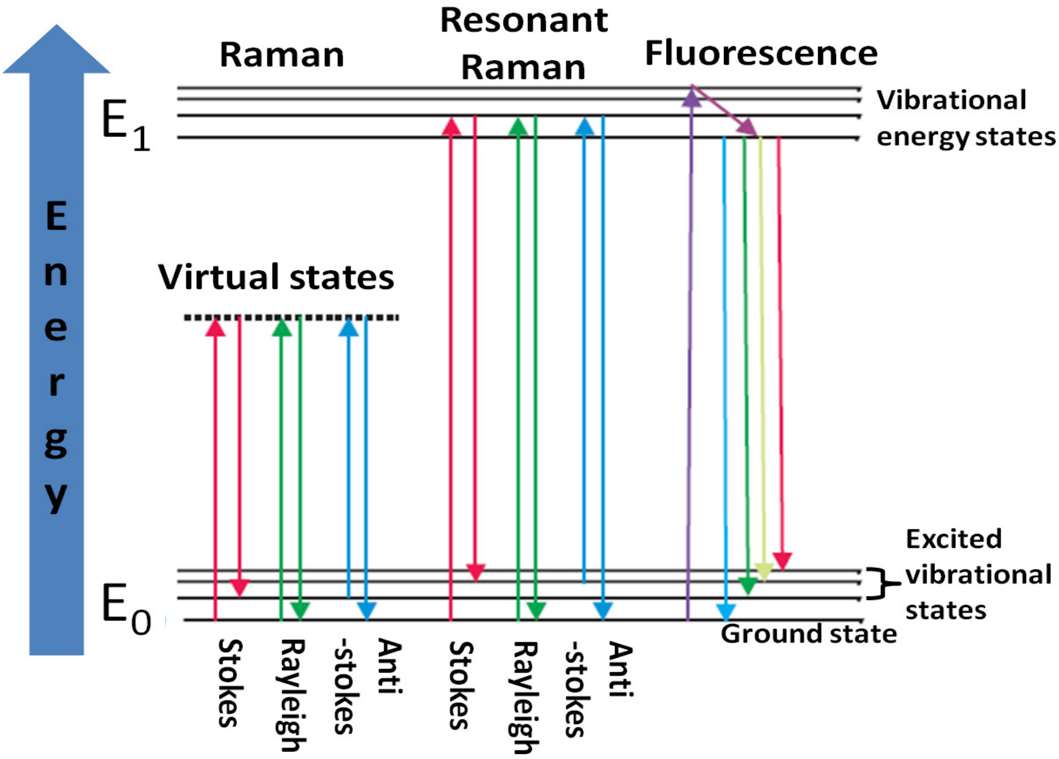

Figure 1.1: Energy level diagram comparing Raman, resonant Raman scattering and Fluorescence

separation happens and positive and negative centers are created due to distortion of the electron cloud. This separation of charges is called the induced dipole moment, p and depends upon the magnitude of the applied external electric field. The molecule is now said to be polarized and the polarization is given by the equation

$$P = \alpha \cdot E; \tag{1.1}$$

where α is the polarizability of the molecule and is denoted by a 3×3 polarizability tensor. This tensor depends on the positions of the nuclei of the atoms with respect to the electron cloud. Thus, it is sensitive to the change in the molecular coordinates. Eq.1.1 can also be represented as follows

$$\begin{bmatrix} p_x \\ p_y \\ p_z \end{bmatrix} = \begin{bmatrix} \alpha_{xx} & \alpha_{xy} & \alpha_{xz} \\ \alpha_{yx} & \alpha_{yy} & \alpha_{yz} \\ \alpha_{zx} & \alpha_{zy} & \alpha_{zz} \end{bmatrix} \begin{bmatrix} E_x \\ E_y \\ E_z \end{bmatrix} \tag{1.2}$$

If the molecule is exposed to a time varying electric field of frequency ν

$$E = E_0 \cos 2\pi\nu t \tag{1.3}$$

then the dipole moment varies as

$$P = \alpha \cdot E = \alpha E_0 \cos 2\pi\nu t \tag{1.4}$$

This dipole oscillation results in Rayleigh scattering and corresponds to elastic scattering. If the molecule has other internal degrees of freedom which changes the polarizability periodically, then the oscillating dipole will be superposition of the varying electric field and the polarizability. These internal degrees of freedom come from the rotation and vibration of the molecules. If the molecule vibrates with a frequency ν_{vib} then, the nuclear displacement q is given by the relation

$$q = q_0 \cos 2\pi\nu_{vib} t \tag{1.5}$$

where q_0 is the amplitude of the vibration. Thus for a small amplitude of vibration, the polarizability can be expressed as a taylor series:

$$\alpha = \alpha_0 \ + (\frac{\partial\alpha}{\partial q})_0 + \cdots \tag{1.6}$$

Therefore, combining the expressions for P, q and α we obtain

$$\begin{aligned} P &= \alpha E_0 \cos 2\pi\nu_0 t \\ &= \alpha_0 E_0 \cos 2\pi\nu_0 t + (\frac{\partial\alpha}{\partial q})_0 q E_0 \cos 2\pi\nu_0 t \\ &= \alpha_0 E_0 \cos 2\pi\nu_0 t + \frac{1}{2}(\frac{\partial\alpha}{\partial q})_0 q_0 E_0 \{\cos 2\pi(\nu_0 + \nu_{vib})t - \cos 2\pi(\nu_0 - \nu_{vib})t\} \end{aligned} \tag{1.7}$$

In the above equation, there are three frequency components, ν_0, $\nu - \nu_{vib}$ and $\nu + \nu_{vib}$. The component ν_0 represents an oscillating dipole responsible for elastic or Rayleigh scattering of the incident light. The components $\nu - \nu_{vib}$ and $\nu + \nu_{vib}$ represent Stokes and anti-Stokes line respectively and are the inelastically scattered components. if $(\frac{\partial\alpha}{\partial q})_0$ is zero, then the vibration is Raman inactive. For a vibration to be Raman-active, the change of polarizability must be non-zero.

1.1.2 Quantum picture of Raman scattering

The classical picture predicts equal intensities for both Stokes and anti-Stokes scattering. But it is observed that Stokes scattering involving loss of energy of the photons give stronger signal than anti-Stokes. The quantum mechanical picture solves this ambiguity and accounts for the intensity ratio of Stokes and anti-Stokes scattering. This quantum mechanical treatment of the two photon Raman scattering process is based on second order perturbation theory derived by Placzek [6] from Kramers and Heisenberg's[7; 8] dispersion theory. The molecule is treated quantum mechanically but the radiation is treated classically. Therefore the molecule undergoes a transition from one vibrational quantum state to another vibrational quantum state with energies E_1 and E_2 respectively. This transition is through a virtual state with the energy E_v. The virtual state is a transition state which does not correspond to an eigenstate of the molecule and is an imaginary state. The electromagnetic radiation perturbs the molecular system and a direct transition is accompanied by emission or absorption of radiation. Such an event happens if the dipole moment of the transition is non-zero. The amplitude of transition from state i to a state f induced by the electromagnetic radiation of frequency ν is given by

$$[\mu]_{fi} = \langle \psi_f | \alpha | \psi_i \rangle \cdot E; \tag{1.8}$$

where ψ_f and ψ_i are the wavefunctions of the initial and the final states respectively. The intensity of Raman scattering depends on the transition polarizability tensor. By ignoring the electrical and mechanical anharmonicity only for non-zero matrix elements, vibrational quantum number changes by unity whereas all other quantum number remains unchanged. Thus, the matrix element of transition polarizability of Stokes scattering is given by

$$[\alpha_{xy}] = b\beta\sqrt{v+1}; \tag{1.9}$$

where v is the vibrational quantum number. The quantum mechanical analog of the amplitude of a classical oscillator given by $b = \hbar/(4\pi c\tilde{\nu})$. For a transition to be Raman active, at least one component of the polarizability tensor should be non-zero. The ratio of intensities of Stokes and anti-Stokes is given by the following equation

$$\frac{I_{Stokes}}{I_{anti-Stokes}} = \left(\frac{\tilde{\nu_0} - \tilde{\nu_k}}{\tilde{\nu_0} + \tilde{\nu_k}}\right)^4 exp\left(\frac{hc\tilde{\nu}}{kT}\right) \tag{1.10}$$

The Raman scattering cross section representing the cross sectional area of the molecule interacting with the incident electomagnetic radiation is given by the equation

$$\sigma(i \to f) = \frac{8\pi\omega_s^4}{9\hbar c^4}\left|\sum_j\left(\frac{\langle\alpha_{ij}\rangle\hat{e}_L\langle\alpha_{jf}\rangle\hat{e}_s}{\omega_{ij}-\omega_L-i\gamma_L}+\frac{\langle\alpha_{ji}\rangle\hat{e}_L\langle\alpha_{jf}\rangle\hat{e}_s}{\omega_{jf}-\omega_L-i\gamma_j}\right)\right|^4; \tag{1.11}$$

where $\hat{e}_L$ and $\hat{e}_s$ are unit vectors, which represents the polarization of the incident laser beam and the scattered light. The sum extends over all molecular levels j with the homogeneous width γ. The initial and final states are connected by two-photon transitions.

1.2 Surface enhanced Raman scattering (SERS)

Surface enhanced Raman spectroscopy (SERS) is a technique to enhance Raman scattering cross-section by bringing a molecule in the vicinity of a plasmonic surface. SERS was first observed on roughened electrodes by Fleischmann et al. [9] and later interpreted by other groups [10; 11]. Plasmonic nanostructures from noble metals like gold, silver and copper exhibits strong SERS enhancements [12]. Even metals like aluminium, lithium and sodium show weaker SERS enhancements [13]. The collective oscillation of electrons on the surface of these materials is known as surface plasmons. When an incident electromagnetic radiation falls on the surface of these materials the surface plasmons are excited. The plasmons come into resonance with the frequency of the incident radiation. This is called the surface plasmon resonance. When the dimensions of these plasmonic metal structures are lesser than the wavelength of light, the excited surface plasmon produces an oscillating dipole. This oscillating dipole creates a local electromagnetic radiation very close to the surface. When a molecule is placed in the proximity of this surface of the nanostructure, it experiences a very intense electromagnetic field due to the resonant plasmons leading to the phenomenon of SERS. Before the discovery of SERS, the use of Raman for characterization of molecules was restricted due to the low scattering cross section of Raman scattering and also masking of the signals by fluorescence. In non-resonant Raman, the cross section is around 10^{-30}cm^2 per molecule. On the other hand, in the case of fluorescence, the cross section is around 10^{-17}cm^2 per molecule [14]. SERS drastically enhances the scattering cross section of a molecule which makes it comparable to florescence [15]. There are two major mechanisms to explain the SERS enhancement. These are electromagnetic and chemical enhancements [16]. Since the Raman scattering intensities are dependent on the product of incident electric field and the polarizability, both have a bearing on the SERS enhancements. The electromagnetic enhancement mechanism involves the enhancement from the local electric field [16]. The chemical enhancement is the result of the enhancement in polarizability of the molecule due to different chemical effects like charge-transfer excited states and formation of resonant intermediates [16]. These two enhancement mechanisms are discussed below.

1.2.1 Electromagnetic enhancement

According to the Drude model, metals can be considered to consist of periodic static positive charges surrounded by a sea of electrons. A momentary displacement of the electrons causes a dipole to be formed. The dipole oscillation has its own characteristic frequency and generates an electric field. When a molecule is placed in the vicinity of this metallic surface, it experiences an enhanced electric field. The resultant electric field experienced by the adsorbed molecule on a spherical metallic surface is given by $E_i = E_0 + E_s$, where E_0 is the incident field and E_s is

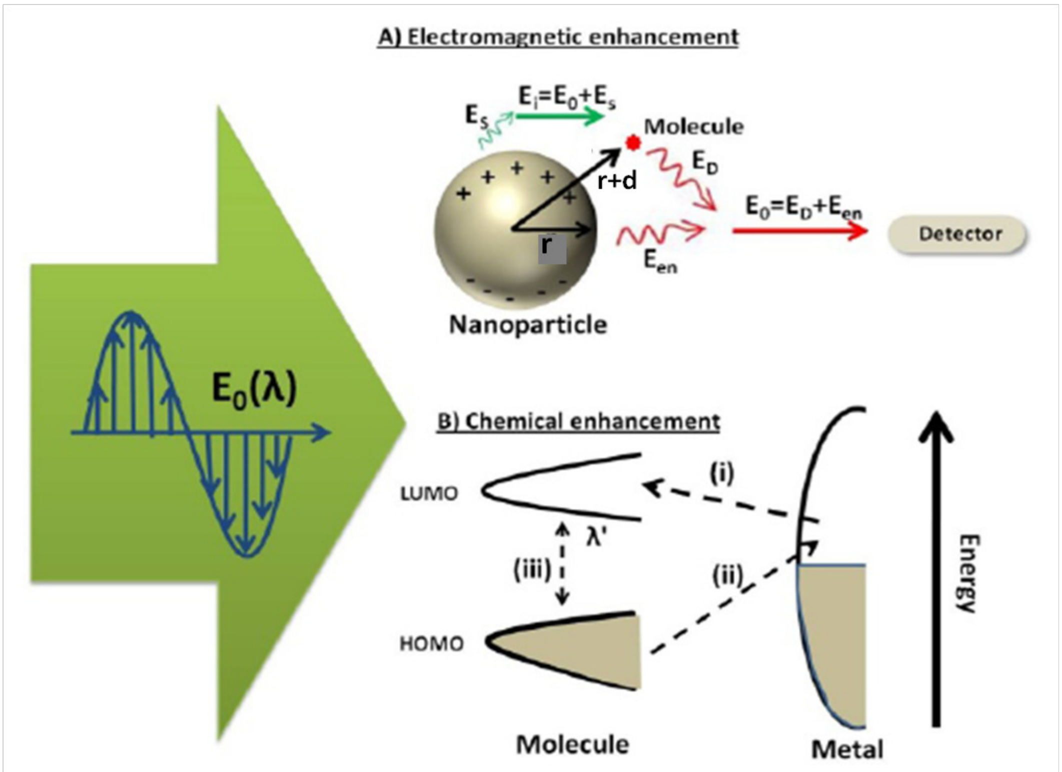

Figure 1.2: The metal nanoparticle experiences a time varying electromagnetic field E_0 which produces an oscillating dipole moment in the nanoparticle. The resultant incoming field is E_i and the resultant outgoing field is E_o. (B) Shows the chemical enhancement mechanism. HOMO and LUMO interact with the metal surface and are broadened into resonances. Charge transfer happens through paths (i) and (ii), and path (iii) shows the resonant Raman process. Figure adapted from [17].

due to the surface plasmon oscillation. E_s depends on the sphere's radius r and the distance d from the molecule (Figure 1.2). It also depends on the dielectric constant ϵ of the metal and the incident field E_0 of the light. Using a Drude model, E_s is given by

$$E_s = \frac{\varepsilon - \varepsilon_0}{\varepsilon + 2\varepsilon_0}\left(\frac{r}{r+d}\right)^3 E_0 \tag{1.12}$$

The resultant electric field E_i induces a dipole μ_i in the molecule. This resultant dipole is directly proportional to the electric field E_i and the polarizability tensor α. As we have seen before, molecular vibrations combine with the oscillating E_i

and produces three kinds of frequencies which are Rayleigh, Stokes and anti-Stokes scattering. In case of Stokes scattering the radiation is red shifted (E_D) and the resulting outgoing field is given by $E_o = E_D + E_{en}$, where E_{en} is the additional component due to the elastic scattering from the dipole in the molecule itself. The field enhancement thus is given by the ratio of the field amplitudes E_i/E_0 and E_o/E_0 for laser and Raman scattered field respectively. The SERS electromagnetic enhancement is the product of the laser and Raman scattered fields

$$G_{SERS} = |A(\nu_L)|^2|A(\nu_S)|^2 = \left|\frac{\varepsilon(\nu_L) - \varepsilon_0}{\varepsilon(\nu_L) + 2\varepsilon_0}\right|^2 \left|\frac{\varepsilon(\nu_S) - \varepsilon_0}{\varepsilon(\nu_S) + 2\varepsilon_0}\right|^2 \left(\frac{r}{r+d}\right)^{12} \tag{1.13}$$

G_{SERS} scales as the fourth power of local field at the vicinity of the metallic nanostructure and is strong when the scattered and plasmon field are in resonance. G_{SERS} is maximum when the real part of $\varepsilon(\nu)$ is equal to $-2\varepsilon_0$ and the imaginary part is negligible. Metals like Ag, Au and Cu satisfy the above conditions at visible wavelengths and therefore, show high SERS enhancements in visible light. The electromagnetic factor accounts for 10^6-10^9 of the total SERS enhancement factor. The enhancement factor also depends upon the specific geometries of the nanostructures or more localized areas with extremely high enhancements. Such localized areas with high SERS enhancements are called "hotspots". Hotspots are formed in the gaps between closely spaced nanostructures and also at sharp tips. Calculations show that the electric field strength in the gap between adjacent particles are a few orders of magnitude higher than that on the surface of an isolated single plasmonic nanoparticle.

1.2.2 Chemical enhancement

Chemical enhancement comes into play when the molecule is in chemical contact (bond formation) with the surface of the metallic nanostructure. It accounts for a factor of 10-100 times towards the total enhancement factor. This value looks small but is significant. When a molecule is in contact with the surface of the metal, an electronic coupling can occur. This charge transfer leads to the broadening and shifting of the electronic level in the molecule resulting in a scenario similar to the resonance Raman effect. This enhances the Raman scattering cross section and thus gives SERS enhancement [16]. The charge transfer takes place when a photon is absorbed by the metal giving rise to a hot electon state. The hot electron undergoes transition to the Lowest Unoccupied Molecular Orbital (LUMO) of the molecule (Figure 1.2 B). The increase in the population in the LUMO electrons leads to the increase in Raman signal due to increased probability of electron-phonon coupling in the Raman scattering tensor. The excited electron then transfers back to the metal from the LUMO of the molecule resulting in the emission of Stokes photons. This is also known as first layer effect and the contact between the metal and the molecule is essential for this enhancement.

1.3 Determination of protein secondary structure

Proteins are complex three dimensional structures made up of basic units known as amino acids. The primary structure of each protein is determined by the sequence of amino acids. The way these amino acid sequences fold through hydrogen bonding is known as secondary structure. The different secondary structures are α helix, β-sheet, turns and random coils. These secondary structure elements connect with each other to form a tertiary structure. In come cases, different polypeptide units of the protein connect to form a functional unit of the protein called the quarternary structure. A definite part of the protein that can fold independently from the rest of the protein is called a domain. Domains are constituted by smaller motiffs which contain specific amino acid sequences. The three dimensional structures of proteins therefore depend on the sequence of the amino acids and how they fold in particular environments. This three-dimensional structure is very significant as it defines the shape as well as the function of the protein.

Determination of the primary sequence of protein is quite straight forward. But obtaining the three dimensional structural information about proteins is a challenging task and requires sophisticated techniques. The most popular technique to determine protein structure as well as protein complexes is x-ray crystallography. It gives the complete three dimensional structure of crystallized proteins. However, one of the major drawback of this technique is the difficulty to crystallize the protein to get a good diffraction pattern. It is never sure if the crystallized proteins are in the active state. It does not provide the solution phase dynamics of the proteins. Another important technique for determination of protein structure is the nuclear magnetic resonance (NMR). NMR can correctly predict the structure of smaller proteins but in case of bigger proteins, it becomes difficult to interpret the data. In recent times, various computer programs are used to determine the structures of proteins by comparing them with the sequences of proteins with known three dimensional structures. It is a theoretical prediction tool and the success of the prediction depends on the goodness of the match between the unknown and known protein sequences.

Other techniques, which provides information about specific structural aspects of the proteins are vibrational , absorption and emission spectroscopy. Vibrational spectroscopic techniques like Raman and IR gives an estimate of the secondary structural elements in the protein. Absorption spectroscopic technique like circular dichroism also provides an estimate of the secondary structure of proteins. Emission spectroscopic techniques like fluorescence provides limited structural information. It provides information about specific residues in proteins and their environments. The vibrational spectroscopic techniques provide detailed molecular information and interactions of the proteins. In this thesis, We will be discussing about the use of Raman spectroscopy for obtaining specific clues to the structural information about proteins.

1.4 Raman spectroscopy of proteins

Since proteins are bulky molecules containing hundreds and thousands of atoms, the vibrational Raman spectrum is very complex with a large number of normal modes. The overlap of various vibrations is supposed to make the extraction of meaningful information from the spectra very tedious if not impossible. However this is not the case as it is always possible to interpret different spectral regions separately. For example, a normal mode of all the repeating units in the protein will appear at one particular position in the spectrum. Information about the structure and environment of amino acid side chains can be obtained. Information about bound ligands as well as the protein backbone can be obtained from the band positions and bandwidths. Thus, Raman spectroscopy can be applied to study proteins of various sizes and in different environments including physiological conditions.

The information obtained from proteins can be divided into three broad categories. These are amino acid sidechains vibrations, protein backbone vibrations and the amide vibrations.

1.4.1 Amino acid side-chain vibrations

The side chain vibrations in proteins come from the highly polarizable aromatic rings of the aromatic amino acids phenylalanine, tyrosine, tryptophan and histidine (Figure 1.3). These aromatic amino acids have characteristic modes which can be used as Raman markers.

The tyrosine Fermi doublet bands at ∼ 830 and ∼ 850 cm^{-1} are one the most useful side chain markers arising due to an interaction between the ring breathing fundamental and the overtone of the C-C-O deformation in para-substituted benzene rings [18]. The relative intensities of these two bands give an idea of the hydrogen bonding condition of the phenol group of the tyrosine residue.

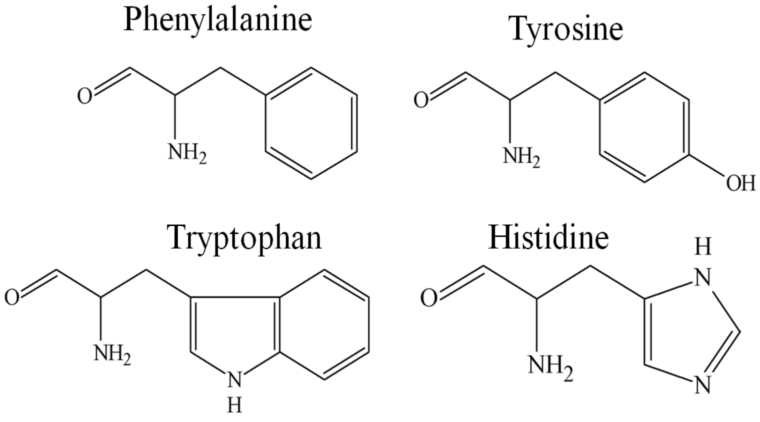

Figure 1.3: Aromatic amino acids

There are 18 bands assigned to the amino acid tryptophan. The majority of these vibrational modes can be assigned to the indole ring. The Fermi doublet of tryptophan is found at 1360 and 1340 cm^{-1}. The relative intensities of these modes give an estimate of the hydrophobicity around the tryptophan residue. The 1010 cm^{-1} band is sensitive to the van der Walls interaction of the phenyl ring with the surrounding residues. Wavenumbers greater than 1020 cm^{-1} indicate stronger van der Waals interactions. The band around 761 cm^{-1} is sensitive to the hydrophobicity of the indole ring environment.

A strong band at around 1000 cm^{-1} corresponds to the ring vibration of phenylalanine which is not sensitive to the conformational changes in protein and is commonly used for the normalization of Raman spectra.

Other significant side chain vibrations come from the amino acid cysteine. The S-S stretching vibrations are found between 510 and 540 cm^{-1} and depend on the conformation of -C-S-S-C-. The C-S stretching frequency lies between 630-670 cm^{-1} and 700-745 cm^{-1} depending on whether the conformation is in gauche form or in the trans form. The alkyl side chains also contribute to the side chain vibrations and are found around 1400-1500 cm^{-1}. The carboxyl group vibrations are found around 900 cm^{-1} and 1400 cm^{-1}.

1.4.2 Amide bands as secondary structure markers

The amide I, II and III are indicative of the protein secondary structures and are combination modes of N-H and C=O vibrations (Figure 1.4). The amide I band is assigned mainly to the C=O stretching vibrations. The amide III band is due to C-N stretching with contribution from N-H bending. The amide II band is not Raman active. The amide I vibration is not affected by the nature of the side-chains. Since it depends only on the secondary structure, it is commonly used for secondary structure analysis. The amide III band has contributions from side-

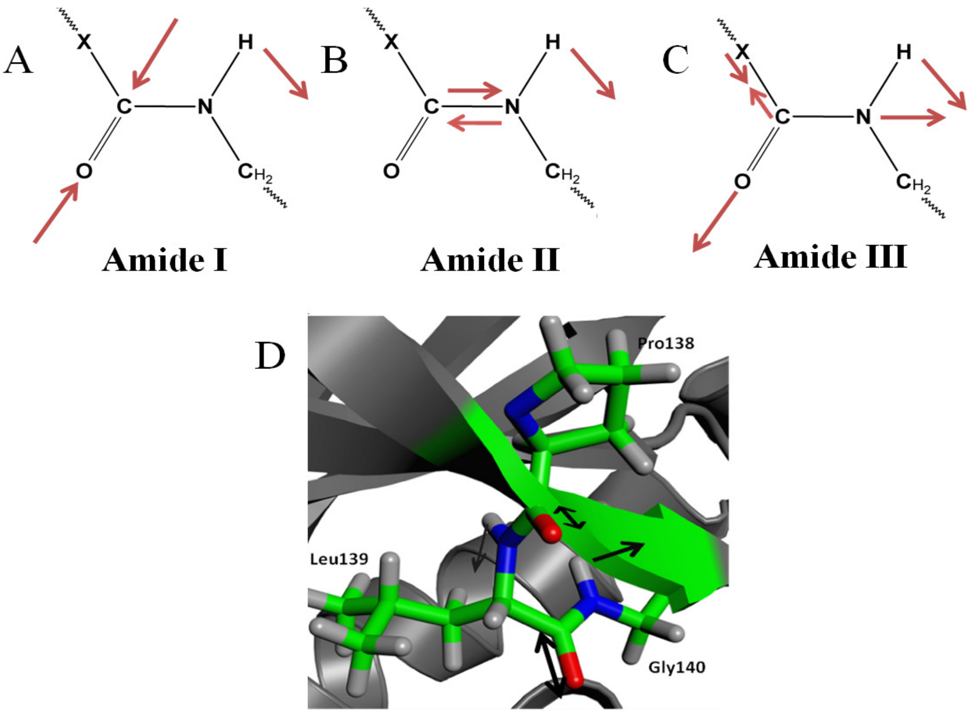

Figure 1.4: The amide I, II and III modes are shown in A, B and C respectively. D shows the amide I band in a protein molecule (taken from PDB ID: 1MQ4)

chains also. Thus, it is less suitable for secondary structure analysis. Since the secondary structures (see Figure 1.5) have their own characteristic amide I band positions, the amide I band can be deconvoluted to get the fraction of each of them from their relative intensities. The amide I band shape and position are effected by various types of interactions. There are some effects like the splitting of bands in case of β-sheet structures with the main band lying at around 1630 cm^{-1} and a weak band lying around 1690 cm^{-1}. These effects can be explained theoretically by mechanism of transitional dipole coupling. This splitting of amide I frequency occurs in case of antiparallel β-sheet and is observed in both IR and Raman [19]. Other effects like through-bond coupling and hydrogen bonding also modifies the amide I band frequency to varying extents. The dielectic constant of the protein environment also has an effect on the amide I frequency.

Other types of secondary structures include the α_{II}-helix and turns. Due to weaker hydrogen bonds, the amide I frequency lies around 10 cm^{-1} higher than that of α-helix. The turn structures absorbs between 1700 and 1630 cm^{-1} and its exact frequency depends upon the type of turn and the dihedral angles [19]. In proteins the secondary structures other than α-helix and β-sheet have modes present in the entire spectrum thus making it difficult to distinguish between different structures, for example, of a turn [20].

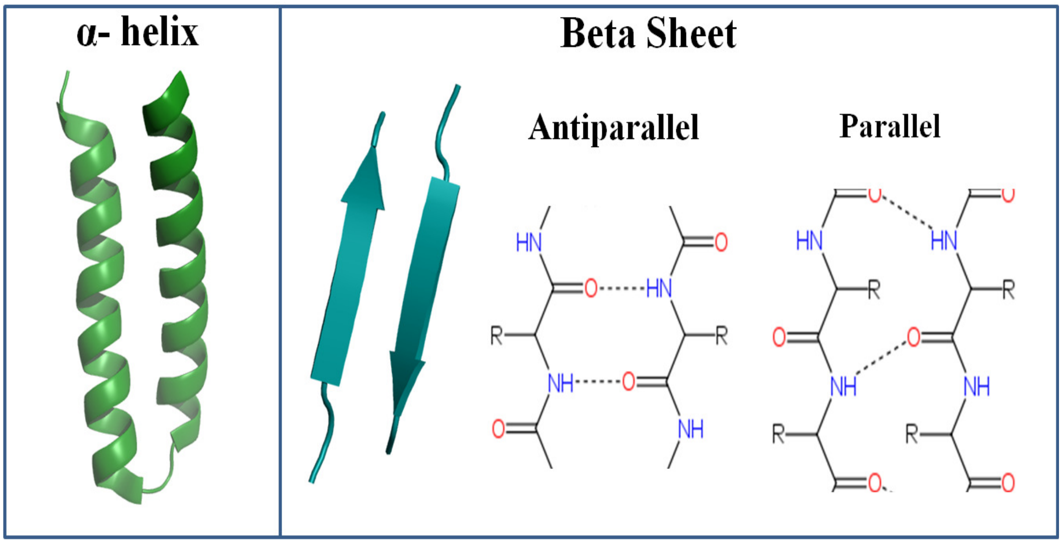

Figure 1.5: The important secondary structural components of proteins

1.5 SERS of proteins

Some of the drawbacks of normal Raman like low scattering cross section, fluorescence background and need for a large amount of sample can be addressed by SERS. This technique is being considered as a potential tool for the study of bio-molecules. Raman gives the average of all the vibrational information present within the probe volume of the laser. But in case of SERS, the spectrum can look very different from normal Raman because of a few factors. Firstly a new set of selection rules come into play . Since the electric field decays down from the nanoparticle surface, the part of molecule in the vicinity of the surface of the nanoparticles experiences greater enhancement. Therefore, in case of bigger molecules like protein, SERS provides surface information about the molecule. As mentioned earlier, the Raman scattering intensity is proportional to $(\frac{\partial\alpha}{\partial q})_0 E_0$. The polarizability tensor is represented by Eq.1.14. The change in polarizability is given by the Raman tensor,

$$\hat{R} = (\frac{\partial\alpha}{\partial q})_0 = \begin{bmatrix} \alpha'_{xx} & \alpha'_{xy} & \alpha'_{xz} \\ \alpha'_{yx} & \alpha'_{yy} & \alpha'_{yz} \\ \alpha'_{zx} & \alpha'_{zy} & \alpha'_{zz} \end{bmatrix} \tag{1.14}$$

A Raman mode has a xy component when the α'_{xy} element in the Raman tensor is non-zero. The appearance of a mode in Raman spectrum is dependent on the orientation of the molecule with respect to the polarization of the incident light and the observed Raman intensity depends on the polarization of the incident and scattered light (denoted by $\hat{\epsilon_s}$ and $\hat{\epsilon_o}$ respectively). This is significant in case of SERS. The maximum enhancement of a SERS mode happens when both the incident and scattered light is polarized in the same direction ($\hat{\epsilon_s} = \hat{\epsilon_o}$). The A_1 symmetry has polarization components xx, yy and zz. Symmetry species A_2, B_1 and B_2 only has xy, xz or yz polarizability components. Therefore, we see that each symmetry species has a particular group of polarization components. Modes with xx, yy and zz polarizability components are independent of the polarization of the incident light. In case of SERS, in order to achieve the E^4 enhancement, both the incident and scattered light should bring about SERS enhancement. These two lights must be polarized in the same direction as the electric field in the vicinity of the nanoparticle for the maximum enhancement. Therefore, for determining the SERS intensities, knowledge of the Raman tensors of different modes and also the local field polarization experienced by the molecule are required. Raman tensors can be found out by using density functional theory (DFT) or by symmetry analysis.

All these factors have lead to the introduction of the concept of surface selection rules in case of SERS by Moskovitz [21] on the basis of local field polarization.In case of most experimental studies, it is qualitatively assumed that the local field polarization is perpendicular to the surface of the metal. Therefore, the modes with strong Raman tensor component normal to the surface are enhanced the most. Those modes lying parallel to the surface are not enhanced. Therefore, based on this analysis, the molecular orientation can be inferred whether the molecular unit is upright or flat on the surface of the metal.

Because of these surface selection rules, the SERS spectrum of a protein looks quite different to the normal raman spectrum of the same protein. In SERS, some peaks can be observed which cannot be seen in diffraction limited Raman. Like Raman, in SERS too, the spectrum is dominated by the ring modes of the aromatic amino acids as well as from the amide modes. Interestingly, the amide II mode which is not Raman active, can be seen in SERS. The amide I band is narrow in case of SERS when compared to Raman. This implies that SERS gives specific information about the secondary structure at the point of attachment of the protein to the nanoparticle surface. Thus, deconvolution of amide I peaks for secondary structure assignments are not necessary in SERS. The SERS spectrum also consists of information related to the aliphatic side chains including the disulfide bonds and carboxylate groups similar to that of normal Raman.

In this work, we will discuss the SERS and Raman spectra of proteins of the therapeutic and the biomedical relevance. The utility of Raman and SERS to elucidate specific information regarding the interaction of the small molecules with proteins will be highlighted.

CHAPTER 2

EXPERIMENTAL TECHNIQUES

2.1 Setup for surface enhanced Raman spectroscopy

A custom made Raman setup was used for the SERS experiments (Figure 2.1). An epi-fluorescent microscope was converted to a Raman microscope whose details are given elsewhere [22]. The Raman setup consisted of a laser source, fluorescence microscope based collection optics, a Raman spectrograph and computer interfacing. Each of these parts of the Raman setup is discussed below.

Laser: Raman excitation source were either a gas laser (He-Ne laser, 632 nm) or a solid state laser (frequency-doubled Nd-YAG laser, 532 nm). The choice of laser depends on the absorption region of the nanoparticles used for SERS. The incident light from laser comes in resonance with the surface plasmons of the nanoparticles resulting in greater SERS enhancement.

Collection optics: The laser passes through a band-pass filter before entering the input port of an upright microscope. The laser beam is diverted towards the sample by a dichroic mirror and the incident light is focused on to the sample using a high numerical aperture objective lens. The scattered light is then collected back by the objective and after it passes through an edge filter is directed towards the output port of the microscope. The filtered light is then directed towards the Raman spectrograph through an optical fiber which is f-number matched to the spectrograph.

Raman spectrograph: The Raman spectrograph consists of a computer controlled adjustable slit and a turret. The turret has three gratings which can be used to attain different resolutions. These three kinds of gratings are 600, 1200 and 1800 grooves/mm respectively. The higher number of grooves/mm gives more spectral resolution but lesser throughput. The captured light is converted into electronic signals through a charge coupled device (CCD) and is interfaced to a

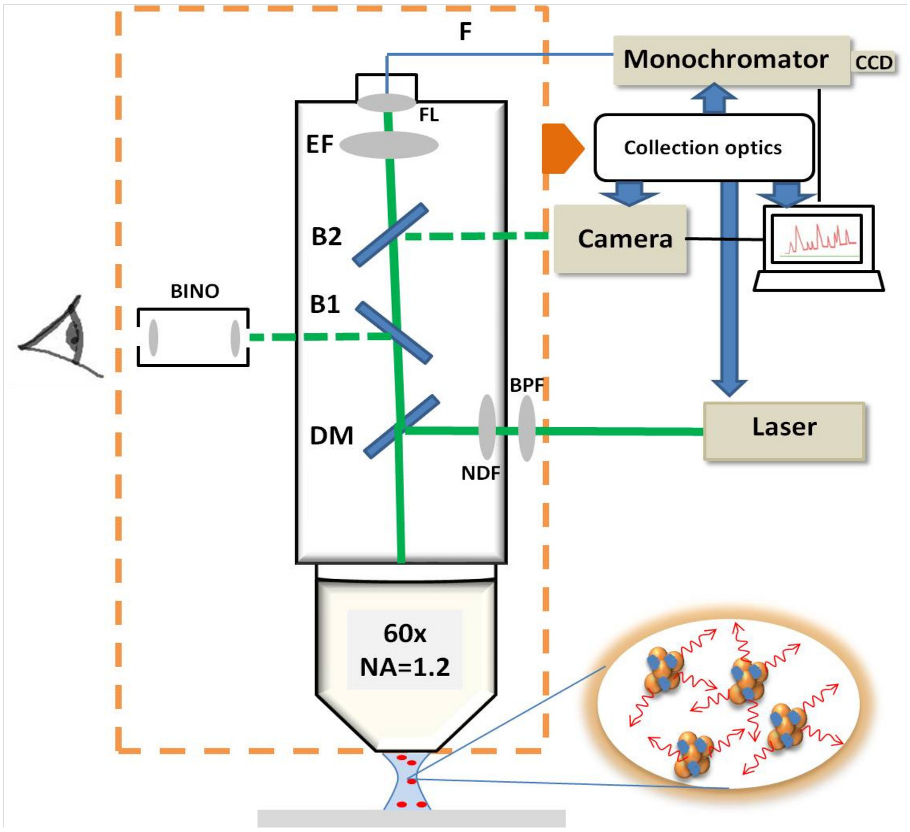

Figure 2.1: SERS microscopy setup: The scattered light from a sample in aqueous solution is collected by a water immersion objective and directed to the monochromator via the collection optics. The collection optics is connected to a monochromator and CCD, camera and a laser input. The camera and the monochromator are connected to a computer. The collection optics consists of the following components. NDF neutral density filter, BPF band pass filter, DM dichroic mirror, B1 and B2 beam splitters, BINO binocular, EF edge filter, FL focusing lens and F optical fibre. Figure adapted from [17].

computer. A digital camera port is also present atop the microscope to allow simultaneous optical image capturing along with spectral acquisition.

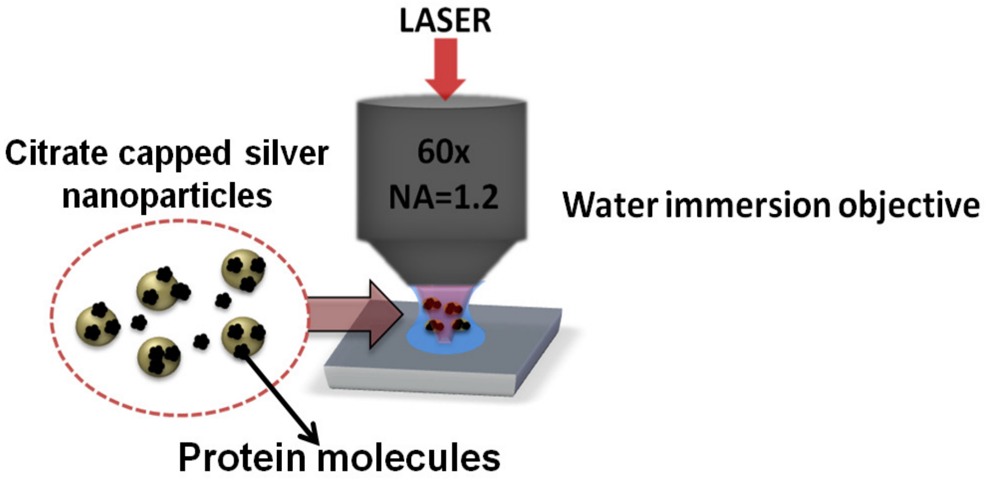

Figure 2.2: Water immersion 60x objective used for acquiring SERS of protein samples in an aqueous environment.

2.2 Spectral measurements

Preparation of samples and objectives: SERS of the samples would be performed either in liquid medium or in a dry state. In case of liquid samples, typically 10-20 μL would be dropped on a clean glass slide (grooved or normal). A water immersion objective would focus the laser on to this liquid sample (Figure 2.2). The higher the numerical aperture (N.A.) of the lens, higher is the spatial resolution which is ideal for acquiring spectrum where the object lies in contact with the objective. Since the SERS samples contain nanoparticles and sticky moieties like proteins, it is necessary to clean the surface of the objective lens thoroughly. A drop of Proteinase K solution was put on the objective lens and incubated at 37°C for around 30 mins and thoroughly washed with water and ethanol. The proteinase K solution helps to digest proteins which tightly binds to the glass surface and thus makes the objective lens clean.

Measurement region and choice of grating: The entrance slit to the monochromator was typically set at 200 μm. The width of the slit defines the resolution of the spectrum. In case of weakly scattering samples, the slit width can be increased for an increase in the intensity, but the resolution is compromised. For the SERS experiments, the 1800 grooves per mm grating was used to achieve a high resolution of 0.7 cm^{-1}. At this resolution, the CCD chip covers around 600 cm^{-1} in a single window. Therefore to scan a region from 100 to 4000 cm^{-1}, the entire spectrum is divided into 7 windows. The overlap between the windows was around 30 cm^{-1}.

Intensity of laser: The intensity of the 632 nm laser was kept at 4 μW at the sample to avoid damage to the sample. When sample degradation sets in, the spectrum is dominated by the D and G peaks coming from amorphous carbon formed due to the charring of the substrate. These peaks are found at around 1350 and 1600 cm^{-1} respectively. The laser intensity was adjusted in such ways as to prevent the sample from degrading as well as to get the highest signal-to-noise ratio.

Accumulation time: The average accumulation time for acquiring SERS spectrum varied from 30s to 120s. It must be noted that the more is the accumulation time, the more is the exposure of the sample to laser. This might cause the sample to undergo degradation. To get a better spectrum, multiple spectra are averaged by increasing the accumulation number.

Calibration of the spectrum: The accuracy of Raman spectrum is crucial for accurate interpretation of data. There are several factors which contribute to errors in the wavenumber. For example, the movement of the grating of the monochromator can cause minor shifts. Therefore, to avoid such errors, calibration of the spectrum is necessary. The standard way for calibration is to collect a spectrum of a compound which has sharp Raman peaks and compare them with their standard positions reported in the literature. Instead of a compound, sometimes a neon glow lamp is used as an emission source as it has many characteristic sharp lines in the complete region of interest. The spectrum of the unknown compound is then fitted accordingly to get the calibrated spectrum.

Analysis of Raman spectra: Majority of bands of Raman and SERS spectra of proteins are found in the region between 500 to 1750 cm^{-1}. These modes have been assigned by various means in the last 50 years. The vast literature available on assigned modes of known compounds with known structures is utilized for band assignment of proteins. But due to huge overlap of different modes owing to the complex structure of protein, it is sometimes difficult to assign some modes. Therefore, specific experiments have to be carried out to confirm the assignments. One such important mode is the amide I mode, which will be discussed in the subsequent section. After calibration of the spectrum, the buffer spectrum should be obtained to check its contribution to the main spectrum. It must be noted that certain buffer components give very large Raman scattering which can completely dominate the protein spectrum. Therefore these components should be removed from the protein solution through dialysis before acquiring the protein spectrum. The optimum composition of the buffer is discussed in the subsequent chapters.

2.3 Steps to acquire SERS spectum of a protein

The four major steps to acquire SERS spectrum of a protein are given below.

2.3.1 Attachment of proteins to nanoparticles

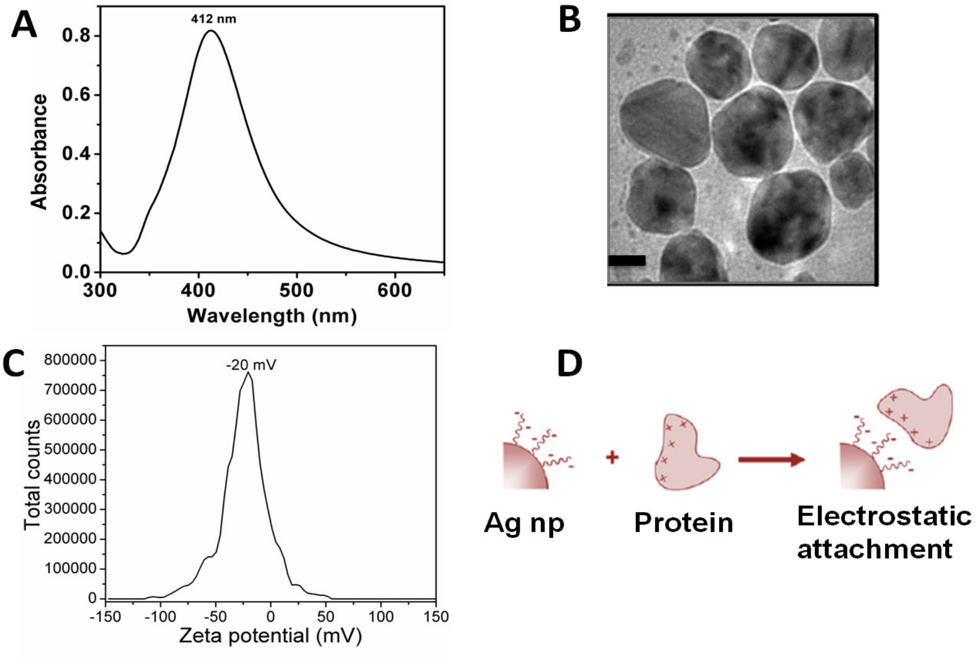

Figure 2.3: Attachment of protein to nanoparticles: (A) The Uv-Vis spectrum of Ag nanoparticles showing maxima at 412 nm. (B) TEM of Ag nanoparticles (scale bar=20nm). (C) Zeta potential measurement of Ag nanoparticles showing overall negative charge. (D) Scheme showing electrostatic attachment of proteins to nanoparticles.

Plasmonic silver nanoparticles were synthesized by Lee-Meisel method [23]. Milli-Q water with a resistance of 18.2 MΩcm at 25°C was used for all the exeriments. 18 mg of silver nitrate was added to 100 mL of water and boiled under reflux conditions to maintain water at a constant level. 2 mL of 1% sodium citrate solution was added to this solution under vigorous stirring. The boiling and stirring was continued for 1 h. The solution was then brought back to room temperature while stirring. The nanoparticles were then characterized by Uv-vis spectroscopy, zeta-potential measurements and transmission electron microscopy (TEM) (see Figure 2.3).

There are several strategies used to link protein molecules to the surface of nanoparticles. The most common are electrostatic absorption, attachment to ligand on nanoparticle surface, using the cofactor-ligand chemistry and direct conjugation to the nanoparticle surface [24]. We have seen in the previous chapter that direct attachment of molecules is required for obtaining chemical enhancement. Since protein molecules are weak Raman scatterers, it is useful to bring them in contact with metal nanoparticle surface.

Citrate is known to be a weak capping agent. The analyte molecules are attracted electrostatically and come in direct contact with the metal nanoparticle after replacing the citrate molecules. Our strategy is to use similar electrostatic interactions to conjugate the proteins on to the surface of the nanoparticles. DLS data shows a net charge of - 22 meV on the surface of the nanoparticles. The pH of as-prepared nanoparticles was found to be $\sim$ 8. Therefore any protein of pI above 8 can be electrostatically attached to the surface of these citrate capped nanoparticles.

The size of nanoparticle is also a determining factor for attachment of proteins. But, it is valid only for sizes comparable to that of proteins. As evident from the crystal structure of Aurora A, the diameter of the protein is around 5 nm. Since the silver nanoparticles are more than 30 nm in diameter, the proteins can be thought to be attached in a similar way as to a solid flat surface. Therefore the size distribution of 30 - 50 nm of nanoparticles will not affect the mode of attachment of the proteins. Also this size distribution is necessary for generating surface plasmons in the visible range for application in SERS. In the subsequent sections we will demonstrate that SERS provide more direct experimental data for understanding the protein- nanoparticle interaction.

2.3.2 Activity of the protein-nanoparticle conjugate

When an interface is created between organic and inorganic materials, it leads to many problems. In nanometer scales, the surface effect is enhanced and it might lead to the structural alterations in macromolecules like proteins. The structures of proteins are directly related to their functions. Therefore, in order to get reliable SERS spectra, both the structure and function of the proteins must be maintained in the presence of nanoparticles. Biochemical activity assays are done to check the activity of the protein-nanoparticle conjugate. The schematic representation is shown in Figure 2.4.

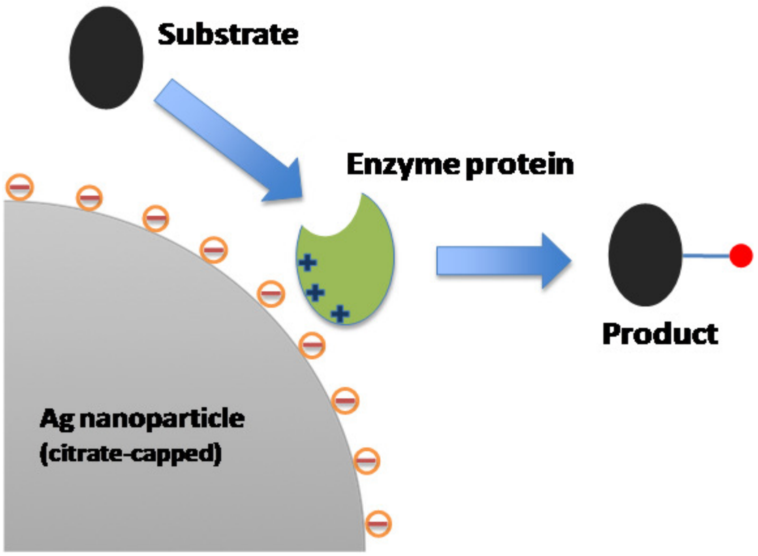

Figure 2.4: Schematic showing the biochemical assay performed to check the activity of protein in the presence of Ag nanoparticles

2.3.3 Amide mode verification by deuteration studies

Hydrogen deuterium exchange is a way to study the stability and flexibility of proteins. It is also used as a method to assign Raman bands to proteins, especially in the case of the amide bands. The deuteration of the labile NH group brings

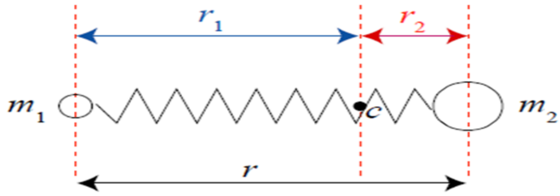

Figure 2.5: Bond vibration can be considered as two masses connected by a spring.

about a change in the position of the amide I band. The amide I vibration is independent of the nature of the side chains but is influenced by changes in the secondary structure of the backbone. Therefore, it is important to deduce the position of these bands for elucidating their secondary structure. We know that a bond vibration can be treated classically as a vibration of a spring attached to two masses which corresponds to atoms (Figure 2.5). The vibrational oscillation of this spring is given by

$$\nu_{osc} = \frac{1}{2\pi}\sqrt{\frac{k}{\mu}} \tag{2.1}$$

where μ is the reduced mass and is given by $\frac{m_1 m_2}{m_1+m_2}$. When any of the masses m_1 or m_2 changes, as it happens when hydrogen atom (H) is replaced by deuterium (D), the ν_{osc} also changes. The amide modes, which are combination of vibrations containing NH modes are prone to changes on deuteration. The amide I band contains NH in-plane bend which is responsible for its sensitivity to N-deuteration of the backbone. Thus it shifts to lower wavenumbers on deuteration. The amide II mode also consists of NH in-plane bend and on N-deuteration converts to C-N stretching vibration. The ND bending vibration has a lower frequency than the NH bending vibration and it no longer couples to the C-N stretching vibration. Therefore it occurs as a new mode in other regions around 900 cm^{-1}. In case of amide III, the ND separates out and gets redistributed among other modes. Therefore it is evident that if a mode is to be verified as an amide mode, it has to have a change in intensity or position on deuteration.

2.3.4 Amide I verification by denaturation studies

Amide I band is dependent on the secondary structure of protein and the secondary structure is disrupted in case of thermal denaturation. Therefore, when a protein is denatured, change in amide I mode is expected to be seen. In certain cases, the thermal denaturation takes place through a molten globule state. It is characterized by the initial downshift of amide I band at the melting temperature then subsequent upshift to higher wavenumbers at higher temperatures [25]. In case of SERS it is observed that increased side chain interactions with the nanoparticle surface obscures the amide I band [26]. When thermal denaturation happens, the unfolding of protein can lead to greater interaction of the side chains with the surface of the nanoparticle. This reduces the intensity of the amide I band and thus confirms it. Therefore study of denatured proteins can also be used for verification of amide I mode.

2.4 Fourier Transform Raman spectroscopy of fluorescent molecules

The fourier transform Raman spectroscopy (FT-Raman)uses near-infrared laser of wavelength 1064 nm. The major advantage of using FT Raman is to bypass the fluorescence of highly fluorescent samples. Although fluorescence is completely absent, the Raman scattering is weak as scattering is proportional to $1/\lambda^4$. An interferometer is used to convert Raman signals into an interferogram. Thus the entire spectrum is collected simultaneously. At low signal levels, the spectral noise is predominantly constituted by dark noise. Since it is independent of the intensity of the Raman signal, the direct transmission of the entire spectrum at once to the detector improves the signal-to- noise ratio. The obtained interferogram is fourier transformed to convert it back into Raman spectrum. FT-Raman is used to study the complexes of proteins with highly fluorescent molecules and its use has been demonstrated in chapter 6.

CHAPTER 3

SERS STUDIES ON AURORA A AND AURORA B KINASES

This chapter constitutes the following publication:

Surface enhanced Raman spectroscopy of Aurora kinases: direct, ultrasensitive detection of autophosphorylation

Soumik Siddhanta, Dhanasekaran Karthigeyan, Partha P. Kundu, Tapas K. Kundu and Chandrabhas Narayana

RSC Advances 3, 4221-4230 (2013).

3.1 Introduction

The family of Aurora kinases is an important member of the mitotic kinases. Aurora A-C have been discovered till date. Aurora A is involved in centrosome duplication and bipolar spindle assembly. Another kinase of this family, Aurora B is a component of the chromosome passenger complex that helps in chromosome alignment, kinetochore-microtubule biorientation and cytokinesis [27]. Aurora B is also a spindle pole assembly check point protein that can sense the tension imbalance on either side of the kinetochore. Thus, it corrects chromosomal misalignment during the metaphase stage of mitosis [27]. Aurora A and Aurora B have been found to be overexpressed in several tumors in humans. Both Aurora A and B kinases present inside the cell at physiological concentrations are inevitable component of normal cell division [28]. Hence an aberrant expression or activity of these kinases may promote various factors that favor aneuploidy and oncogenesis [29]. It is for this reason Aurora kinases are one of the hot targets for anti-cancer therapy. Crystal structure of Aurora A kinase was reported in the year 2002 by Cheetam et al [30]. Aurora A has the classical bilobar protein kinase fold comprising of a N-terminal lobe, C-terminal lobe and a hinge region connecting these two lobes. Aurora B is a Serine/Threonine kinase and the human homologue is about 344 amino acids long which include a C-terminal kinase domain (residues 77-327) and a nucleotide binding region between residues 83-91 [30]. Aurora A and B are nearly identical except for four of the residues within the catalytic domain and has an overall structural similarity of nearly 70% [31]. We have utilized this highly sensitive technique of SERS to study protein kinases Aurora A and Aurora B. The knowledge of the crystal structures of the proteins validates the structural components predicted through the comprehensive SERS band assignments reported here.

Due to large similarities in structure of two kinases, it has been difficult to produce a specific inhibitor of either Aurora A or Aurora B [31]. Hence the band assignments of Aurora A and Aurora B would be helpful to detect and characterize protein-small molecule interactions at a larger scale and find suitable candidates for inhibition. The ease of sample preparation and the low volume required for the SERS studies makes it easier to use than other secondary structure analysis techniques like NMR , circular dichroism and x-ray crystallography. X-ray crystallographic data and NMR have been able to give an accurate picture of proteins and protein-ligand complexes. But the inability to obtain perfectly diffracting single crystals is often the stumbling block. This is a prerequisite for X-ray diffraction. NMR also has its own shortcomings in not being applicable to proteins which are larger than a few hundred residues. These drawbacks, combined with the need for large quantity of samples make it necessary to look towards alternative techniques for drug-screening applications.

Raman spectroscopy provides structural and chemical information and works in different conditions including physiological environments. Thus, Raman spectroscopy and SERS can emerge to be complementary techniques to x-ray crystallography and NMR. Our goal is to demonstrate the usefulness of SERS in extracting specific information from the protein molecules at low concentrations. By using this technique we also demonstrated that it is possible to distinguish between two very similar protein structures. To demonstrate the extremely high sensitivity of this technique we showed that it could detect autophosphorylation in Aurora A, which is an important post-translation modification. Autophosphorylation of Aurora A at residue T288 enhances its kinase activity [32]. The detection level was in nanomolar regime which is lower than other conventional techniques used in detection of proteomic modifications like radio labeled ATP molecules, western blot, enzyme-linked immunosorbent assay (ELISA), flow cytometry, mass spectroscopy (MS) etc.[33]. The structural information obtained from the extensive SERS band assignments of this protein can help in understanding protein-drug interactions as well as the interaction of proteins with the surface of plasmonic nanoparticles which are widely used in sensor applications.

3.2 SERS of Aurora A and Aurora B

3.2.1 Experimental details

3.2.1.1 Purification of proteins for SERS and kinase assay

Aurora kinase A and Aurora B enzymes were expressed as C-terminal His6-tagged proteins and purified using Ni-NTA affinity purification from the recombinant baculovirus infected Sf21 cells. For performing SERS, the proteins were dialyzed against Tris-NaCl (Tris 20 mM, EDTA 0.2 mM and NaCl 100 mM) buffer extensively so as to remove glycerol, imidazole and 2-mercaptoethanol. The bacterially expressed recombinant histone (Xenopus) H3, which comes in inclusion bodies, was purified by denaturation in 8 M urea followed by renaturation as described elsewhere [34]. 1 mg of bacterially expressed recombinant histone H3 was incubated along with baculovirus-expressed His6-tagged protein (40 ng) in a 30 ml reaction mixture containing 50 mM Tris. HCl, 100 mM NaCl, 0.1 mM EGTA, 10 mM MgCl2, 0.2% 2-mercaptoethanol and [γ-^{32}P] ATP (Specific Activity 3.5 Ci mM^{-1}). The reaction mixture along with ATP was incubated at 30 °C for 10 min. The reaction mixture was precipitated using 25% TCA and resolved using 15% PAGE followed by autoradiography. For autophosphorylation the same assay was carried out with unlabelled ATP in the absence of histone substrate and subsequently dialyzed against Tris-NaCl (Tris 20 mM, EDTA 0.2 mM and NaCl 100 mM) buffer to remove unbound ATP molecules.

3.2.1.2 Sample preparation and SERS

The silver colloid preparation and the experimental setup is explained in the experimental techniques (Chapter 2). The laser power used at the sample was 5 mW. Typical concentration of protein used was 40 nM. Samples were prepared by keeping the concentrated nanoparticle solution to analyte ratio at 5 : 1. The amount of protein used per sample was 0.8 picomoles. For deuteration studies, the protein was treated with 50% D_2O solution. For SERS on salt aggregated colloids the final salt concentration in the colloid solution was kept at 5 mM prior to the addition of protein. The typical accumulation time used was 30 s. SERS spectra were smoothened using standard five-point fast Fourier transform (FFT) filtering technique.

3.3 Results and discussions

3.3.1 Attachment of proteins to silver nanoparticles

We have used citrate capped silver nanoparticles of about 30−50 nm in diameter for SERS. Citrate is known to be a weak capping agent and the protein molecules can displace them on the nanoparticle surface through electrostatic interaction [35]. Another important advantage of using citrate-capped nanoparticles in SERS experiments is that the citrate molecules does not interfere with the protein spectra as they do not show any observable modes themselves. Our strategy

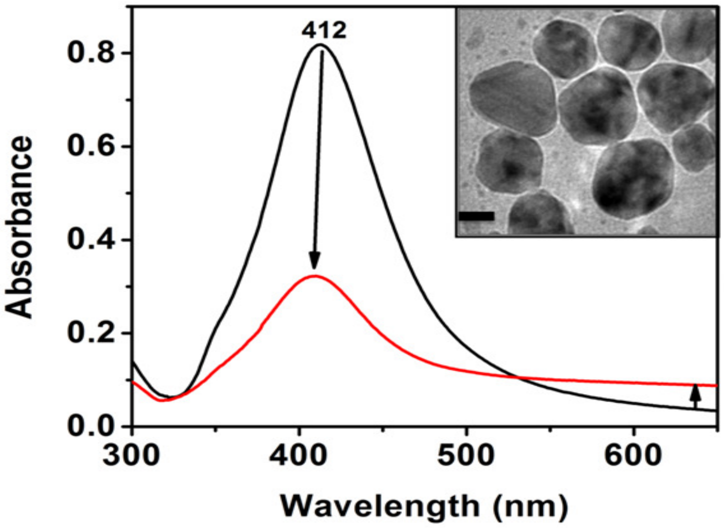

Figure 3.1: UV-vis absorption spectrum of Ag nanoparticles without (black) and with (red) salt aggregation. The TEM of the Ag nanoparticles are shown in the inset. Scale bar represents 20 nm

was to use this electrostatic interaction to conjugate the aurora kinase proteins on to the surface of the nanoparticles. The negatively charged nanoparticles electrostatically bind to the overall positively charged Aurora kinases, which have a pI of more than 9. The two major factors that determine the electrostatic attachment sites of the proteins are (a) the positively charged domains present on the protein that can interact with the negatively charged nanoparticles and (b) the size of the nanoparticle that interacts with the protein. The size of nanoparticles also determines the total surface area available to the protein for attachment. The present size distribution of the nanoparticles is necessary for generating surface plasmons in the visible range for application in SERS. The colloids were also activated or aggregated partially to facilitate the binding of the proteins to the nanoparticles and to get better SERS enhancements. The aggregation of the Ag colloids at 5 mM NaCl concentration is demonstrated by UV-Vis spectroscopy as shown in Figure 3.1. The intensity of the absorbance maxima at 412 nm decreases considerably and there is an increase in intensity at higher wavelengths which is due to aggregation.

3.3.2 Activity of protein-nanoparticle conjugates

In order to find out the enzyme activity, in-vitro kinase assays were performed using free enzyme as well as the enzyme adsorbed on the nanoparticle (Figure 3.2). The activities of the purified Aurora A (Figure 3.2 C (i)) and Aurora B (Figure 3.2 C (ii)) were confirmed by performing dose dependent phosphorylation on recombinant histone H3 substrate using [γ-^{32}P]- ATP. Similar kinase assays were performed in the presence of Ag nanoparticles at a particular concentration of [γ-^{32}P]-ATP (Figure 3.2 D). The results show that the overall kinase activities of Aurora A and Aurora B are only moderately reduced after adsorption on the silver nanoparticles. The kinase binds quite strongly to the nanoparticle at a pH of 7.5, which presumably causes a drop in their activities as compared to the free enzymes. As revealed from the kinase assays performed in the presence of Ag nanoparticles, the enzyme is sufficiently active even after adsorption onto the nanoparticle surface, and hence should be suitable for structural analysis by SERS. The retention of enzymatic activity upon adsorbtion to nanoparticles implies that the active sites of the proteins are still accessible to the substrate molecules without any hindrance.

3.3.3 SERS of Aurora Kinases

The X-ray crystallographic data [30] shows that Aurora A has an N-terminal domain (residues 127−215) which consists of β-strands and a C-terminal α-helical domain (residues 216−385). The hinge region which connects these two domains (residues 210−216) forms the catalytically active site. Similarly Aurora B has an

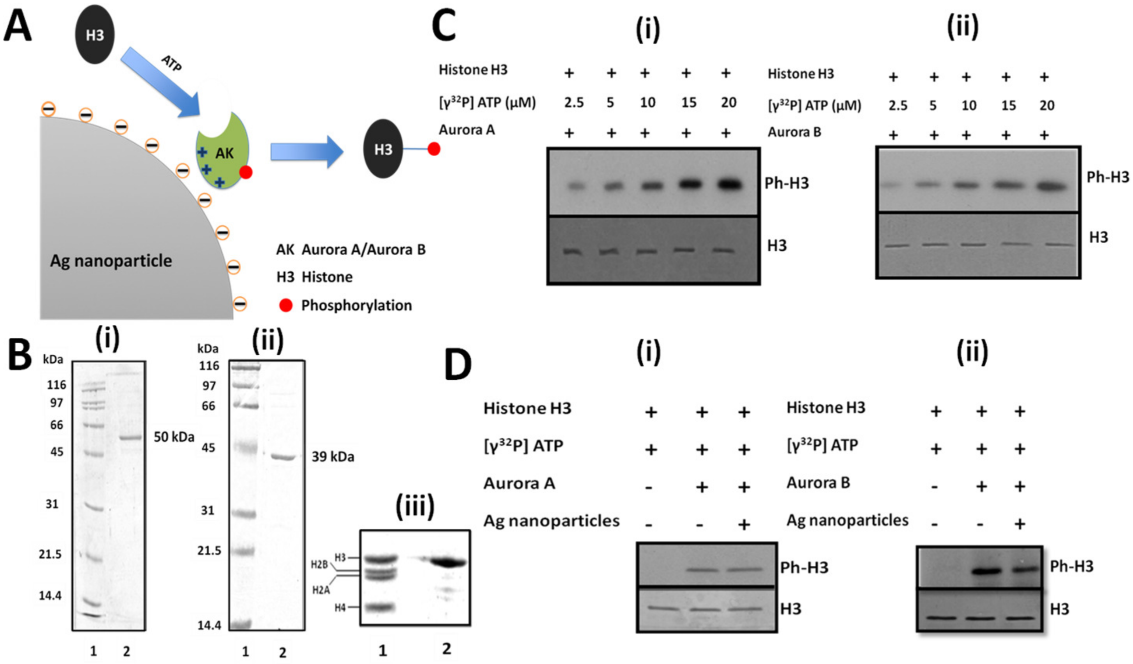

Figure 3.2: (A) Schematic showing the kinase activity of Aurora kinase over a negatively charged Ag nanoparticle surface. (B) Full-length recombinant His6-tagged (i) Aurora A and (ii) Aurora B proteins used in the experiment (iii) purified Histone H3 (used for all experiments). (C) Kinase assay of (i) Aurora A and (ii) Aurora B using recombinant histone H3 as substrate. (D) Effect of nanoparticle on kinase activity of (i) Aurora A and (ii) Aurora B.

N-terminal β-sheet domain and a C-terminal α-helical domain [36]. SERS was used to obtain surface sensitive information about these proteins. It is known that SERS can be used to look into the protein conformations as well as to examine the spatial structure [37]. The spatial distribution of individual amino acids and their proximity to the nanoparticle surface determines the region of the molecule which gets enhanced in a SERS experiment [16]. Another factor which influences SERS spectra is its orientation relative to the surface. Due to the surface selection rules, which are quite different from the usual Raman selection rules, the vibrational modes having vibrations perpendicular to the metallic surface of the nanoparticles

Table 3.1: SERS band assignments for Aurora A and Aurora B on non-aggregated and aggregated Ag colloids. The new bands arising in case of aggregated nanoparticles are marked by $*$

Aurora A(cm^{-1})	Aurora B(cm^{-1})	Band assignment
	533*, 571*	Trp
	634*, 636*	C-C twisting of Tyr
652		ν(C-S)P_H, Cys
665	679*	Tyr
	726, 733*	$\delta(COO^-)$
762	760	Trp (W_{19}) or His
803, 808*	800*, 804	Tyr and/or ν_{as}(C-S-C)
849, 837*	857	Tyr
910	912	$\nu(COO^-)$/C-C stretch of Pro ring
931	932	$\nu(COO^-)/\alpha$ helical C-C stretching vibration
998*	1000*,1002*	Phe ν_{12}
1028*, 1033	1025	Phe ν_{18a}/ C-N stretch
1065		C-N stretch
1100	1105*, 1100	$\tau(NH_2)/\nu(C\text{-}C)/\nu(C_\alpha\text{-}N)$, Trp
1126	1124	$\nu_{as}(C_\alpha CN)$
1164	1164	ν_{as}(CCN), Tyr and/or Phe
1189	1189	Phe ν_{9a}
1259	1259	amide III/ C-C_α-H deformation
1324	1321, 1324*	δ(CH) and/or Trp
1349	1347	C_α-H bend/C-C_α stretch
1443	1444*, 1446	$\delta(CH_2)/\delta(CH)$
1471	1471	$\delta(CH_2)/\delta(CH)$, N-H deformation, Trp, His
1497		Phe, Tyr
1524	1524	amide II
1534	1532	Trpω_3
1586	1577*, 1583	$\nu_{as}(COO^-)$, His, Trp and/or Phe
1620	1616	amide I

are enhanced to a greater extent compared to the modes with vibrations parallel to the surface [21]. Therefore SERS can give information about the orientation of a molecular moiety on the metallic nanoparticle surface. The electromagnetic enhancement factor decays as a factor of $\frac{1}{r^{12}}$, where r is the distance between the molecule and the nanoparticle surface [38]. Thus the amino acid residues which are present on the surface of the protein will be observed in the SERS spectra.

The spectra of both the proteins Aurora A and Aurora B are shown in Figure 3.3. The band assignment has been done in accordance with the available literature on the SERS spectra of amino acids and proteins (Table 3.1) [39; 40] .We have also recorded the Raman spectra of the silver nanoparticle solution and the protein buffer (Tris 20 mM, EDTA 0.2 mM and NaCl 100 mM) (Figure 3.12) to ascertain that they do not contribute to the SERS of the proteins.

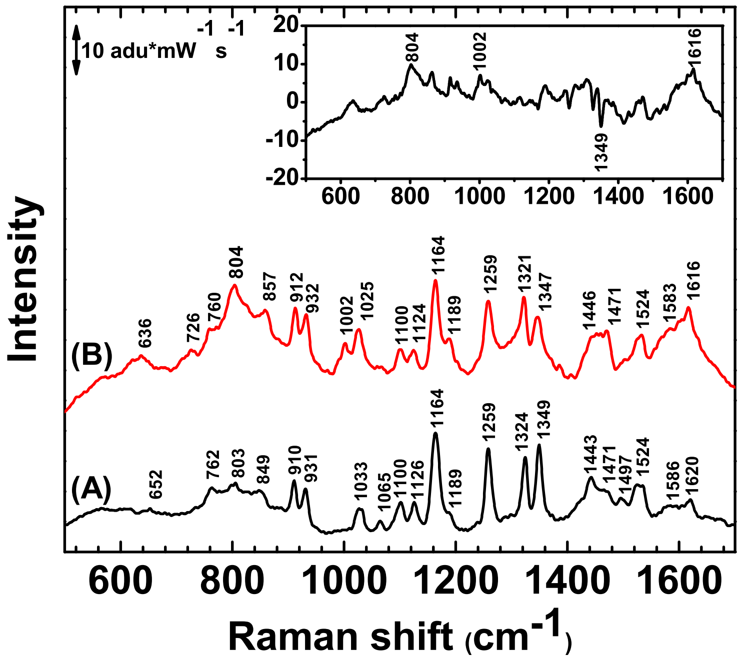

Figure 3.3: SERS spectrum of (A) Aurora A and (B) Aurora B on Ag colloid. The inset shows the difference spectrum (B-A).

3.3.3.1 Aromatic amino acids

The SERS spectra of both Aurora A and Aurora B are dominated by peaks from aromatic amino acids. In Aurora A the modes at 1033, 1189 and 1586 cm^{-1} can be assigned to in-plane CH bending (ν_{18a}), combination of in-plane CH bending

(ν_{9a}) with ring stretching and phenyl C-stretching (ν_{8a}) respectively, of the phenylalanine amino acid [41]. The band at 1002 cm^{-1} corresponding to symmetric ring breathing mode of the benzene ring in aromatic amino acids is absent in Aurora A, but is present in Aurora B. The corresponding modes in Aurora B for phenylalanine occur at 1002, 1025, 1189 and 1583 cm^{-1} respectively. When the benzene ring of these amino acids are oriented at a tilted angle close to 90° to the nanoparticle surface the SERS spectrum will show intense ring-breathing vibration along with the appearance of CH stretching vibration, otherwise these would be very weak. Based on this, we can say that in both Aurora A and Aurora B, the orientation of phenylalanine with respect to the metal surface is different. In addition the region from 1300-1500 cm^{-1} can be assigned for $\delta(CH_2)$ mode for phenylalanine. The Raman spectrum of tyrosine shows a characteristic doublet at around 828 and 845 cm^{-1}. This doublet is a result of the Fermi resonance between the ring breathing mode and the overtone of an out-of-plane ring bending vibration of the para-substituted benzenes. The doublet is slightly shifted to 829 and 847 cm^{-1} in the case of SERS. In addition, in the SERS spectra of the whole protein, the doublet is not always very pronounced. Such is the case for Aurora A and Aurora B, where we do not observe a clear doublet. Peaks were observed at around 849 and 857 cm^{-1} for Aurora A and Aurora B, respectively. The low frequency mode at around 829 cm^{-1} which is absent in case of both the proteins is a B_{1g} mode of tyrosine which would be greatly enhanced if the orientation of the ring was such that the face of the ring was tilted to the metal surface. These modes are sensitive to the environment of the phenyl ring and also conformation of the amino acid backbone.

3.3.3.2 Aliphatic side chain vibrations

The two amino acids with acidic side chains are glutamic acid and aspartic acid. The stretching vibration of C-COO^- appears as doublet in both Aurora A and Aurora B at 910/931 cm^{-1} and 912/932 cm^{-1} respectively. Asymmetric stretching vibration $\nu_{as}(COO^-)$ at 1586 cm^{-1} overlaps with histidine, tryptophan and phenylalanine bands. The distinct doublets arising at 1443/ 1471 cm^{-1} in Aurora A and 1446/1471 cm^{-1} in Aurora B are the CH_2 deformation vibrations. The 1471 cm^{-1} mode also overlaps with modes from tryptophan and histidine. The 1324 cm^{-1} and 1321 cm^{-1} band in Aurora A and Aurora B respectively can be assigned to CH_2 wagging vibration. In contrast, the C-N stretching modes are observed at around 1030 cm^{-1} which may be overlapped with the phenylalanine ring mode in the case of Aurora B. C-NH_2 group vibrations occur in the region 1050-1200 cm^{-1}. The $\nu(C_\alpha\text{-N})$ band appears at 1065 cm^{-1} and 1100 cm^{-1} for Aurora A and Aurora B. Whereas the $\nu_{as}(C_\alpha CN)$ band appears at 1126 and 1124 cm^{-1} for Aurora A and Aurora B respectively. The modes at 1349 and 1347 cm^{-1} for Aurora A and Aurora B are assigned to a complex mode of C_α-H bending and C-C_α stretching internal coordinates. Though this band diminishes in intensity upon deuteration, it is not an amide III mode, which is not expected to appear at this high wavenumber.

3.3.3.3 Amide vibrations

The amide band comes from the bond vibrations in the peptide units. The amide I band is a combination mode consisting of CO stretching vibrations with some contribution from N-H bending, out of phase CN stretching vibration and CCN deformation. Amide II mode is a combination of NH in-plane bend and the

CN stretching vibrations with contributions from CO in-plane bend and the CC and NC stretching vibrations. The amide III mode is the combination of the NH bending and CN stretching vibration with contributions from CO in-plane bending and the CC stretching vibration. The deuteration of NH group brings about a change in the position of the amide bands. The amide II band is a Raman inactive mode in a normal Raman experiment, but in case of the SERS, it becomes active due to the modification of the surface selection rule. The amide I band region of SERS spectra of proteins is generally narrower than the normal Raman spectra of the protein which ranges from 1600-1750 cm^{-1}. This can be attributed to the fact that the nanoparticles attach preferentially to certain secondary structures and therefore the amide I mode corresponding to these conformations is enhanced. But if one deconvolutes the amide region one can see the presence of all the amide bands. The 1620 cm^{-1} and the 1616 cm^{-1} band in Aurora A and Aurora B can be assigned to the amide I band. This has been confirmed by deuteration as the amide I of Aurora A is shifted to 1605 cm^{-1} and in Aurora B, it shifts to 1604 cm^{-1}. Deuteration decreases the vibrational frequency due to increase in mass. The origin of this band could be assigned to anti-parallel β-sheet whose band position is near 1620 cm^{-1} in Raman and IR spectra. As evident from the Aurora A crystal structure, the N-terminal lobe contain a five stranded antiparallel β sheet. The similarity in the position of the amide I band in both the Aurora kinases indicate the similarity in the structure of the homologous proteins as well as the similarity of their binding sites to the nanoparticles. Amide III band is generally observed in the region between 1200 and 1400 cm^{-1} interfered by other bands in this region. Since the band at 1259 cm^{-1} for both Aurora A and Aurora B changes in intensity upon deuteration of the proteins we believe it is due to amide III band. In general Amide II bands occur at around 1510$-$1530 cm^{-1}. Hence the peak at 1524 cm^{-1} in the spectra of Aurora A and Aurora B has been assigned to amide II mode. Since it disappears upon deuteration we are confident of this assignment.

3.3.4 Effect of deuteration on SERS of Aurora Kinases

The effect of deuteration and its utility in confirming the amide I modes is discussed in chapter 2. In case of Aurora A (see Figure 3.4), the amide I band was shifted to 1605 cm^{-1}, nearly 15 cm^{-1} shift. In the case of Aurora B the amide I band shifted from 1616 cm^{-1} to 1604 cm^{-1} on deuteration. This confirms our amide I vibrations assignments. Interestingly, upon deuteration, there is a change observed in the way Aurora B binds to the nanoparticle, suggesting that this could be an important clue to study of the subtle difference in the structures of Aurora A and Aurora B.

The amide II has large contributions from N-H bend. Therefore N-deuteration

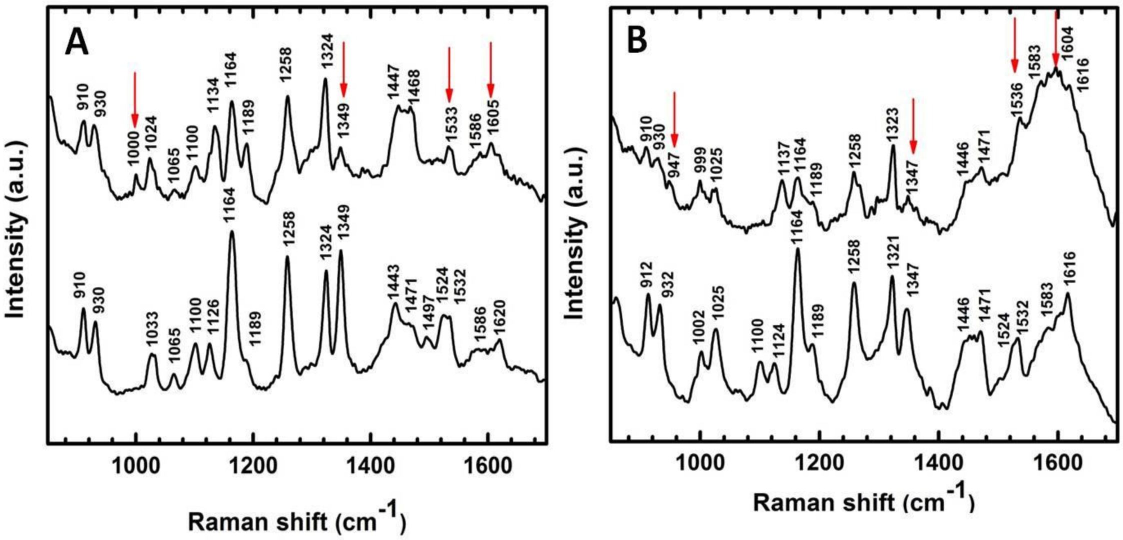

Figure 3.4: SERS spectra of (A) Aurora A kinase (below) and deuterated Aurora A kinase (top) and (B) Aurora B kinase (below) and deuterated Aurora B kinase (top). The red arrows show changes in amide bands of the proteins and also appearance of new bands.

results in the conversion of the mode to a CN stretching mode at around 1460 cm^{-1}. Based on the deuteration studies, we have assigned the band at 1524 cm^{-1} in both Aurora A and Aurora B to be amide II band. This band lies very near to the 1532 cm^{-1} band arising from Trp W3 and could have some influence from the Trp residue. On deuteration the amide II band indeed disappear. The expected new band at 1460 cm^{-1} is not directly observed as there is an overlap with $\delta(CH_2)/\delta(CH)$ modes in that region. Similar to amide II, upon deuteration, the amide III peaks also shift to lower wave number but to a larger extent around 960-1000 cm^{-1}. We see a reduction in the intensity of the band at 1258 cm^{-1} in both Aurora A and Aurora B and emergence of new band at 1000 cm^{-1} for Aurora A and 947 cm^{-1} for Aurora B respectively. On deuteration we also observe a change in the intensities of the stretching vibrations of $C\text{-}COO^-$ bands in both Aurora A and Aurora B. New bands at 1134 cm^{-1} and 1137 cm^{-1} arise for Aurora A and Aurora B respectively which may be assigned to $\nu_{as}(C_\alpha CN)$. Prior to deuteration the attachment was mainly through the carboxylate groups, but on deuteration the attachment is mainly through the N containing groups as interpreted from our results. This kind of behavior has also been observed in case of homopeptides, where the mode of attachment to the nanoparticle surface changes over time [41]. This confirms our earlier suggestion that deuteration changes the conformation of the protein.

One way to look at this is that the hydrogen-deuterium exchange requires temporal breakage of hydrogen bonds which may result in partial structure opening, thus exposing other groups to the nanoparticles surface. Since the surface groups and side chains are mostly enhanced in SERS experiments and these groups in the present case are more exposed to the solvent than to the interior of the protein, a greater change in spectra of deuterated proteins is seen. The modes corresponding to the ring vibrations of Phe and Tyr also undergo intensity changes, which again suggests the orientation of the rings to the surface of the nanoparticles has changed. The Phe and Tyr residues have modes A_1 and A_g that have polarizability components in the x,y and z directions. The enhancement of these modes does not depend on the orientation of the ring to the nanoparticle surface. These modes can be seen at 1024 cm^{-1} and 1189 cm^{-1} for Aurora A and at 1002, 1025 and 1189 cm^{-1} for Aurora B. These modes do not show any change in intensity on deuteration. The group of modes corresponding to B_1 and B_{2g} will be enhanced if the face of the ring is tilted towards the nanoparticle surface since their polarizabilities are in the x and z direction of the ring. The A_2 and the B_{1g} modes will be enhanced if the edge of the ring is tilted towards the nanoparticles surface as their polarizabilities are in the y, z direction. These bands are seen at 1164 and 1586 cm^{-1} in case of Aurora A and 1164 and 1583 cm^{-1} in case of Aurora B. On deuteration, due to the change in orientation of the rings to the nanoparticle surface, we do see a change in these modes.

3.3.5 Effect of denaturation on SERS of Aurora Kinases

The effect of denaturation of proteins and its effect on SERS spectrum is described in chapter 2. SERS was performed on the heat denatured proteins to confirm the position of the amide bands (Figure 3.5). When the protein undergoes denaturation, it assumes a random backbone structure which exhibits a broad amide I band. In case of Aurora, on denaturation the peak at 1620 cm^{-1} which is assigned to amide I band disappears and the whole amide I region appears as a broad band. Similar observations were made in case of Aurora B, where the amide I band at 1616 cm^{-1} was diminished too. The amide II band at 1524 cm^{-1} for

Aurora A and Aurora B reduced in intensity too. The intensity of all the other bands increased as the protein opened up to expose the buried groups to come in contact with the nanoparticles surface.

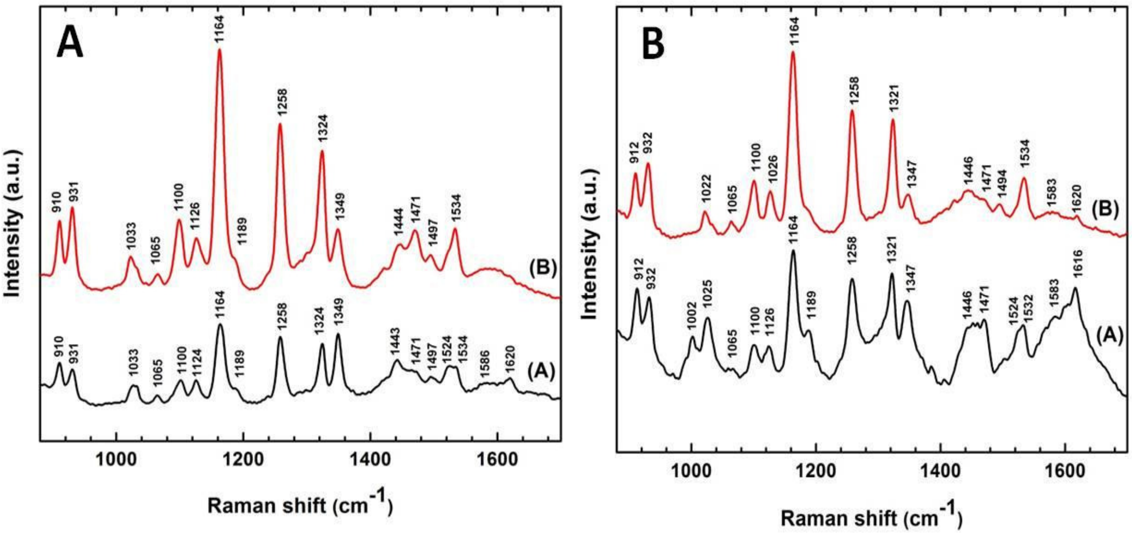

Figure 3.5: SERS spectra of (A) Aurora A kinase (below) and denatured Aurora A kinase (top) and (B) Aurora B kinase (below) and denatured Aurora B kinase (top).

3.3.6 Differentiating between Aurora A and Aurora B through SERS

Aurora A and Aurora B have similar structures (Figure 3.6) with a sequence identity of 68%. Most parts of the α-helical C-terminal domain and the N-terminal domain containing predominantly β-sheets are structurally conserved as seen from the coloration according to order parameter Q [42] shown in Figure 3.6 B prepared through VMD. Q values refer to the fraction of similar native contacts between residues of two aligned protein molecules. It is the measure of fraction of C_α-C_α pair distances that are similar between two structures. Q value of 1 (coloured blue)

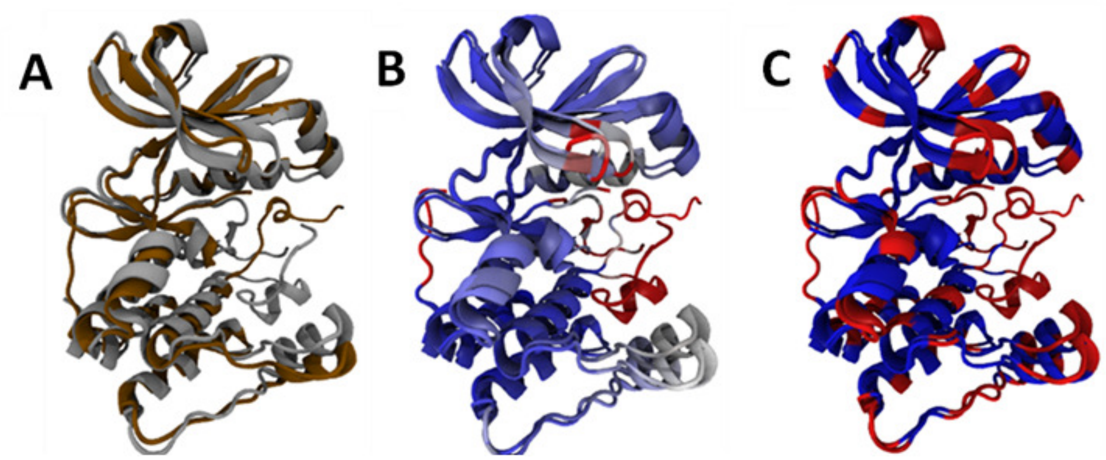

Figure 3.6: (A) Structural alignment of Aurora A (grey, PDB ID: 1MQ4)[30] and Aurora B (brown, PDB ID 4AF3 [36]). (B) The aligned protein molecules are colored according to their structure conservation by Q per residue value. (C) The aligned protein molecules are colored according to their sequence conservation. Blue indicated high sequence conservation and red means very low or no conservation.

indicates identical structures whereas low values (coloured red) mean low amount of C_α atoms superimposition. The SERS spectra shows large scale similarities in the bands related to aromatic amino acids as well as aliphatic side chains. The most prominent difference is the disappearance of the 1002 cm^{-1} phenylalanine ring breathing mode in the case of Aurora A. This could imply that the phenylalanine associated with the residues of Aurora A binding to the nanoparticle could be away from the surface of the nanoparticles or are differently oriented in case of Aurora A. Interestingly, the amide band positions in Aurora A and B indicate attachment through the β-sheet domain for both the proteins (schematic shown in Figure 3.7 and sequence alignment shown in figure 3.8. The β sheet region is coloured in yellow). The difference of 4 cm^{-1} can be attributed to the difference in the strength of binding to the nanoparticle surface. Also the intensity of modes of different aromatic amino acids as well as aliphatic side chains also changes as seen in the difference spectrum in Figure 3.3 (inset). The 804 cm^{-1} peak of tyrosine and the 1349 cm^{-1} backbone vibration mode have prominent differences. The difference in the SERS spectra of Aurora A and Aurora B inspite of their high structural similarity highlights its high sensitivity and specificity in binding to the nanoparticles.

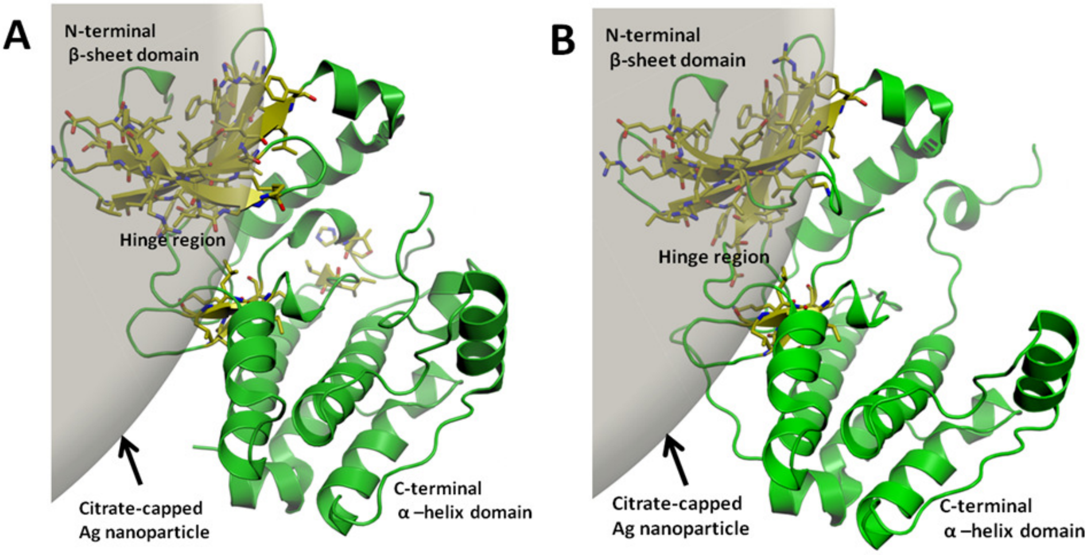

Figure 3.7: Attachment of (A) Aurora A and (B) Aurora B to silver nanoparticle surface.

3.3.7 SERS of Aurora kinases in presence of colloid aggregating agent

Addition of salt solutions like NaCl and KCl aggregates the nanoparticles and the protein molecules are absorbed into this aggregate. The enhancement of SERS signal on addition of anions is due to the aggregation of nanoparticles leading to enhanced plasmon coupling. The activated colloids also increase the charge transfer pathway between the metal and the protein, which contributes to the chemical

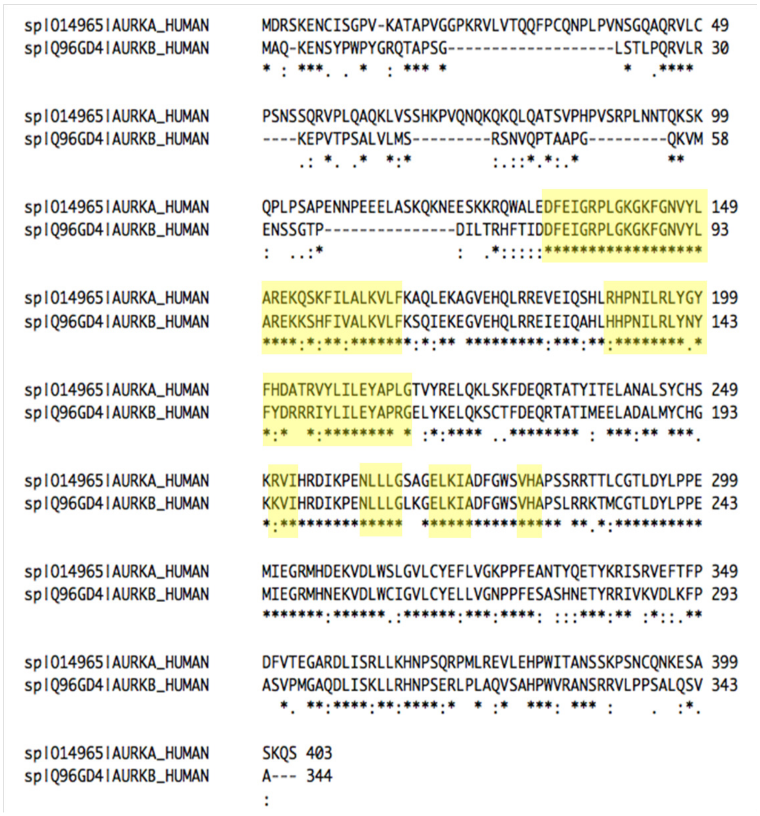

```
sp|O14965|AURKA_HUMAN      MDRSKENCISGPV-KATAPVGGPKRVLVTQQFPCQNPLPVNSGQAQRVLC 49
sp|Q96GD4|AURKB_HUMAN      MAQ-KENSYPWPYGRQTAPSG-------------------LSTLPQRVLR 30
                           * : ***. . *  : *** *                    *  .****

sp|O14965|AURKA_HUMAN      PSNSSQRVPLQAQKLVSSHKPVQNQKQKQLQATSVPHPVSRPLNNTQKSK 99
sp|Q96GD4|AURKB_HUMAN      ----KEPVTPSALVLMS---------RSNVQPTAAPG---------QKVM 58
                               .: *. .*  *:*         :.::*.*:.*          **

sp|O14965|AURKA_HUMAN      QPLPSAPENNPEEELASKQKNEESKKRQWALEDFEIGRPLGKGKFGNVYL 149
sp|Q96GD4|AURKB_HUMAN      ENSSGTP---------------DILTRHFTIDDFEIGRPLGKGKFGNVYL 93
                           :  ..:*               :  .*::::******************

sp|O14965|AURKA_HUMAN      AREKQSKFILALKVLFKAQLEKAGVEHQLRREVEIQSHLRHPNILRLYGY 199
sp|Q96GD4|AURKB_HUMAN      AREKKSHFIVALKVLFKSQIEKEGVEHQLRREIEIQAHLHHPNILRLYNY 143
                           ****:*:**:*******:*:** *********:***:**:********.*

sp|O14965|AURKA_HUMAN      FHDATRVYLILEYAPLGTVYRELQKLSKFDEQRTATYITELANALSYCHS 249
sp|Q96GD4|AURKB_HUMAN      FYDRRRIYLILEYAPRGELYKELQKSCTFDEQRTATIMEELADALMYCHG 193
                           *:*  *:******** * :*:**** ..******** : ***:** ***.

sp|O14965|AURKA_HUMAN      KRVIHRDIKPENLLLGSAGELKIADFGWSVHAPSSRRTTLCGTLDYLPPE 299
sp|Q96GD4|AURKB_HUMAN      KKVIHRDIKPENLLLGLKGELKIADFGWSVHAPSLRRKTMCGTLDYLPPE 243
                           *:**************  **************** **.*:**********

sp|O14965|AURKA_HUMAN      MIEGRMHDEKVDLWSLGVLCYEFLVGKPPFEANTYQETYKRISRVEFTFP 349
sp|Q96GD4|AURKB_HUMAN      MIEGRMHNEKVDLWCIGVLCYELLVGNPPFESASHNETYRRIVKVDLKFP 293
                           *******:******.:******:***:****: :::***:** :*::.**

sp|O14965|AURKA_HUMAN      DFVTEGARDLISRLLKHNPSQRPMLREVLEHPWITANSSKPSNCQNKESA 399
sp|Q96GD4|AURKB_HUMAN      ASVPMGAQDLISKLLRHNPSERLPLAQVSAHPWVRANSRRVLPPSALQSV 343
                             *. **:****:**:****:*  * :*  ***: *** :    .  :*.

sp|O14965|AURKA_HUMAN      SKQS 403
sp|Q96GD4|AURKB_HUMAN      A--- 344
                           :
```

Figure 3.8: Clustal W alignment of Human Aurora A and Human Aurora B primary sequences. The β-sheet region is highlighted in yellow.

enhancement. The addition of anions also leads to reorientation of the protein molecules on the surface of the nanoparticles. SERS spectra with high signal to noise ratio could be obtained even at a low concentration of 20 nM of the kinase proteins. Since the SERS spectrum of a protein is sensitive to its orientation to the plasmonic surface, changes in intensities of various modes as well as appearance of modes are expected. On addition of NaCl solution at a concentration of 5 mM an overall increase in SERS enhancement was observed. SERS done with and without addition of NaCl solution showed large scale similarities in terms of peak positions. We see new modes appearing at 665 and 998 cm^{-1} in Aurora A and 679 cm^{-1} in Aurora B (Figure 3.9).

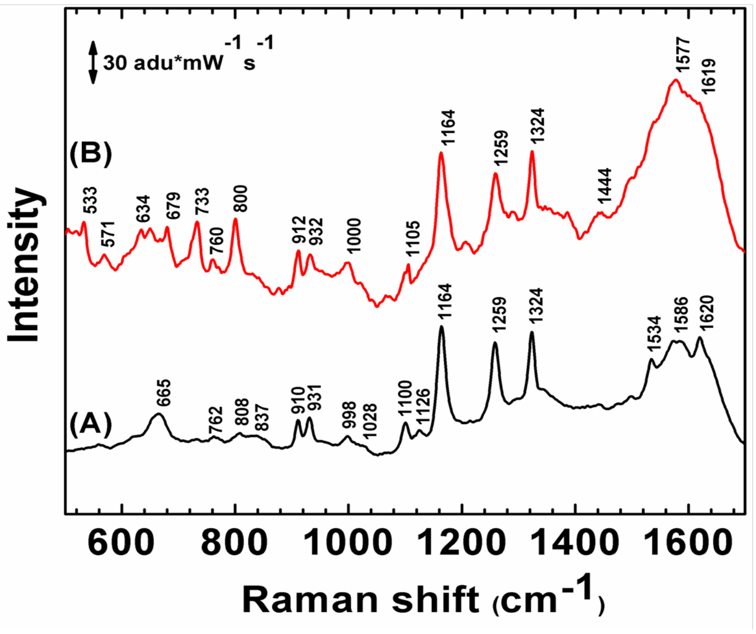

Figure 3.9: SERS spectrum of (A) Aurora A and (B) Aurora B on NaCl aggregated Ag colloid.

The appearance of 998 cm^{-1} band, which is absent in case of Aurora A SERS in non-aggregated colloid, is the symmetric ring breathing mode of phenylalanine indicating change in original attachment site or multiple attachment sites of proteins to the nanoparticles. The shift of 25 cm^{-1} in phenylalanine ring breathing modes (around 1000 cm^{-1}) as well as the ring breathing modes of tyrosine (around 800 cm^{-1}) in both Aurora A and B is due to the difference in the strength of interaction of the residues as well as the subtle differences in orientations of the residues to the nanoparticles surface. The peaks 665 cm^{-1} in case of Aurora A and 679 cm^{-1} in Aurora B SERS can be assigned to B_{3g} and B_{2g} modes whose enhancements are dependent on the orientation of the ring. We observe a significant loss in the intensity of the band at 1349 cm^{-1} in both Aurora A and Aurora B in case of colloid aggregation, which is also an indication of the change in orientation of the protein. Thus chloride ions effect can be used to obtain additional chemical information about the proteins using SERS.

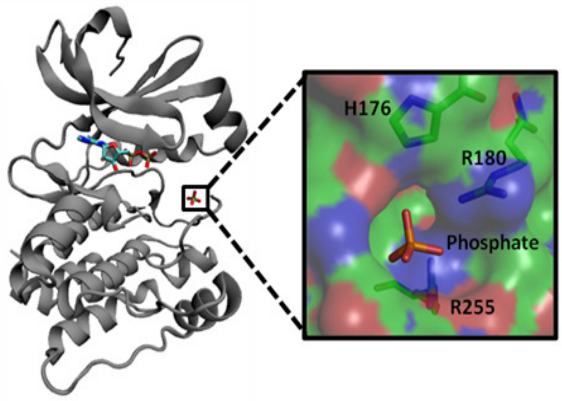

Figure 3.10: Crystal structure of Aurora A (1MQ4) complexed with ADP. The bound ADP is shown as sticks. The phosphate ion is highlighted by a square and the surface representation shows its surface binding mode.

3.3.8 Detection of autophosphorylation in Aurora A

The Aurora kinases get autophosphorylated during the course of their catalytic activity [32]. This is a very significant process as it enhances the enzyme activity. In general, protein phosphorylation is a significant step in numerous biological processes such as cell cycle, immune response, signal transduction etc. Since kinases are the targets for anticancer drugs, it is important to specifically detect phosphorylation in order to identify agents which regulate them. Although several commercial technologies are available for kinase assays, there is a need for a highly sensitive technique which is simple to use, cost effective and also less time consuming. In Aurora A as seen in the crystal structure, a free phosphate is bound near T288 in a surface pocket created by the side chains of the amino acids R180, H176 and R255 [32] (see Figure 3.10). This phosphate bound structure is similar to the catalytically active conformation. Therefore the phosphate ion lies in the position of the native phosphorylation site of the Aurora A.

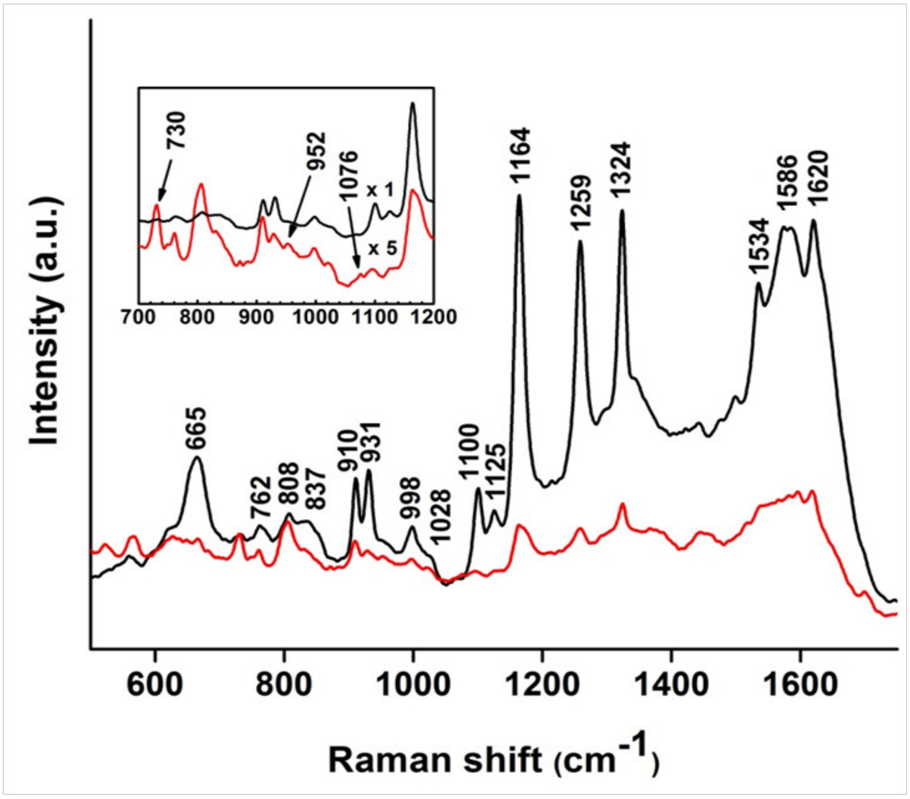

Figure 3.11: (A) SERS of Aurora A (black) and autophosphorylated Aurora A (red). (Inset) SERS spectra of Aurora A (black) and autophosphorylated Aurora A (red) multiplied five times.

Interestingly, SERS performed using aggregated colloid on Aurora A and autophosphorylated Aurora A showed observable spectral differences (see Figure 3.11). It should be noted that aggregated colloids have multiple binding sites, useful for such studies and these experiments were performed at nM concentration of protein in physiological condition (active state) which makes this much more sensitive and simple compared to competing technologies. Two weak bands at 952 and 1076 cm^{-1} appeared in the spectrum of phosphorylated protein. These bands can be assigned to stretch band of phosphate group [43; 44]. The occurrence of these bands is consistent with that reported in literature for Raman studies of phosphorylated proteins like α-casein [43]. The 952 and 1076 cm^{-1} modes are due to the dibasic (-$OPO_3{}^{2-}$) and the monobasic (-OPO_3H^-) forms of phosphate. The intensities of these bands are strongly dependent on the pH of the solution. The presence of both these bands indicates the presence of mixed forms of the phosphate, both the monobasic and dibasic forms. There is a significant drop in the intensity of amide bands at 1620, 1524 and 1259 cm^{-1}. Many ring modes of aromatic amino acids undergo change in intensities, such as the ring mode of tyrosine at 665 cm^{-1}. A new band comes up at 730 cm^{-1} which is due to the adenosine ring vibration of the molecule in the ATP binding region of the kinase protein [45]. This mode can be seen in the SERS of only ATP molecule (see Figure 3.12). Hence, it is possible to detect the bound catalytic intermediates using SERS. It opens an opportunity to employ SERS for the investigation of catalytic processes in other physiologically important proteins.

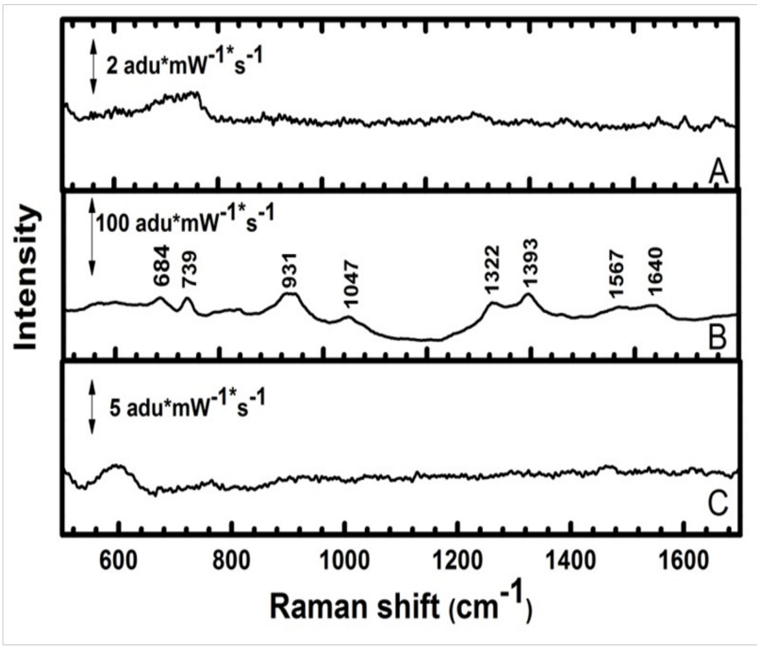

Figure 3.12: SERS spectrum of (A) Ag nanoparticles, (B) 1 mM ATP solution and (C) protein buffer.

3.4 Conclusion

We have used highly sensitive SERS to study the protein kinases Aurora A and Aurora B. The aqueous phase spectra are dominated by amide bands and bands from aromatic amino acids. Amide band analysis shows that the proteins are attached to the nanoparticles predominantly through the antiparallel β-sheet strands. The two homologous proteins could be differentiated by subtle differences in their SERS spectra which corroborates the high sensitivity of this technique. Addition of NaCl solution to the colloids causes aggregation providing greater SERS enhancement of the proteins without changing the spectra drastically. Aurora kinase being a cancer therapeutic target, the study opens up new avenues. Complete understanding of the SERS spectra helps in using it as a simple tool to study potential small molecule-protein interaction leading to drug discovery. In this work, we have demonstrated an important application of SERS by using it for detection of autophosphorylation in Aurora A. The overall decrease of SERS intensity and the appearance of bands at 952 and 1076 cm^{-1} provided direct evidence of the existence of phosphate anion bound to the protein. The presence of a band at 730 cm^{-1} also shows the presence of the adenosine ring of the moiety present in the ATP binding region of the protein, thus providing the proof of the enzymatic process facilitated by the kinase protein. For the first time SERS study is being employed in the detection of phosphorylation in a full length protein in nanomolar concentration in physiological conditions which paves the way for the studies of other proteomic modification using this direct and highly sensitive technique.

CHAPTER 4

INTERACTION OF SMALL MOLECULE INHIBITORS WITH AURORA KINASES PROBED BY SERS

This chapter constitutes the following publication:

SERS and MD simulation studies of a specific inhibitor for Aurora Kinase A shows the emergence of a potential drug discovery tool

Soumik Siddhanta, Dhanasekaran Karthigeyan, Tapas K. Kundu, Chandrabhas Narayana et. al.

Proceedings of National Academy of Sciences, USA. doi: 10.1073/pnas.1402695111

4.1 Motivation

Elucidating the mechanism of binding of small molecules to proteins is imperative in drug discovery process as well as to increase the potency and find new targets for already existing drugs. In the previous chapter we have shown that specific structural information can be obtained from the proteins through SERS. In this chapter we show the utility of this technique to find new drug targets, obtain information about their binding to proteins and highlight its probable use as a screening technique for future applications. In this direction, we have investigated the action of few dihydropyridine compounds and their inhibitory activity on oncogenic Aurora Kinases. Interestingly, one of such molecule, Felodipine is found to selectively inhibit the activity of Aurora A kinase.

As discussed in the earlier chapter, Aurora Kinases are potential targets for anti-cancer drugs as it is found to be over-expressed in certain types of cancers. There are numerous reports on inhibitors of Aurora Kinases in the literature, but very small number of them are selective inhibitors. This is due to the similar structure of these kinases. They have a difference of only four residues in their active site. The development of selective inhibitors can lead to many mechanistic studies and will help to elucidate the mechanism of action of these kinases in more detail. The dihydropyridine molecule felodipine, which was found to be exhibiting selective inhibition of Aurora A kinase was therefore of interest, in spite of the fact that it was a micromolar inhibitor rather than a nanomolar one, which is a norm for a drug to be highly potent. Therefore, the next step was to eventually find out the mechanism of inhibition of the molecule.

As discussed in the earlier chapter, the common techniques to study protein-drug interactions are NMR, X-ray crystallography, fluorescence, surface plasmon resonance, etc. But these techniques have their own problems like the requirement of a high protein concentration or incorporation of secondary tagged-molecules. A lot of these problems can be circumvented by using SERS but it is scarcely used to study protein systems. SERS have been traditionally used for ultrasensitive detection of analytes, but recently it has been utilized to study protein-small molecule interactions [46]. A common problem of SERS is that it does not give complete vibrational information like Resonant Raman. But it is interesting to find out what can be derived out of the minimal information that SERS can provide us. The questions that can be asked are whether SERS can detect the binding of molecules to the proteins? Can SERS distinguish between competitive and non-competitive mode of action of a drug molecule? Can SERS predict specific changes in protein structure upon ligand binding? If SERS can answer these questions, it can be really potent technique for studying protein-ligand interactions. When combined with computational simulation techniques like Molecular Dynamics (MD) to validate the experimental findings, it can be used for screening of drugs for therapeutic applications. This would also facilitate the development of tip-enhanced Raman spectroscopy (TERS) for imaging of small molecule interactions. This SERS-MD simulations combination can be used for screening of small molecules with lower protein concentrations and in lesser time. Also, in case of SERS, the experiments can be done in aqueous environments and without the requirement of any specialized sample preparation techniques.

To demonstrate these points, we have studied the interaction of Felodipine, a specific inhibitor of Aurora A kinase through SERS by a label free manner in physiological conditions. We have shown that SERS could predict the surface binding mode of this molecule with the protein, which was further validated through molecular docking and molecular dynamics simulations. The uniqueness of these binding pockets lie in the fact that through these very same pockets, coactivator proteins like TPX2 and INCENP binds to Aurora A and Aurora B respectively, in-vivo. The possibility to predict binding position of ligands to proteins without the need of crystallizing the complex and conducting X-ray studies has opened up possibility of a new technique.

4.2 Experimental and simulation details

Raman and SERS studies: Purification of enzymes and preparation of samples were done using the methods described in chapters 2 and 3. All the Raman and SERS measurements were done with custom built Raman spectrometer described in chapter 2.

Kinase assay: 1 μg of bacterially expressed recombinant histone H3 was incubated along with baculovirus-expressed His$_6$-tagged protein (40 ng) in a 30μl reaction mixture containing 50mM tris.HCl, 100 mM NaCl, 0.1 mM EDTA, 10mM MgCl$_2$, 0.2% 2- mercaptoethanol and [γ^{32}P] ATP (specific activity 3.5 cimM^{-1}). The reaction was carried out either in the presence of DMSO or the indicated small molecules at 30°C for 10 mins. The reaction was stopped over ice and the reaction mixture was precipitated using 25% TCA and resolved using 15% PAGE followed by autoradiography.

Molecular docking and dynamics simulations: Aurora A crystallographic structure (PDB entry 1MQ4 [30]) was used as initial coordinates for MD simulations. Electronic structure optimized (B3LYP/6-31G*) ligand and the protein forms the model complex in our simulation, while the respective interactions were duly approximated by CHARMM22 force field and parameters [47] including CMAP correction [48]. Before performing the molecular dynamics of ligand bonded protein, the ligand-free crystallographic protein structure was neutralized with counter-ions and solvated with 32016 TIP3P[49] water molecules. Particle Mesh Ewald (PME) was used to calculate long range electrostatic interactions [50]. The SHAKE method was applied for fixing the bond lengths involving a hydrogen atom [51]. A box cut-off length of 20 Å was adapted during the simulation. After 500000 steps of energy-minimization 1 ns equilibration MD run was performed with 1 fs unit step size at 300 K. Subsequently the obtained structure was used for molecular docking studies. The optimized structures of ligands felodipine was docked into the proteins using the Autodock (version 4.2) [52]. AutoDockTools 1.5.4 [53] was used to set the rotatable bonds and add polar hydrogen. Gasteiger charge was added and the protein was embedded in a grid box of size 126 x 126 x 126 centered on the mass center of the protein and with a grid spacing of 0.375 Å. Lamarckian genetic algorithm (LGA) [54] was used to generate the ligand-protein conformation. Docking was carried out with population size of 300 with 25 x 10^5 evaluations and maximum of 27000 generations. A cluster analysis was carried out with the root-mean-square deviation tolerance as 2 Å. The best conformation is considered to be the one having lowest free binding energy or the lowest energy conformation of the most populated cluster. A finer docking was done keeping the centre of the smaller grid box of dimension 60 x 60 x 60 on the ligand position of the lowest binding energy. The resulting coordinates of the docked complex were secured for further MD runs. The whole complex was energy minimized, that followed with a 2 ns MD run at 300 K to capture the necessary dynamics for our simulation studies. All essential MD procedures were carried out with NAMD program suite (version 2.8) [55]. Corresponding topology and parameter files for MD were generated with paratool plugin in VMD visualization program [56], while the missing hydrogens of the crystal structure were incorporated with the help of psfgen plugin. Ab-initio electronic structure of the ligand was obtained using Gaussian 03 [57].

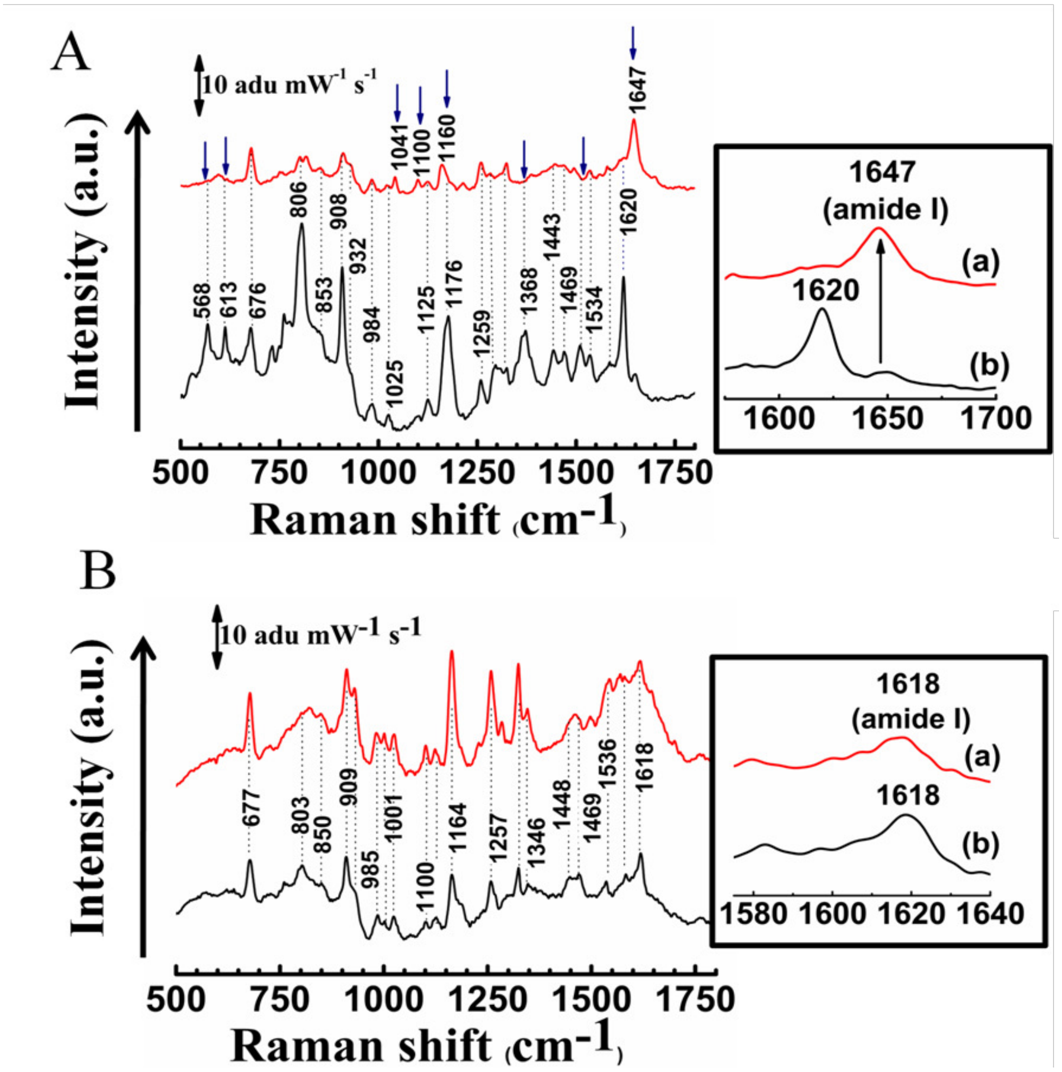

Figure 4.1: SERS of (A) Aurora A (black) and Aurora A complexed with felodipine (red). (B) Aurora B (black) and Aurora B complexed with felodipine (red). Insets show the magnified amide I region.

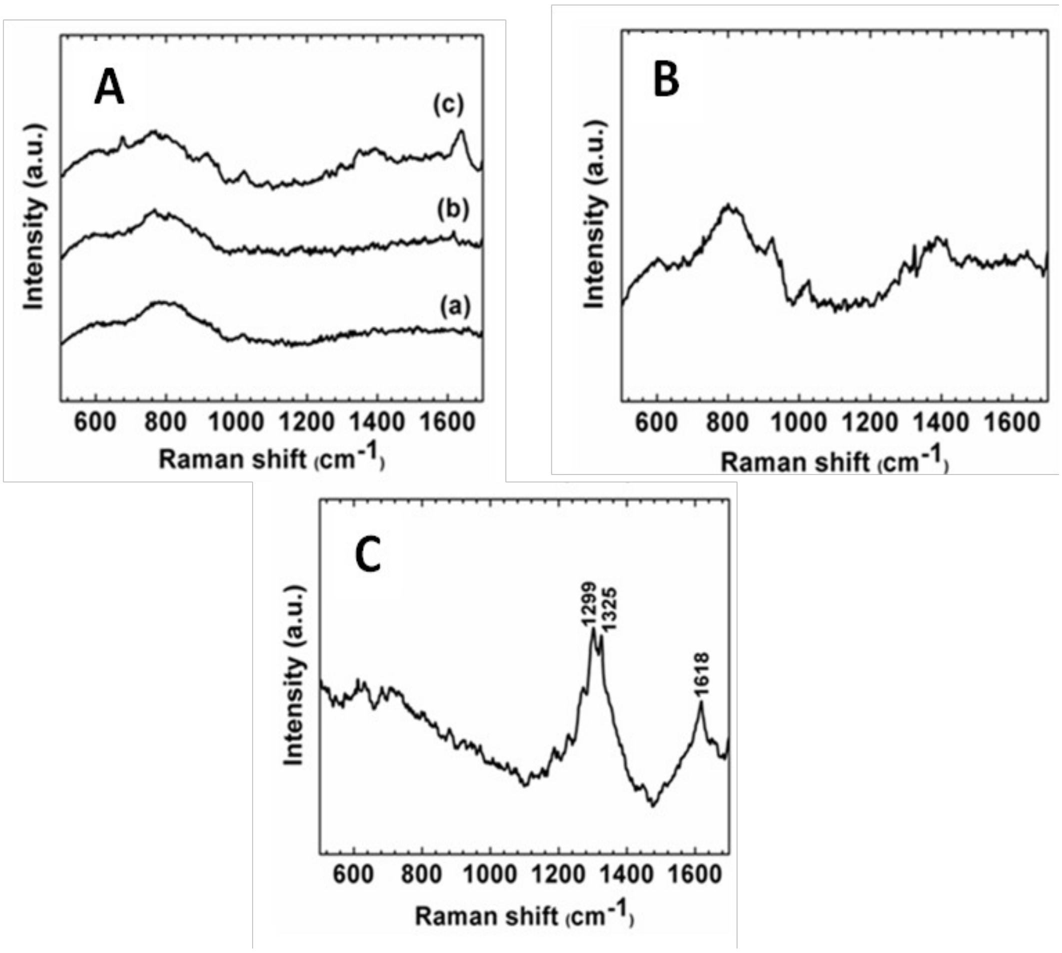

Figure 4.2: (A) a,b and c represent SERS spectra of Ag nanoparticles solution, protein buffer and DMSO containing protein buffer respectively. (B) SERS of 20 mM felodipine solution. (C) SERS of 20mM reversine solution.

4.3 Results and discussions

4.3.1 Prediction of surface binding through SERS

Figure 4.1 shows the SERS of both Aurora A and Aurora B kinases in free form and in complex with felodipine. The detailed band assignments of Aurora A and Aurora B have been done in chapter 3. It is interesting to see that there is a significant change in the spectrum of the Aurora A complexed with felodipine in comparison to that of Aurora B. SERS spectra of Aurora A and Aurora B are dominated by bands from aromatic amino acids Phe, Tyr, His and Trp and also amide modes. To compare the effects of felodipine with a known inhibitor we performed the experiments with reversine, an ATP analog, which is a competitive inhibitor for both Aurora A and Aurora B. We have performed SERS of the buffer, DMSO and also the individual small molecules (Figure 4.2) and found out that these molecules do not contribute to the SERS spectra of the protein or the protein complex.

The most significant change in the spectrum of Aurora A-felodipine was the shift in maximum intensity of amide I band from 1620 cm^{-1} to 1647 cm^{-1}. The 1620 cm^{-1} band almost diminishes, but the 1647 cm^{-1} band intensity increases. We believe that Felodipine is a surface binding ligand and the change in the amide I band could have originated due to the change in the position of the attachment of the protein on the silver surface (see schematic in Figure 4.3).

In order to confirm this hypothesis, we have performed SERS of Aurora Kinases A and B complexed with reversine. Since reversine is not a surface binding

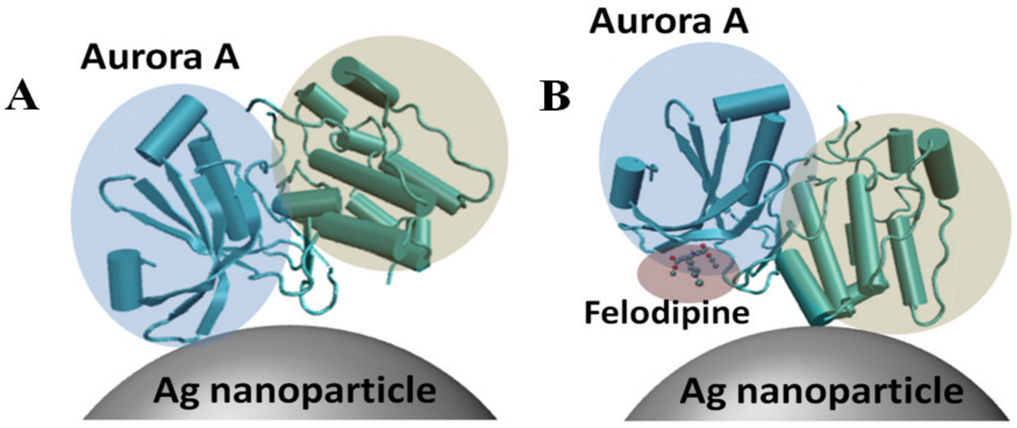

Figure 4.3: (A) Mode of attachment of Aurora A to Ag nanoparticle. (B) Change in orientation of Aurora A on the Ag nanoparticle surface on complexation with felodipine.

molecule, it should not change the orientation of the protein to the surface of the nanoparticle (see Figure 4.4). As expected, the SERS spectra (see Figure 4.5) showed that, the amide I band shows no shift in position on Aurora A complexing with reversine, and in addition we don't see any significant changes in the protein SERS spectra for both Aurora A and Aurora B. But it is interesting to see the appearance of two new peaks around 1297 and 1369 cm^{-1} in case of Aurora A-reversine complex and around 1293 and 1376 cm^{-1} in Aurora B-reversine complex. It is interesting to see the new peaks match very well with the strong peaks of the SERS spectra of Reversine at high concentrations. Although at lower concentrations (used in complexation for SERS experiments) reversine didn't show observable peaks. Therefore it is evident that surface binding of Felodipine could be manifested as a non-competitive inhibition since these binding pockets might be far from the catalytic active site.

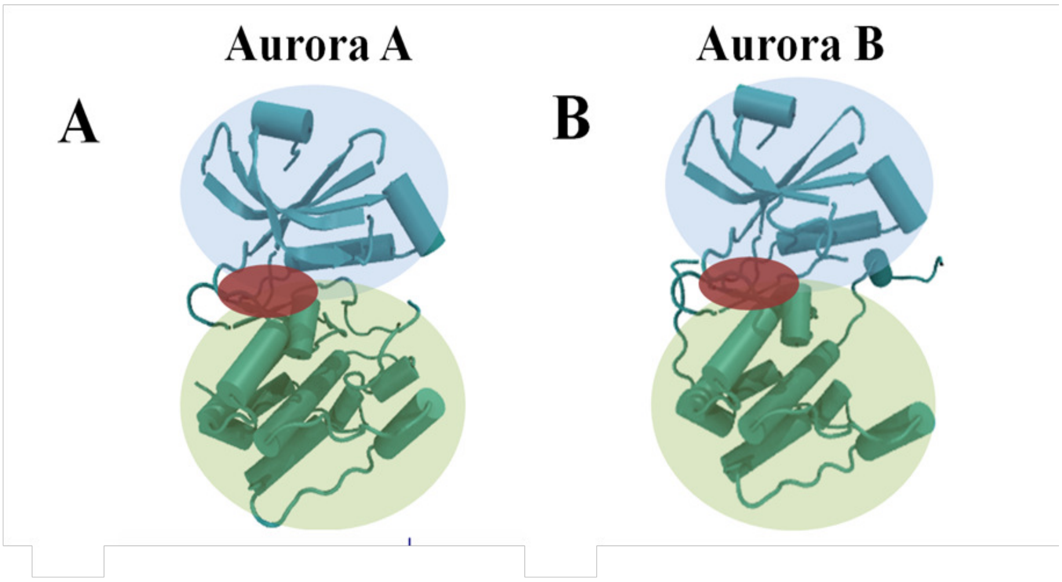

Figure 4.4: The schematics (A) and (B) shows the binding sites of reversine to Aurora A and Aurora B respectively.

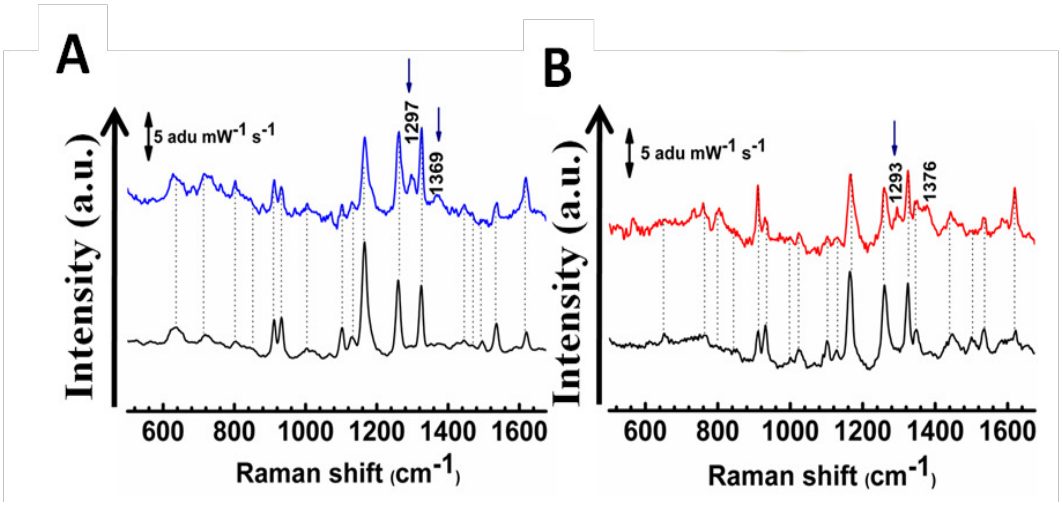

Figure 4.5: (A) SERS of Aurora A (black) and Aurora A complexed with reversine (blue). (B) SERS of Aurora B (black) and Aurora B complexed with reversine (red).

4.4 Molecular docking and molecular dynamics simulations

To validate the binding of Felodipine to Aurora A, we performed molecular docking to predict the binding site and orientation of felodipine. The molecular docking is based on the reported crystal structure of Aurora A [30] and Aurora B [36]. The docking results show that in most favourable docked pose (lowest binding energy, see Figure 4.6 A) felodipine binds to a solvent exposed pocket just outside the hinge region and it is in hydrophobic contact with the residues Phe157, Ile158 and Tyr212 (Figure 4.6 B).

The carbonyl group of the felodipine forms a hydrogen bond with the -NH group of the residue Tyr212 (hydrogen bond distance 2.05 Å) which is a part of the solvent exposed front pocket of Aurora A that lies to the flipside of the catalytic pocket in the hinge region (amino acid residues 210-216). In case of Aurora B, the pocket is unfavourable for binding of felodipine as it is narrower by around 2 Å

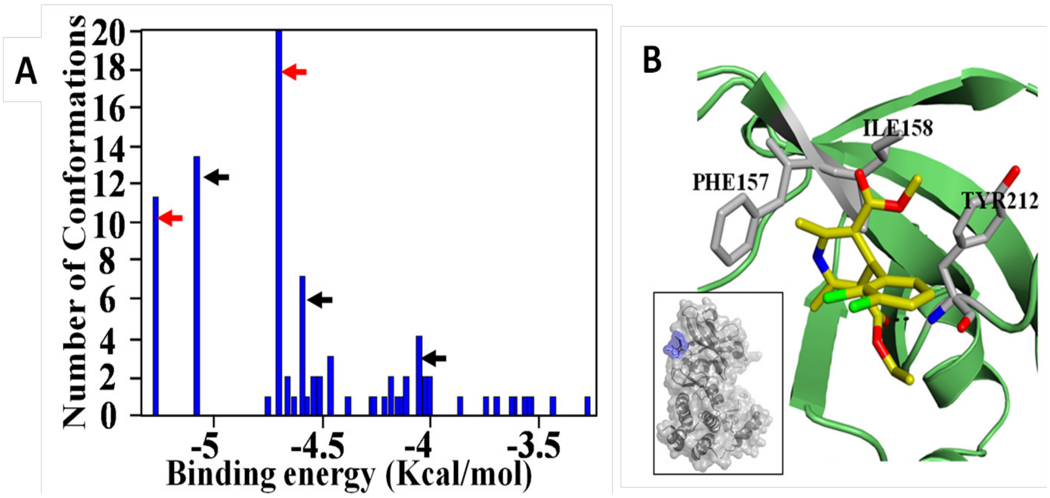

Figure 4.6: (A) Conformational clustering histogram generated from molecular docking of felodipine to Aurora A through Autodock. The red arrows represent the conformations of felodipine bound to the hinge pocket (first site) while the black arrows represent binding over the N-terminal pocket (second site). (B) The bound configuration of Felodipine to Aurora A through residue TYR212 (dashed line). The carbon, oxygen, nitrogen and chlorine atoms are colored in yellow, red, blue and green respectively. The inset shows the felodipine(blue) attached to the surface of Aurora A near the hinge region.

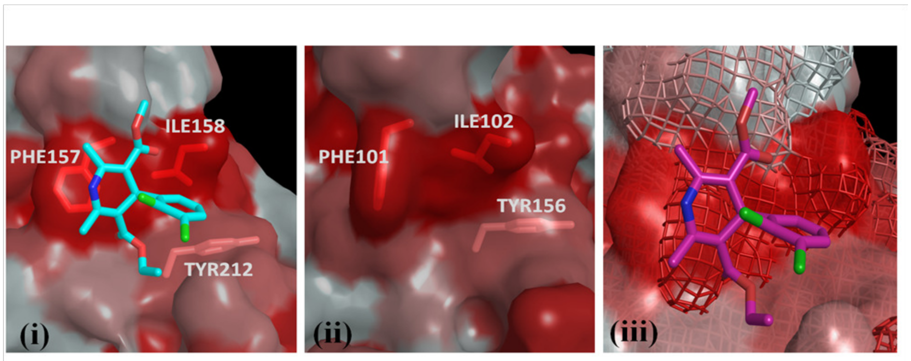

Figure 4.7: (i) Binding mode of felodipine to the hydrophobic pocket of Aurora A. (ii) The corresponding hydrophobic pocket in Aurora B. (iii) The superimposed pockets of Aurora A (solid surface) and Aurora B (in wireframe) shows the difference in shapes of the pockets. The surface is colored according to the Eisenberg's hydrophobicity index.

(Figure 4.7). This is due to the tilt of residues Phe101 and Ile102. This change in hydrophobic pocket is due to the differences in the nature of the residues lining the hydrophobic pocket (Lys156 for Aurora A and His 100 for its counterpart, Aurora B). Docking has a disadvantage, as it considers the protein to be rigid. But in reality, proteins have flexible parts which shows movement in the solvent. Also, docking does not take water molecules into account. We performed molecular dynamics (MD) simulations to take into account the flexibility of the protein. The 2 ns MD simulation of the Aurora A-felodipine complex showed the stability of the binding between felodipine and Aurora A. The RMSD distances between the centre of masses of felodipine and the residues Phe157, Ile158, Tyr212 and the protein shows constant values over the entire duration of simulation (Figure 4.8A).

We also checked the stability of felodipine in the second most favorable site

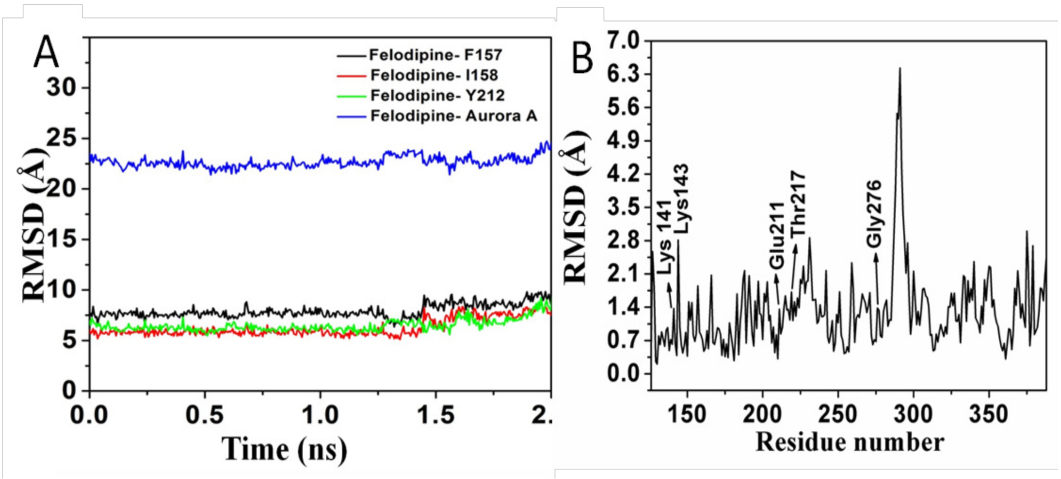

Figure 4.8: (A) The RMSD distance variation with time of felodipine and different residues. (B) The RMSD distances between the residue numbers between the initial and final frames of the 2ns MD simulation of Aurora A-felodipine complex. Key residues lining the active site are labeled.

predicted by Autodock. Here, the felodipine molecule was hydrogen bonded to the residues His 201 and Trp 128 (see Figure 4.9A). MD simulations predicted the stability of the molecule in this site. Incidentally, this second site is also different in shape from Aurora A (see Figure 4.9B). We also investigated the stability of

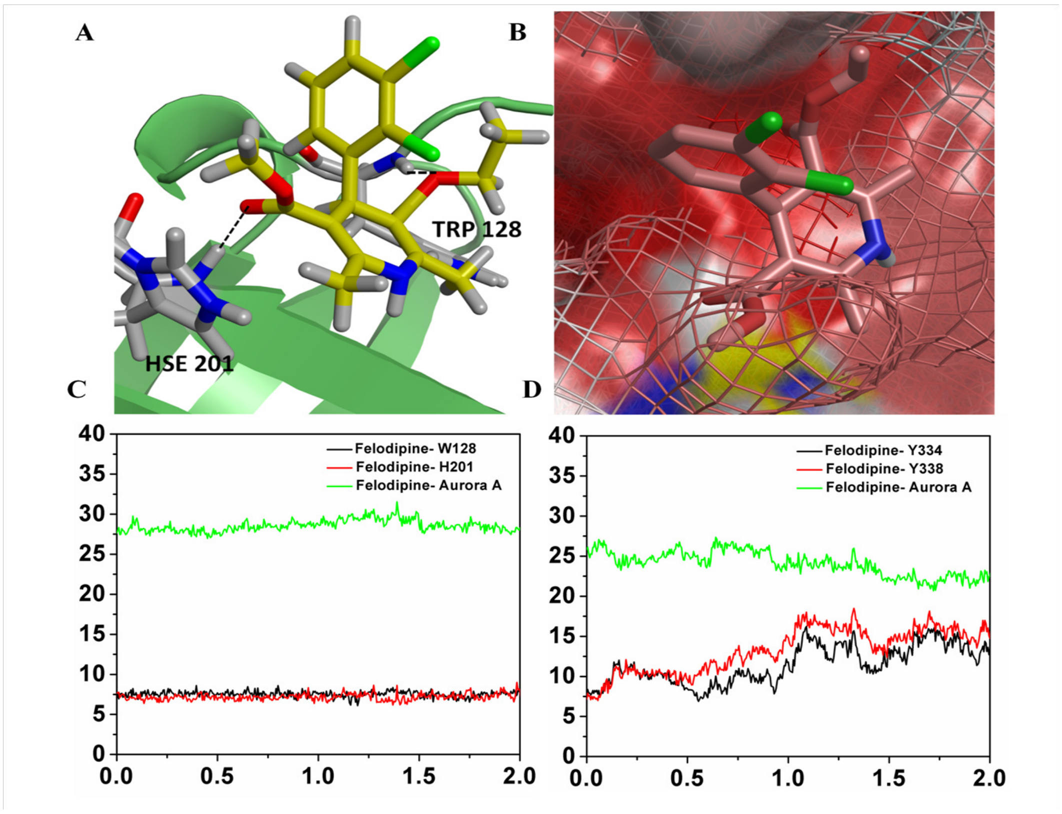

Figure 4.9: (A) The bound configuration of Felodipine to Aurora A to the second binding site. The residues colored in grey are in hydrophobic interaction with Felodipine. Felodipine is hydrogen bonded to Aurora A through residue TRP128 and HSE201 with hydrogen bond distances of 2.1 and 1.9 Å respectively (represented by dashed line). The carbon, oxygen, nitrogen and chlorine atoms are colored in yellow, red, blue and green respectively. (B) The surface binding mode of Felodipine to the second binding site. The Aurora B surface is shown in wireframe to highlight the difference in the hydrophobic binding site. (C) RMSD distances between Felodipine and residues TRP128 (black), HSE201 (red) and Aurora A (green) for the second binding site. (D) RMSD distances between Felodipine and residues TYR334 (black), TYR338 (red) and Aurora A (green) for the third site.

felodipine in a third site, which was similar to first site, in having two aromatic residues coming together (Tyr 334, Tyr 338). In the course of MD, the molecule didn't show stable trajectory within this pocket (see Figure 4.9D). Thus from the MD simulations, it is evident that there are two binding sites for felodipine. This has been further verified by isothermal calorimetry experiments. On comparing the structures of Aurora A after 2 ns simulation with and without felodipine revealed a number of conformational changes lining the active site that might affect the binding of ATP in the ATP binding pocket (Figure 4.8B).The residues 141-143 in the glycine rich loop are highly flexible and Lys143 has been particularly shown to be a switch in case of ATP binding in Aurora A [58]. The kinetic studies also indicate that unlike most of the ATP competitive inhibitors reported for Aurora kinase, felodipine is a mixed type inhibitor. These observations indicate that SERS based prediction of a non-competitive mode of inhibition is indeed true.

The second site of binding of felodipine to Aurora A is unique since the coactivator protein TPX2 makes van der Waals contact with Trp 128 in case of Aurora A. Similarly INCENP, the specific coactivator of Aurora B binds in the vicinity of both these pockets (the hinge and the N terminal pocket) over Aurora B but not in case of Aurora A. This confirms the uniqueness of these two hydrophobic binding sites which can be targeted for selective inhibition of Aurora Kinases.

4.5 Point mutation studies

The binding of felodipine to Aurora A was also validated through mutation studies. The point mutations of Tyr 212, Phe 157 and Ile 158 were performed and results show a decrease in inhibitory activity up to 37 % from complete inhibition of Aurora A by felodipine. The SERS of Aurora A mutants complexed with felodipine were performed (see Figure 4.10). In case of combinations mutant Ile 158 and Tyr 212 as well as Phe 157 and Tyr 212, significant changes in the SERS spectra were not observed, as compared to the changes seen in the wild type SERS spectra. The mutations in the second site did not show a decrease in kinase activity. Therefore, the second site does not contribute to the inhibition of Aurora A by felopine, but it still binds to this site. In case of point mutant His 201, large scale changes in SERS spectrum could be observed with complexed with felodipine. This includes the shift of amide I band from 1625 cm^{-1} to 1645 cm^{-1}, indicating the shift of attachment point of nanoparticle to the α-helix domain. These changes are comparable to the SERS spectra of wild type complexed with felodipine. Hence, corroborating the previous observations that the most preferable site of felodipine binding could be the hinge pocket surrounded by the hydrophobic residues Phe 157, Ile 158 and Tyr 212.

4.6 Inhibition of Aurora Kinases by other dihydropyridine molecules: SERS studies

In order to gain more insights on the mechanism of binding of dihydropyridine molecules to Aurora Kinases and their inhibitory action, we have undertaken studies on molecules having similar structure to felodipine, but with different functional groups.

During the screening of small molecules, several dihydropyridine molecules were tested, out of which felodipine was found to be selective inhibitor of Aurora A. Two other molecules tested were amlodipine and nimodipine (see Fig 4.11). These molecules did not show inhibition of Aurora Kinases. Therefore, the SERS of Aurora A complexed with amlodipine and nimodipine (Figure 4.12) were performed as a check for the technique. The spectra of Aurora A complexed with these molecules did not show significant changes compared to that of free Aurora A. The position of amide I bands were also same. Similar observation was made in case of Aurora B complexed with amlodipine and nimodipine (Figure 4.13).

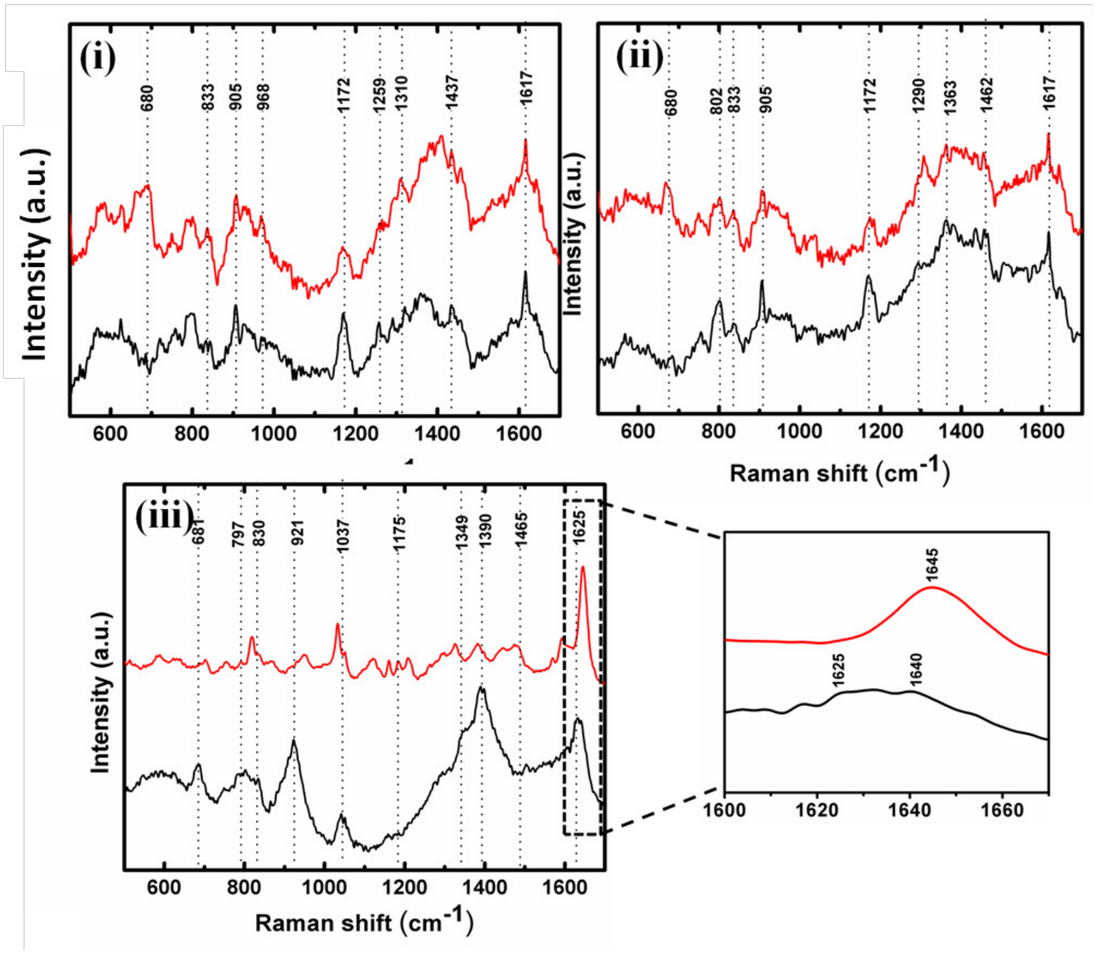

Figure 4.10: (i) SERS spectra of combinatorial mutant of Aurora A (Ile 158 and Tyr 212) in black and its complex with felodipine in red. The same is represented for the Phe 157 and Tyr 212 mutant (ii) and His 201 mutant (iii) proteins. The enlarged region highlighting the amide I region of (iii) shows the shift in amide I band from 1625 cm^{-1} to 1645 cm^{-1}.

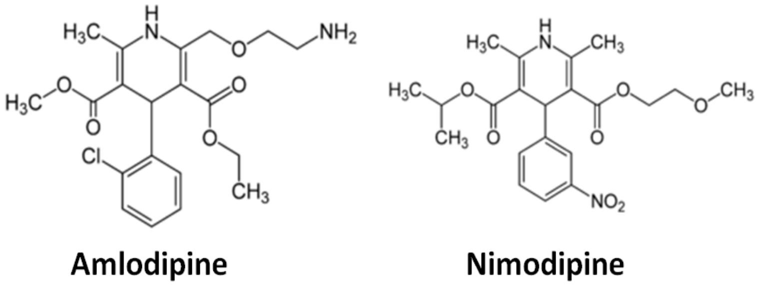

Figure 4.11: Structure of amlodipine and nimodipine

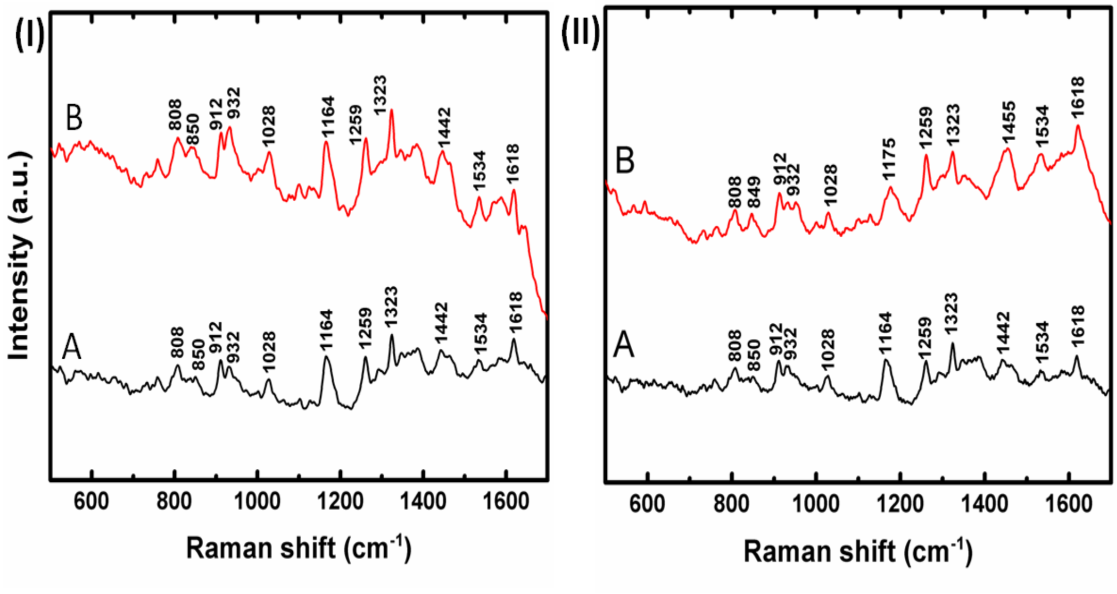

Figure 4.12: (I) SERS of Aurora A (black) and Aurora A complexed with amlodipine (red). (II) (A)SERS of Aurora A (black) and (B) Aurora A complexed with nimodipine (red).

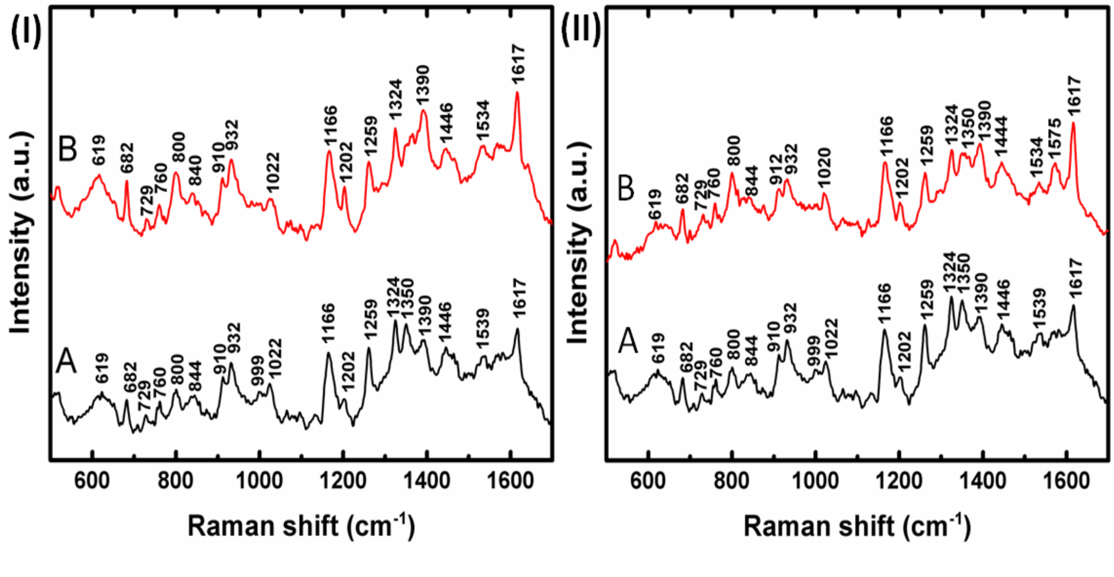

Figure 4.13: (I)SERS of Aurora B (black) and Aurora B complexed with amlodipine (red). (II) (A)SERS of Aurora B (black) and (B) Aurora B complexed with nimodipine (red).

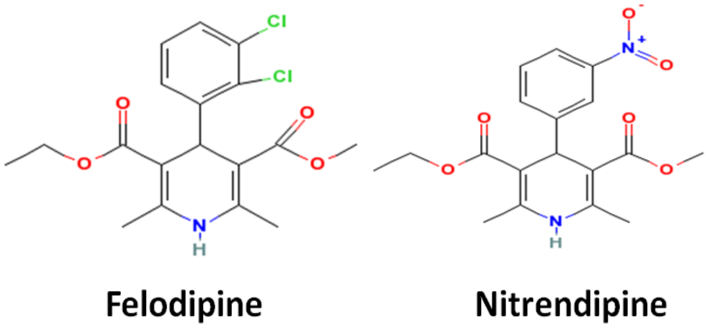

Figure 4.14: Structure of felodipine and nitrendipine

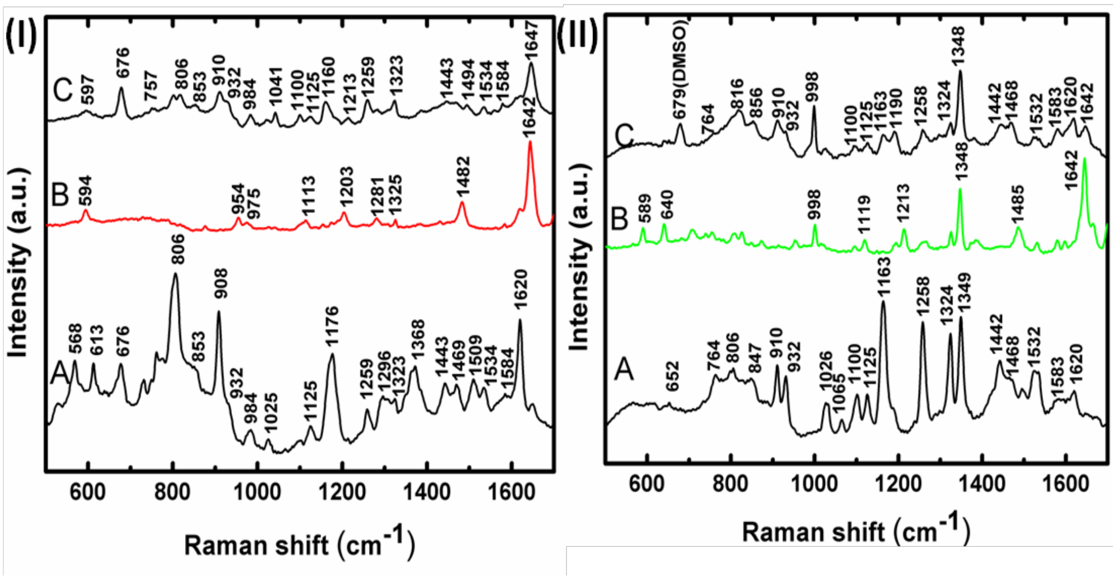

Figure 4.15: (I)(A) SERS of Aurora A, (B) Raman spectrum of felodipine and (C) SERS of complex of Aurora A-felodipine. (II) SERS of Aurora A, (B) Raman spectrum of nitrendipine and (C) SERS of complex of Aurora A-nitrendipine.

The change of orientation of the Aurora A-felodipine complex from the β-sheet region to α-helix region is due to the highly hydrophobic nature of felodipine due to the two chlorine atoms which face away from the protein exposed to the solvent. This repels the hydrated surface of silver away from the bound molecule. To test

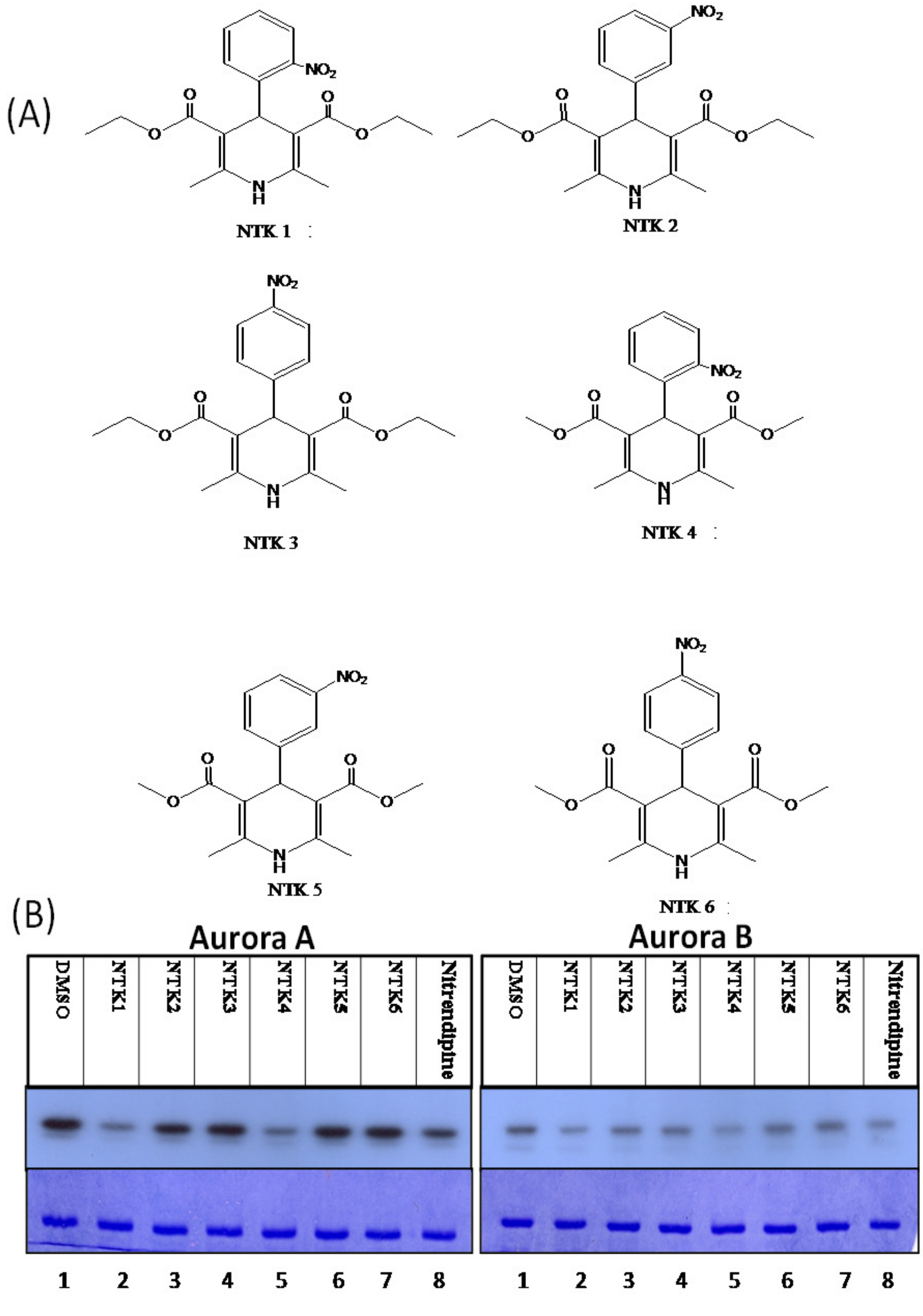

Figure 4.16: (A) Molecules similar to felodipine and nitrendipine synthesized for checking their inhibitory activity on Aurora kinases. (B) Kinase assay of Aurora A (left panel) and Aurora B(right panel) using recombinant histone H3 as substrate in the presence of small molecules. The molecules present are labeled against each lane.

this hypothesis, another molecule called nitrendipine was used. Nitrendipine has the same structure as felodipine except that the chlorine atoms are replaced by a single nitro group (Figure 4.14). SERS results (see Figure 4.15) show that there is no contribution from felodipine to the spectra of Aurora A-felodipine complex. Whereas, in case of Aurora A-nitrendipine complex, the spectrum is a superposition of spectrum of free Aurora A and Raman spectrum of nitrendipine. In case of nitrendipine, due to the absence of hydrophobic chlorine atoms, the protein molecule does not change its orientation on the surface of the nanoparticle. Therefore the nitrendipine molecule gets sandwiched between the protein and the nanoparticle surface. Thus we see its contribution in the spectrum of the protein complex specially the strong peaks (998, 1348 cm^{-1}) and also the amide I region. The amide I region shows two peaks, one from the protein (1620 cm^{-1}) and one from nitrendipine itself (1642 cm^{-1}).

As we have seen in the case of inhibition of Aurora A by felodipine, the shape of the molecule as well as the hydrophobic pocket is crucial for binding of the molecule. Therefore, molecules similar to felodipine and nitrendipine were synthesized by Kundu et. al. (see Figure 4.16 (A)). These molecules had two major differences from felodipine and nitrendipine. The chlorine atoms were replaced by nitro group and their positions were varied from ortho, meta as well as para positions. Secondly, the lengths of side chains attached to the pyridine ring were varied. The action of these molecules on the kinase activities of Aurora A and Aurora B were checked. Interestingly, out of the six molecules, two molecules showed the maximum reduction of kinase activity. These molecules were NTK1 and NTK4 (see Figure 4.16 B). The molecules NTK1, NTK4 and to a certain extent nitrendipine inhibited both Aurora A and Aurora B. The inhibition of nitrendipine was lesser than that of NTK1 and NTK4.

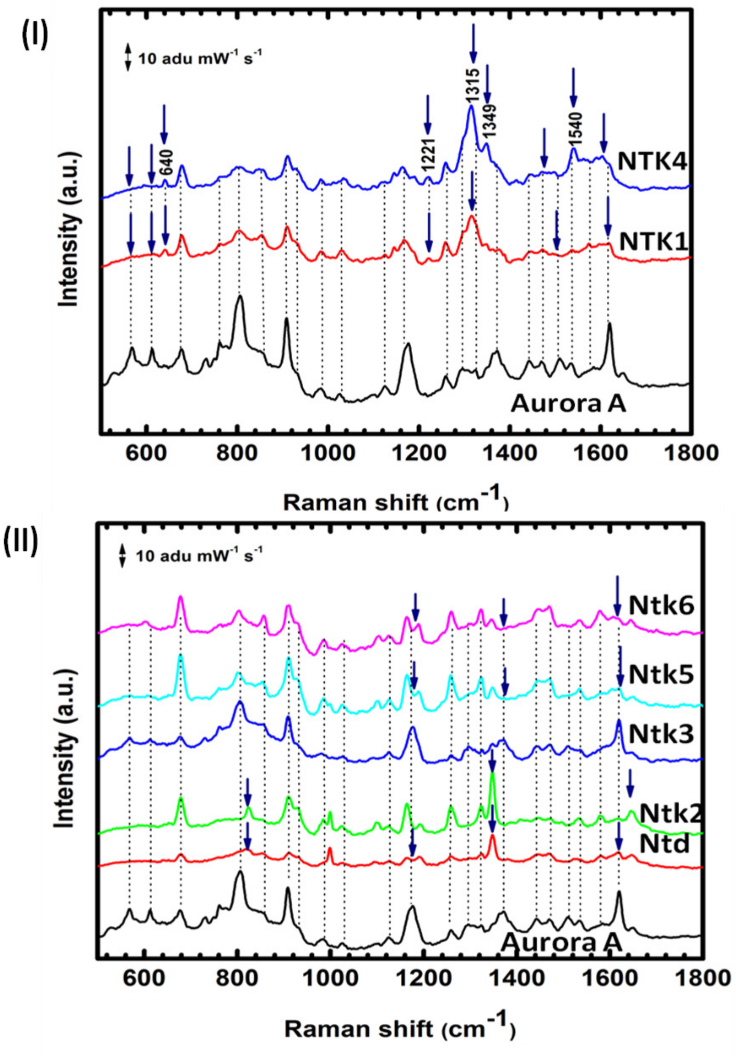

Figure 4.17: (I) SERS of Aurora A and its complexes with NTK1 and NTK4 (indicated as NTK1 and NTK4). (II) SERS of Aurora A and its complexes with nitrendipine, Ntk2, Ntk3, Ntk5 and Ntk6 (indicated as Ntd, Ntk2, Ntk3, Ntk5 and Ntk6 respectively). Major variations in peaks are indicated by blue arrows.

The SERS experiments using all these molecules were performed to see whether there is a correspondence with the biochemical experiments. Interestingly, the SERS experiments followed exactly the same trend as the kinase assays. There were large scale changes in the SERS spectra of Aurora A complexed with NTK1 and NTK4 (see Figure 4.17 I) compared to that of free Aurora A and its complex

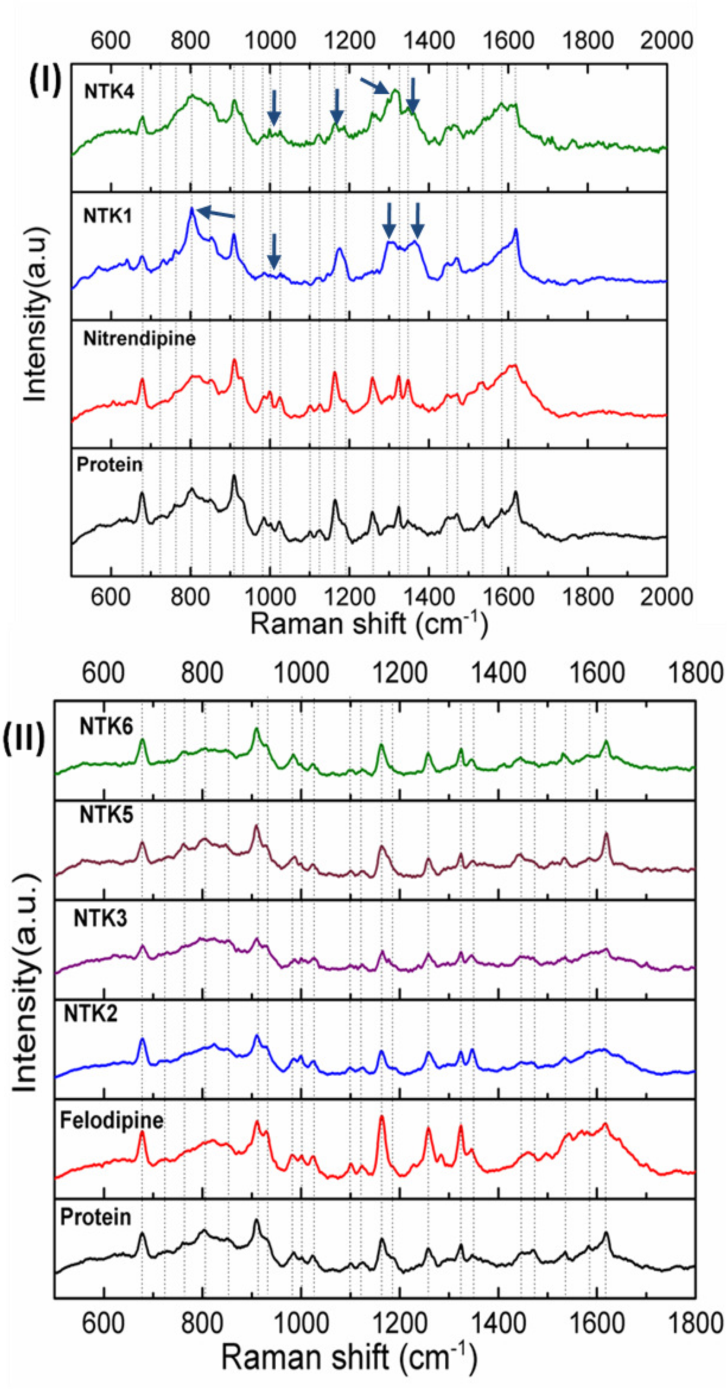

Figure 4.18: (I) SERS of Aurora B and its complexes with NTK1 and NTK4 (indicated as NTK1 and NTK4). (II) SERS of Aurora B and its complexes with nitrendipine, Ntk2, Ntk3, Ntk5 and Ntk6 (indicated as Ntd, Ntk2, Ntk3, Ntk5 and Ntk6 respectively). Major variation in peaks are indicated by blue arrows.

with the other molecules NTK2, NTK3, NTK5 and NTK6(see Figure 4.17 II). The maximum changes occurred in the 1200-1400 cm^{-1} and also in the 750-850 cm^{-1} regions. The amide I region was also affected. The amide I band intensity was greatly reduced. These large scale changes might be due to the overlapping of bands from the attached molecule itself, which gets sandwiched between the protein and the nanoparticle. The other reason might be the structural changes brought about by the molecule on interacting with the protein, as seen from the reduction in amide I band. In case of other molecules, the changes in the spectra were not very pronounced. The minor changes in the spectra can be attributed to the non-specific or weak binding of the molecules to the protein. Even the kinase assays does show traces of inhibition from the other molecules too. Thus it demonstrates the sensitivity of SERS technique and highlights the excellent correspondence to the biochemical techniques.

In case of Aurora B too, similar observations were made in the SERS spectra (see Figure 4.18). In case of NTK1 and NTK4, there were large scale changes, particularly in the regions of 1200-1400 cm^{-1} and 750-850 cm^{-1}. The amide I intensities were also diminished. In contrast we see that in case of nitrendipine, which had a low inhibition of kinase activity of Aurora B, showed intermediate changes in SERS spectrum, not as drastic as that of NTK1 and NTK4. In case of other molecules, there are no drastic changes in the SERS spectra compared to that of free Aurora B.

The probable reason for the inhibitory activity of NTK1 and NTK4 comes from the position of their nitro group. The nitro group lies in the ortho position in these molecules, which is not in the case of other molecules. The presence of the nitro group provides steric hindrance and prevents the free rotation of the molecule about the bond between the phenyl and the pyridine ring. The perpendicular orientation of the rings with respect to each other is favourable for docking of the molecule to the hydrophobic pocket near the active site of Aurora Kinase. Therefore, the NTK1 and NTK4 molecules are more potent as inhibitors. Also, the fixed nature of the phenyl ring paves the way for the hydrophilic interactions of the nitro and other oxygen containing groups with different hydrophilic patches on the surface of the protein. This might be responsible for the loss of selectivity of these molecules and hence they inhibit the activity of both Aurora A and Aurora B. We also observe that the side chain length is not a factor in binding of these molecules. Both NTK1 and NTK4 have side chain differing by a single CH_2 group, but it does not prevent the molecules from binding to the proteins.

4.7 Conclusion

We have demonstrated that, SERS having limited vibrational information of the protein compared to normal Raman or resonant Raman, can be used to gain vital insight into binding of small molecules to the protein.With the help of the structural information and in conjunction with molecular docking and molecular dynamics studies, the binding site of small molecules can be pin-pointed and validated. This is one of the most significant step in developing potential drug candidates. This has been demonstrated by taking felodipine as a model compound and further validated through studies on related molecules having different functional group. SERS can distinguish between surface binding and competitive binding of small molecules to the protein. Point mutations carried on Aurora kinase based on these results confirm the binding mechanism predicted by these techniques. Hence, SERS, molecular docking and molecular dynamics can combine together to provide an alternative to the currently used methods for studying small molecule-protein binding, which is a prerequisite for drug discovery process.

CHAPTER 5

LYSINE ACETYLTRANSFERASE KAT3B/P300 INHIBITION BY 1,4-NAPTHOQUINONES: A SERS STUDY

This chapter constitutes the following publication:

Napthoquinones Mediated Inhibition of Lysine Acetyltransferase KAT3B/p300, Basis for Non-toxic inhibitor synthesis

Mohankrishna Dalvoy Vasudevarao, Pushpak Mizhar, Sujata Kumari, Somnath Mandal, **Soumik Siddhanta**, Mahadeva M. M. Swamy, Stephanie Kaypee, Ravindra C Kodihalli, Amrita Banerjee, Chandrabhas narayana, Dipak Dasgupta and Tapas K Kundu

Journal of Biological Chemistry, doi: 10.1074/jbc.M113.486522 (2014).

5.1 Motivation

Proliferation and differentiation of cells and other cellular processes are controlled by regulation of gene expression. In this process, messenger RNA (mRNA) is synthesized from the DNA which contains genetic information. This process occurs after the recruitment of pre-initiation complex, histone modifying factors and transcription factors to specific regions of the chromatin [59]. The histone modifications like methylation and acetylation takes place which play a critical role in gene regulation. Defects in these histone modifications have been identified in cases of pathological conditions ranging from cancer to autoimmune diseases [60]. KAT3B/p300 (or only p300 as referred to in the later parts of this chapter) is also called as the histone acetyl transferase (HAT) which transfers an acetyl group to the ϵ-amino group of a lysine residue in the histone [61; 62]. p300 is a 300 kDa protein and has 2414 amino acids. The protein has several domains having important functions. These domains are (1) bromodomain, frequently found in mammalian HAT, (2) three cysteine-histidine (CH)-rich domains, (3) a KIX domain and (4) an ADA2-homology domain. Both N- and C- terminal regions of p300 can act as transcriptional activator and the HAT domain resides in the central region of the protein. This modular organization allows p300 to provide a scaffold for assembly of multi-component transcription co-activator complexes. p300 has been implicated in a number of diverse biological functions including proliferation, cell cycle regulation, apoptosis, differentiation and DNA damage response [63–65]. It also acts as a transcriptional coactivator of a number of nuclear proteins like oncoproteins (e.g., myb, jun, fos), transforming viral proteins and tumor suppressor proteins like p53 [66]. It is also known to acetylate nonhistone proteins like NPM1, which activates the chromatin mediated transcription in an acetylation-dependent manner [67]. The role of its contribution in many functions and in several diseases makes it a novel target for therapeutics. Although the functional aspects of this important transcriptional activator is widely studied, the structure-function relationship is yet to be established. One of the reasons for this is the absence of the full crystal structure of the full length p300 protein molecule. But significant developments have been made since the availability of crystal structure of the HAT domain of p300. Recently the crystal structure of the catalytic core including the bromodomain, CH2 region and HAT domain has been reported [68]. Due to this, it has been possible to predict the mechanism of the activation or inhibition of p300 HAT activity. Significant work on structure-activity relationship have been done with the help of the ultrasensitive spectroscopic technique SERS [46]. Since this protein is expressed in very minute quantities, it is difficult to perform normal Raman experiments.

Previous work related to SERS studies on p300 and its complexes with various activators [46] and inhibitors [69] have yielded interesting results on its structure-activity relationship. SERS have been used to probe the acetylation-induced specific structural changes in the HAT domain of p300 [70]. On comparing the normal HAT and the acetylated HAT domain there were changes in modes corresponding to the symmetric streching of COO^- (1369 cm^{-1}) and amide III (1294 cm^{-1}), ν_{9a} of Phe (1184 cm^{-1}) and asymmetric stretching of $C_\alpha CN$ (1132 cm^{-1}). The intensities of these modes changed and their positions shifted to lower wavenumbers due to acetylation. The softening of the modes were a result of the disruption of hydrogen bonding. SERS was also used to probe the activation of p300 HAT by small molecule which induces a change in structure [69]. Two molecules N-(4-chloro- 3- trifluoromethyl-phenyl)-2-ethoxy-benzamide(CTB) and N-(4-chloro-3-trifluro-methyl- phenyl)-2-ethoxy-6 pentadecyl-benzamide(CTPB),which are synthesized from salicylic acid and anacardic acid were found by Kundu and coworkers to enhance the activity of p300 HAT domain. The SERS data obtained from the complex of CTB and CTPB with p300 show one-to-one correspondence with the biochemical data. In case of CTPB the intensities of bands at 1654, 1335 and 960 cm^{-1} change, indicating binding of the molecule to the amide groups of α helix and β sheet. These changes were greater when CTB was bound to p300 with the complete disappearance of the band at 1623 cm^{-1}. These changes in the SERS spectra showed the change of structure of the p300 molecule on binding of these activator molecules. SERS was also used to probe p300 specific inhibitors which also brought about changes in the structure of the enzyme. Garcinol and isogarcinol (IG) and their derivatives were found to inhibit p300 HAT activity by Kundu and coworkers [70]. SERS was useful in elucidating the differential structural changes brought about by binding of specific and non-specific inhibitors to p300 [70].

In this work, we investigate another small molecule inhibitor of p300 HAT activity. This small molecule inhibitor (PTK1) [71] is an improvement over its earlier variant (Plumbagin) which was also a HAT inhibitor [72] but was found to be toxic to cells. The molecule plumbagin was found to promote oligomerization of the p300 protein through the exposed cystein groups. The direct evidence of this oligomerization through formation of disulphide bonds were found through SERS experiments. The inhibitory effect of PTK1 was also observed through spectral changes in SERS spectrum of the complex of PTK1 and p300. The details of the results and their correspondence to the biochemical assays is shown in the subsequent sections. This establishes SERS as a powerful candidate to study surface effects in proteins.

5.2 Experimental methods and docking

The SERS of p300 and p300 complexed with PTK1 and plumbagin were preformed by the experimental methods described in chapter 2. The Crystal structure of p300 KAT domain was extracted from the Protein Data Bank using the code 3BIY [73]. The structure of the inhibitor PTK1 was optimized using the GAUSSIAN 03 program [57]. Docking analysis was performed with Autodock 4.2 using a Lamarkian genetic algorithm. A grid spacing of 0.375 was used. Docking was performed with a flexible ligand with 100 GA runs, a population size of 300, 25×10^5 evaluations and a maximum of 27000 generations [52]. The analysis of conformations was conducted based on clusters generated using MGL Autodock tools version 1.5.4. Figures were created using the PyMOL molecular graphics system [74].

5.3 SERS of KAT3B/p300

The SERS spectrum of KAT3B/p300 (see Figure 5.1) was dominated by modes from aromatic amino acids Phe, Tyr, Trp and His, amide modes and other aliphatic side chain vibrations (see Table 5.1). The p300 is a 300 kDa protein consisting of 2414 amino acids. The structure of HAT domain is known and it consists of 317 amino acids. The HAT domain consists of a central β sheet composed of seven β strands which is surrounded by nine α helices. The C subdomain consists of three of the α helices and the last β sheet. Overall the p300 consists of the C and N subdomains. The details of peak assignment of p300 is given below. The peak assignments are based on the SERS study published previously [75].

Polypeptide backbone vibrations: As seen in the SERS spectrum of p300,

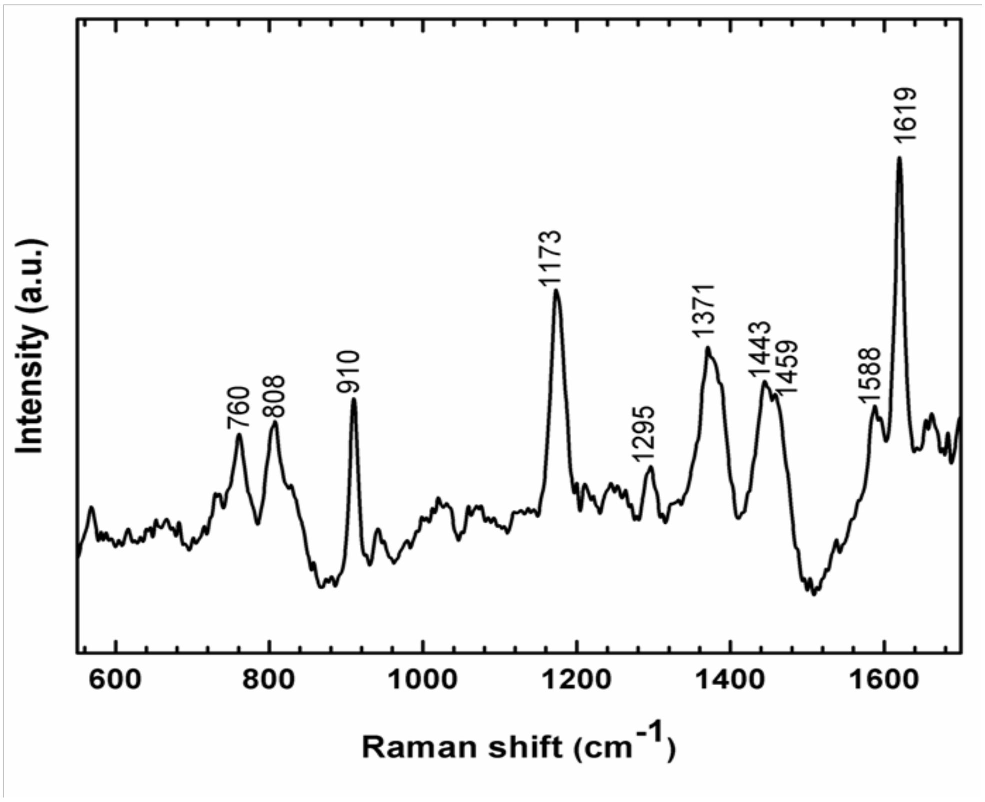

Figure 5.1: SERS of full length p300

the amide I and III lie at the positions 1619 and 1295 cm^{-1} respectively. The amide I position is much lower than conventional α -helix region. But it is known that the position of amide I band shifts to lower wavenumber on interaction with the surface of silver nanoparticles. Therefore this amide I position is certainly not conclusive when assigning the secondary structural component which is in close contact with the surface of the nanoparticle. The amide III position from 1260-1310 cm^{-1} corresponds to α helix. But this assignment of secondary structure is certainly not conclusive without the availability of the full crystal structure of the protein. Similar amide I and III positions occur in case of antiparallel β-sheets too. This amide I band is confirmed by deuteration studies where it shifted to lower wavenumbers and also amide III shifts from 1296 to 950 cm^{-1} [75].

Table 5.1: Assignment of Raman bands in the SERS spectra of p300

Raman shift(cm^{-1})	Band assignment
1619	amide I
1588	$\nu_{as}(\mathrm{COO}^-)$, His, Trp, and/or Phe(ν_{8a})
1459	His and/or Trp
1443	His and/or Trp
1388	$\nu_s(\mathrm{COO}^-)$
1371	$\nu(\mathrm{CH})$
1295	amide-III (α helix) and/or $\delta(\mathrm{CC}_\alpha\mathrm{H})$
1173	Tyr and/or Phe(ν_{9a})
941	$\nu(\mathrm{C\text{-}COO}^-)/\alpha$-helical C-C stretching vibration
910	$\nu(\mathrm{C\text{-}COO}^-)$
808	Tyr and/or $\nu_{as}(\mathrm{C\text{-}S\text{-}C})$
760	Trp or His
559	Trp

Vibrations associated with the aromatic side chains: The SERS spectrum of p300 is dominated by aromatic amino acid side chains. There are 12 Trp, 46 Tyr and 44 Phe present in the primary structure of p300. Trp peaks can be seen at 569, 760, 808, 1173 and 1459 cm^{-1}. Phenyl ring breathing modes or tryptophan indol ring mode cannot be observed in the SERS spectrum. This indicates that these residues are not in direct contact with the surface of the nanoparticles or are not oriented in appropriate direction for SERS enhancement.

Vibrations associated with aliphatic side chains: The carboxylate group vibrations can be seen in the SERS spectrum of p300 at 1371 and 1588 cm^{-1} and are assigned to symmetric and asymmetric stretching modes respectively. These carboxylate groups are from the amino acids aspartic acid (Asp) and glutamine (Glu) or from the C-terminus end of the protein. The C-COO$^-$ stretching modes can be seen at 910 and 941 cm^{-1}. The carbon backbone chain vibrations of the alkyl groups can also be seen in the SERS spectrum. The 1388 and 1443 cm^{-1} modes correspond to $\nu(\mathrm{CH})$ and $\delta(\mathrm{CH}_2)/\delta(\mathrm{CH})$ respectively.

5.4 SERS study of interaction of plumbagin and PTK1 with KAT3B/p300

The SERS experiments were conducted with p300 and p300 complexed with plumbagin and PTK1 by following the experimental method explained in chapter 2. The spectra of baculo-expressed full-length p300 treated with plumbagin or PTK1 showed significant changes when compared to the spectrum of p300 alone (see Figure 5.2). The amide I band at 1619 cm^{-1} was diminished in intensity moderately in the case of PTK1 but almost complete in case of plumbagin. The result suggests that the binding of the molecules induced structural changes to the protein which can be directly correlated with the extent of the interactions of the compound with the protein. The amide III band at 1295 cm^{-1} diminished in intensity. The bands in the region 1150-1550 cm^{-1} also changed in intensity in cases of both PTK1 and plumbagin. This region is mainly associated with the aromatic amino acids. This shows that the binding of the molecules changes the orientation of these amino acids with respect to the surface of the nanoparticles. The appearance of the doublet at 910-941 cm^{-1} corresponding to C-COO^{-} shows that the proteins interact with the nanoparticle surface through the carboxylate groups. The reduction in the intensity of this doublet in case of PTK1 and almost completely in case of plumbagin shows the weakening or change in interaction behaviour of the protein complex with the nanoparticle surface. In case of plumbagin, an extra peak arises at 682 cm^{-1} which is assigned to the ν_s(C-S-C) mode [76]. This mode was absent in free protein and the protein-PTK1 spectra. The appearance of this mode is a direct evidence of thiol-adduct formation which is induced by the small molecule plumbagin. The non-specific binding of plumbagin to the surface of the protein changes the protein binding site on the nanoparticle surface, thereby causing overall reduction in intensities of different modes like the C-COO$^-$ stretching modes and also other modes from aromatic or aliphatic side chains.

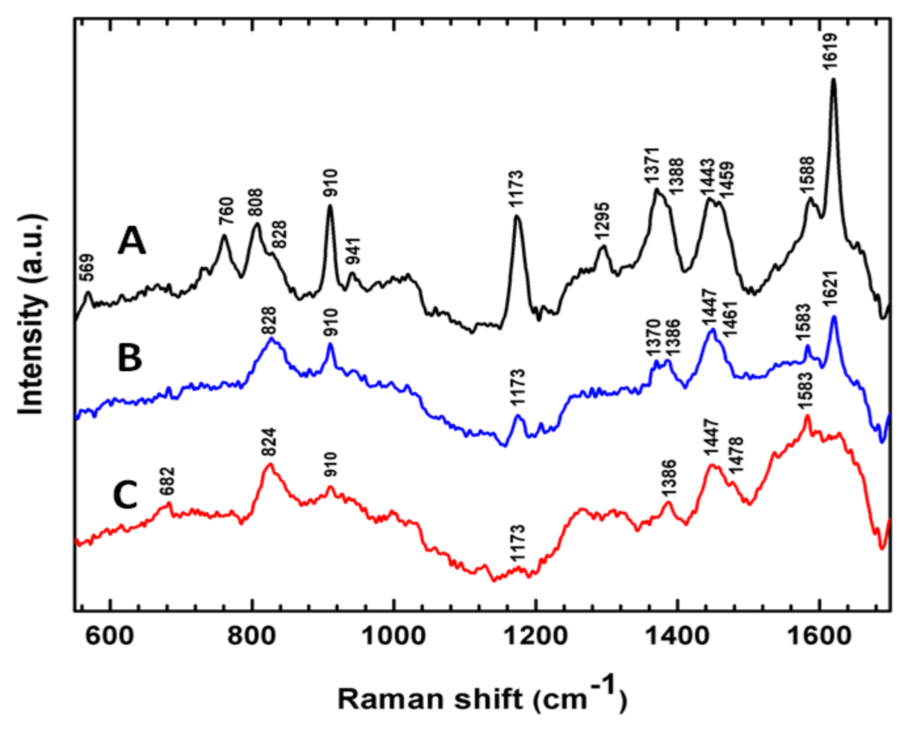

Figure 5.2: SERS of (A) full length p300, (B) p300 complexed with PTK1 and (C) p300 complexed with plumbagin. Figure adapted from [71].

5.5 Correlation of SERS with biochemical studies

Small molecule inhibitors of KAT3B/p300 are of tremendous potential not only as molecules for therapeutic uses but also to develop understanding of how KAT functions in-vivo. Kundu and coworkers had developed a napthaquinone class of KAT/HAT inhibitors [72]. These inhibitors interact directly to the HAT domain of the p300. It has been shown that the hydroxyl group of these compounds (at 5th position)are essential for their inhibitory function (see Figure 5.3). Plumbagin is one such molecule. While these inhibitors were potent in their action, they were toxic to the cells and were irreversible inhibitors. They also generated reactive oxygen species (ROS) and also reacted with thiol groups on the protein forming oligomers, thus enhancing their toxicity. It was found out that the 3rd position is essential for toxicity as plumbagin reacts with thiols through this position. Based on these observations, another molecule was synthesized with a methyl substitution in the 3rd position. The hydroxyl group at the 5th position maintains the HAT inhibitory activity. The reduced ROS generation and absence of thiol adduct formation makes the PTK1 molecule non-toxic and reversible inhibitor.

The SERS measurements also highlights the differential action of the molecules (plumbagin and PTK1) on p300 molecule. Since, the thiol adduct formation is a surface phenomenon, SERS is an ideal surface analytical technique which can detect these kind of chemical modifications. In fact, the appearance of ν_s(C-S-C) mode is a direct evidence for this kind of surface modification of protein. Also, due to the combined effect of adduct formation as well as enhanced cross linking due to ROS generation, the effect of plumbagin on p300 is more adverse than PTK1. This is reflected in the SERS spectrum of p300 complexed with plumbagin and

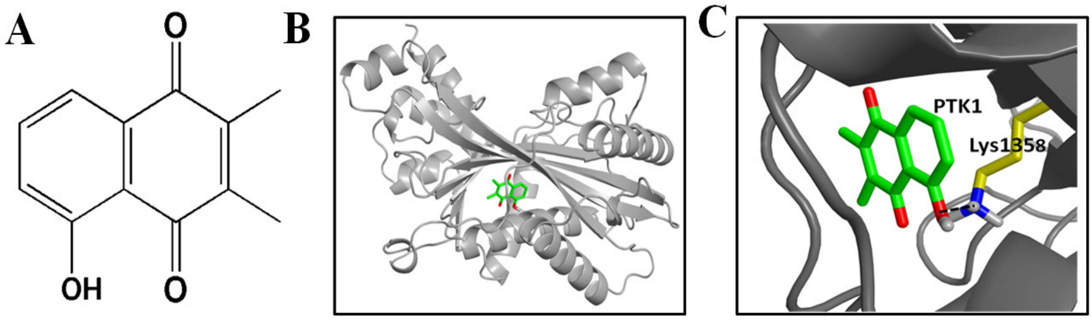

Figure 5.3: (A) The PTK1 molecule. (B) Docking of PTK1 (shown in stick representation) onto the p300 KAT domain (shown in cartoon representation). The crystal structure of the p300 KAT domain was extracted from PDB using the code 3BIY. (C) Hydrogen bonding of PTK1 molecule with Lys 1358 residue (H-bond length 2.51 shown as dotted line). Figure adapted from [71].

PTK1. The complex with plumbagin shows more widespread changes in the spectum, whereas less drastic changes are observed in case of PTK1. Thus we see that SERS has one-to-one correspondence with the biochemical assays.

5.6 Conclusion

The interaction of p300 with a toxic and non-toxic inhibitor were probed with SERS. This technique provides ways to investigate small molecule-protein interactions at low concentrations and can be used to validate biochemical assays. The changes in intensities of modes like amide I and appearance of mode corresponding to ν_s(C-S-C) vibration confirming adduct formation show that SERS can be an ideal candidate to study surface specific modifications as well as structural alterations which are manifested through spectral changes. Therefore, SERS can have applications in finding suitable candidates for therapeutic applications.

CHAPTER 6

TRYPAN BLUE INDUCED STRUCTURAL ALTERATIONS OF THE HUMAN ANTERIOR LENS CAPSULE: A RAMAN SPECTROSCOPIC INVESTIGATION

This chapter constitutes the following publication:

Trypan blue induced structural alterations of the human anterior lens capsule of cataractous lens: A Raman spectroscopic investigation

Soumik Siddhanta, Minu M. Mathen, Mathew Kurian and Chandrabhas Narayana

Manuscript under preparation

6.1 Motivation

Understanding the microstructural changes of any material at molecular or chemical level is imperative in understanding the effects of mechanical or chemical stress. For gaining a complete understanding of the effects of structure and composition on the mechanical characteristics of the material, it is essential to conduct studies at both micro and macro levels. For complex biological systems and tissues having hierarchical structures looking into ultra-structural details has been impossible with conventional techniques for strength characterization like nano-indentation and atomic force microscopy. Therefore, the use of a technique which is non-contact based as well as with a high spatial resolution is necessary to investigate complex materials at microscopic details.

Raman spectroscopy has emerged to be a powerful analytical tool in life sciences and has variety of applications in biology, medicine as well as environmental sciences for detection and characterization of biomaterials [77]. It can be used to study turbid media even like layers of living human tissue to obtain specific chemical and structural information [78]. Together with infrared spectroscopy it has been used to study the molecular level secondary structural components of tissue systems and structural changes in the events of tissue damage or diseases and other pathological factors. Raman spectroscopy has additional advantages over infrared as it is insensitive to aqueous environments commonly found in biological systems. It can be used in variety of modes and environments [79]. For biological systems the ability to tune the laser source makes it possible to bypass the inherent fluorescence of the biomolecules and water. Raman spectroscopy provides information about secondary structures of proteins and other biomolecules as well as the backbone, specific amino acids and side chain informations [20; 80; 81]. Raman spectroscopy has been recently used extensively for determining the secondary structure elements of protein [82], protein-ligand binding [83] among many other applications.

In this work, we explore the structural aspects of a basement membrane which constitutes the human lens capsule using Raman spectroscopy. The lens capsule is predominantly made up of collagen IV type of protein and completely surrounds the ocular lens [84]. One of the main roles of the lens capsule is to shape the lens and its surface curvature and also participate in accommodative mechanism [84]. In case of cataract of eye lens, capsulorhexis is performed, where a circular incision is made on to the anterior lens capsule to expose the cataractous lens prior to its extraction [85]. It is very important to visualize the lens capsule during capsulorhexis, otherwise there is a risk of radial capsule tear which might extend beyond the equator in severe cataract conditions [86]. Trypan blue, which is a common dye used in visualization of dead cells and tissues can effectively stain the anterior lens capsule making it suitable for performing capsulorhexis [87]. Histopathological studies have shown that trypan blue is accumulated selectively in the basement membrane adjacent to the epithelial layer [88]. But there have been reports of increased fragility of the anterior lens capsule on trypan blue staining [89]. Electron microscopy images of the trypan blue stained anterior lens capsule shows focal irregularities [90] and other reports using nano-indentation [91], modified rheometer [89] or material tester [92] shows significant reduction of elastic behavior and increase in stiffness although there was no significant decrease in tear resistance. The decrease in elastic property of the lens capsule can increase the risk of capsular tears and intraoperative complications [89]. Therefore it is important to know the structural alterations occurring during trypan blue staining which affects its mechanical strength.

We have performed a complete Raman spectral analysis of the anterior lens

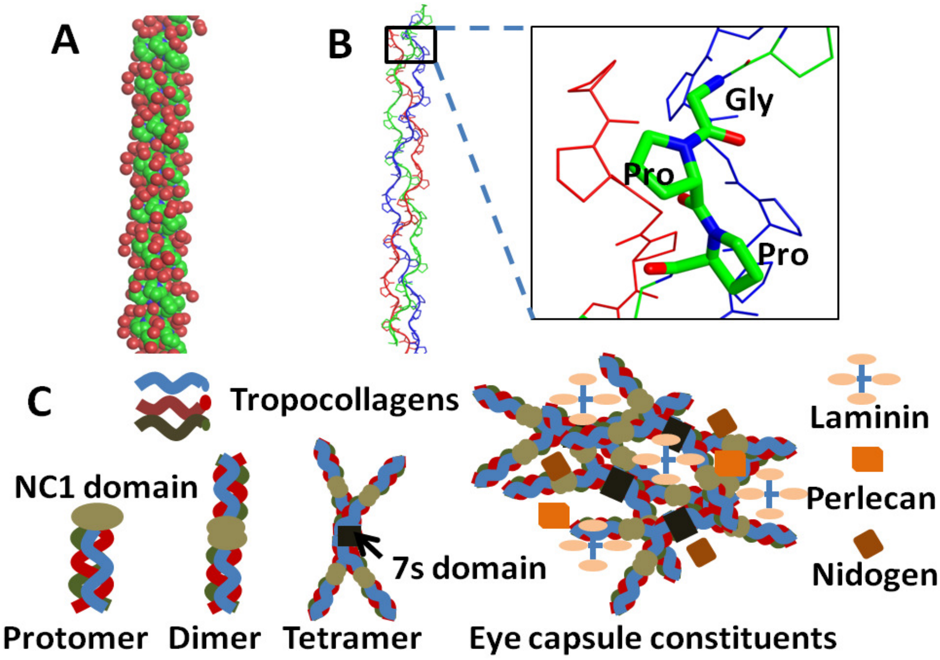

Figure 6.1: Structure of an ideal triple helix containing Gly-Pro-Pro sequences adapted from PDB ID: 1 K6F. (A) Representation of the triple helix with atoms show as spheres. (B) Line representation of triple helix. Inset shows the arrangement of Gly-Pro-Pro sequences as one of the three chains. (C) Structural components of eye capsule. The components are tropocollagens which are the basic unit of collagen IV and form protomer, dimer and network along with laminin, perlecan and nidogen.

capsule which is dominated by vibrational modes corresponding to amino acids like proline and hydroxyproline which are the major components of the collagen triple helix [93]. We have compared this with spectrum of pure collagen IV sample obtained commercially. Very good match suggest that the basement membrane is predominantly made up of collagen IV fibers. Other components (refer to figure 6.1) which constitute the eye capsule are the network protein laminin [84]. The collagen IV fibers are intercalated to the laminin network and held together by perlecan and nidogen [84]. Raman spectroscopy has been used in the past to study collagen fibers from different sources like tooth dentin [94], bone [95], rat and bovine tail [96] among others. Different phenomena like swelling [97], straining

[94], heating [83] and chemical treatment [98] of collagen fibers has been studied with the help of Raman spectroscopy. In this work, for the first time Raman spectroscopy was employed to study the intact Human anterior lens capsule in an ex-vivo environment. Collagen IV consists of triple helical fibrils called tropocollagen(Figure 6.1 A) which are characterized by Gly-X-Y sequences, where X and Y represent proline and hydroxyproline, respectively (Figure 6.1 B) [99]. There is a single hydrogen bond between the Gly N-H and the C=O group of the X residue of the tripeptide and the stabilizing interaction of water and the hydroxyproline groups provide stability to the tropocollagen moieties. Three of the tropocollagen molecules form a protomer (Figure 6.1 C). Two protomers connect through the NC or Non-collagenous terminal domains to form a dimer. Four of these dimers connect through the 7S glycosylated amino terminal and gets connected by disulfide bonds and lysine derived aldimide bonds [99]. In addition to this arrangement, the triple helices also align or attach laterally which could be confirmed though observation though electron microscope in formation of superhelices formed among two or three molecules [99]. Raman spectra correlate to these secondary structural elements through the amide I band analysis and unique signatures of the disulfide linkages constituting the 7S domain. Hence, these two spectral regions form very important regions susceptible to changes on chemical interactions.

We show the various effects of trypan blue on the integrity of the anterior lens capsule membrane (both mature and non-mature) through changes in the various Raman modes associated with amide I and disulfide bonds and have used them to understand the structure of the basement membrane. Trypan blue has also been reported as a cross-linking agent for collagen in eye capsule. We show the effects of cross-linking and its molecular basis by comparison with spectrum from a known cross-linking agent, glutaraldehyde, stained anterior lens capsule. From the concentration and time dependent staining studies, an optimum condition (<10 s) was found out for staining without significant alteration of the structure of the capsular components. Through Raman spectroscopy we have demonstrated that these changes can be observed much before and at much lower concentration that is observed by other macroscopic techniques.

6.2 Instrumentation and sample preparation

6.2.1 Lens capsule isolation

Anterior lens capsules of human eyes were removed surgically from patients undergoing phacoemulsification. 4 stained capsules, 12 unstained capsules and 4 stained capsules from hypermature cataracts were obtained from patients of varied age groups. The samples were stored in balanced salt solution (BSS, INTASOL-500, INTAS Pharmaceuticals Ltd, India) and the Raman experiments were performed within a period of 24 hours. For external staining of the eye capsules, Trypan blue solution (0.06% w/v) from Auroblue (Aurolab, India) was used. This stock solution was diluted with de-ionized water to prepare different concentrations of the dye for staining of the eye capsules. The unstained capsule samples were used for external staining experiments and also as controls.

6.2.2 FT-Raman spectroscopy and signal processing

FT-Raman spectra were recorded by a Bruker RFS 27 FT-Raman spectrometer. A diode-pumped Nd:YAG laser at 1064 nm with an output of 250 mW was used as the excitation source and 128 scans were collected for each spectrum. Spectra were obtained from a range of 400-4000 cm^{-1} with a resolution of 2 cm^{-1}. The specimens were placed on aluminum platform and directly placed inside the sample chamber. All spectra were smoothed using 5 point FFT method and baseline corrections were done using the baselinewavelet 4.0.1 [100] package through the R code (ver 2.15.2). Curve fitting of the amide I bands were done using Gaussian function in the Origin 8.0 software as reported elsewhere. Multiple peak fitting was done to determine position, intensity, width and the area under the peaks.

6.3 Results and discussions

6.3.1 Raman analysis of human anterior lens capsule

The Raman spectrum of the human eye capsule consists of peaks predominantly from aromatic amino acids, the backbone vibrations and the amide bands. The human lens capsule is known to be predominantly consisting of collagen IV but has a composition of proteins mixed with polysaccharides. The amino acid and carbohydrate composition in cataractous Human anterior lens capsule was found to be 80% and 11% respectively. Similar to that of other basement membranes, Human eye capsules consists of glycine, proline, hydroxyproline, hydroxylysine and half-cystine. Additionally the commonly occurring amino acids like cystine, methionine and tryptophan are also present. Among the sugars, the capsule contains significant amounts of glucose and galactose and also small amounts of fucose, mannose, glucosamine, galactosamine and sialic acid [93]. Here we discuss important modes which appear in the Raman spectrum of Human anterior lens capsule (Fig-

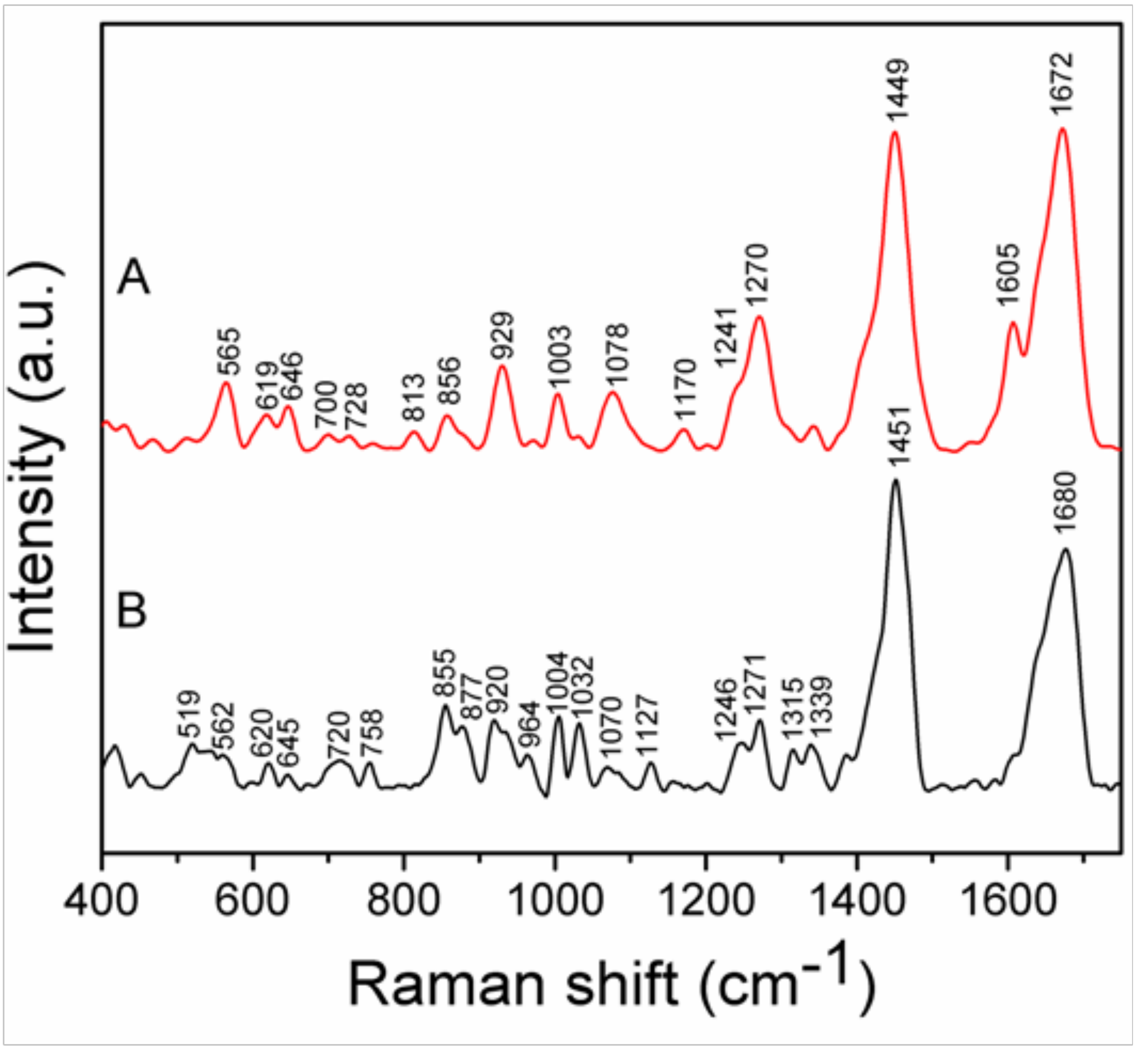

Figure 6.2: FT-Raman spectra of (A) Unstained human anterior lens capsule and (B) collagen IV (pure).

ure 6.2 A) and also discuss the modes of pure collagen IV as a reference (Figure. 6.2 B). The band assignments are given in Tables 6.1 and 6.2 .

6.3.1.1 The amide modes

Amide modes are the direct markers for the secondary structure of proteins. The amide I band lies in the region 1640-1690 cm^{-1} and the amide III lies in the

Table 6.1: Raman band assignment of human anterior lens capsule and collagen IV (pure) between 400- 1000 cm^{-1}1.

Human anterior lens capsule(cm^{-1})	Collagen IV (pure) (cm^{-1})	Glutaraldehyde stained anterior lens capsule	Band assignment and residues
		478, 495	C-O-C deformation
	519		ν(S-S)
565	562	567	ν(S-S)
619	620	616	Tyr, r,δ, ω (COO$^-$)
646	645	647	δ(COO$^-$)
700			C-S symmetric stretch, P$_C$-G
728	720	731	CH$_3$-S symmetric stretch, P$_C$-T
	758		CH$_2$ stretch, P$_C$-T
		801	C-O-C def.
813			(CCN) def./ (COC) str.
856	855	846	ν(CCC) proline ring/ C-H stretch (carbohydrates)
	877	871	Hydroxyproline/ C-H stretch (carbohydrates)
929	920	941	α-helical C-C stretch
	964	973	ν(C-C)

region 1230-1300 cm^{-1}. The major contribution to amide I is from C=O stretching vibrations with minor contributions from out-of-phase CN stretching vibration, the CCN deformation and the NH in-plane bend [20]. The position of amide I band is independent of the side chain configuration and is thus used as a secondary struc-

Table 6.2: Raman band assignment of human anterior lens capsule and collagen IV (pure) between 1000- 1800 cm^{-1}.

Human anterior lens capsule(cm^{-1})	Collagen IV (pure) (cm^{-1})	Glutaraldehyde stained anterior lens capsule	Band assignment and residues
1003	1004	1003	Phe ν_{12}
	1032	1037	Pheν_{18a}/C-N stretch
1078	1070		ν(C-N), carboxyl -OH bend
		1092	C-O-C asymmetric stretch
	1127		δ(NCH) proline
1170		1177, 1197	ω(CH$_2$), tNH$_2$, hydroxylysine, Tyr, Phe
1241	1246	1247	Amide III
1270	1271	1277	Amide III
	1315	1305	ν_r(CH$_3$, CH$_2$)
	1339	1385	ν_w(CH$_3$, CH$_2$)
1449	1451	1449	δ(CH$_2$), ν_{as}(COO$^-$), Lys, δ(N-H)
		1471	δ(CH$_2$)/δ(CH)
1605			Tyr and/or Phe (ν_{8a})
1672	1689	1663	Amide I

ture marker and is sensitive to secondary structural changes and transitions. The amide III vibrations arise from the in-phase combination of N-H bending and C-N stretching vibrations with minor contributions from in-plane CO bending and CC stretching vibrations [20]. The overlap of side chain vibrations in this region makes it less suitable for secondary structure analysis. Hence, we will focus our attention to amide I bands only.

Figure 6.3 shows the amide I region for the various samples used in this experiment. In case of unstained eye capsule the amide I is centered at around 1672 cm^{-1} and is characteristic of collagen like fibers seen in types I, II, III [96] and IV [101]. The typical triple helix structure contains polyproline II [102] type helices which have no intra-molecular hydrogen bonding because of the larger distances between the C=O and the N-H groups in a helical turn. Three of these helices come together to form a triple helix which are held together by a single hydrogen bond between the Gly N-H and the C=O group of the tripeptide. The triple helical

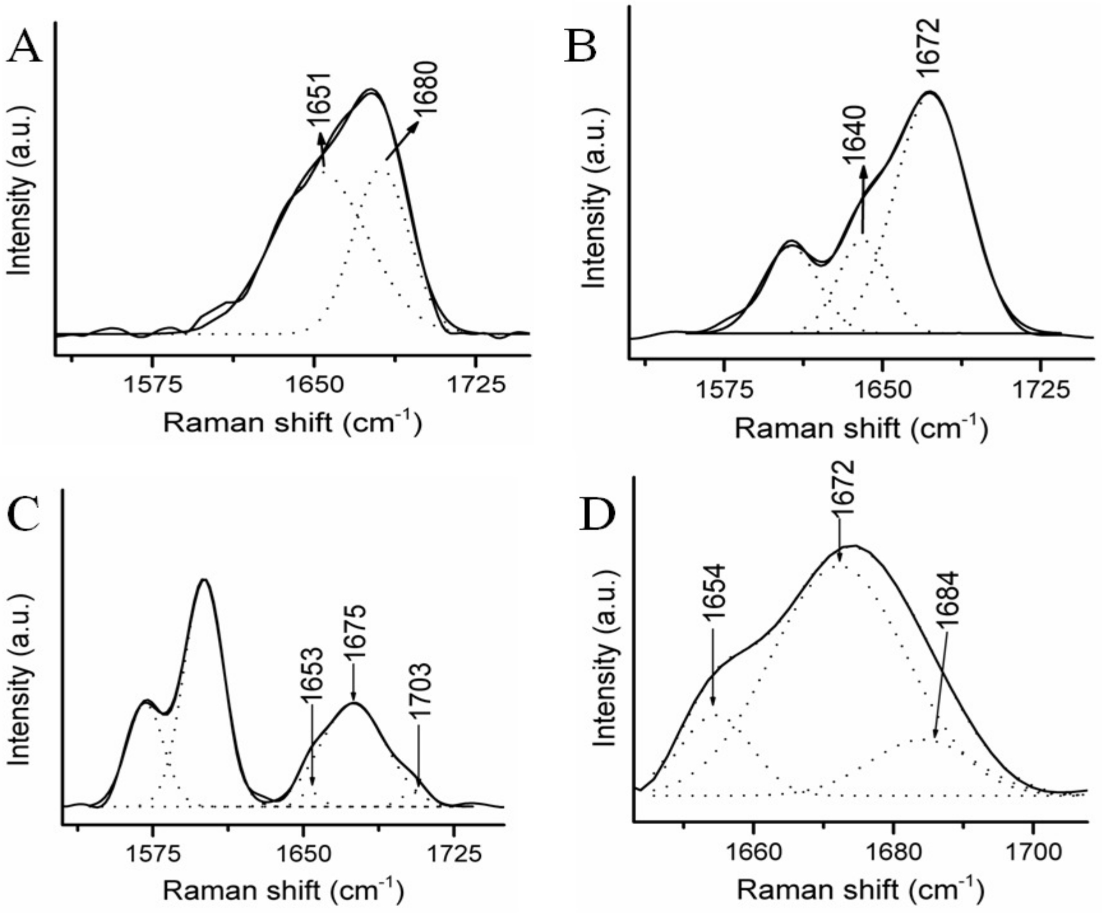

Figure 6.3: Peak fitting of amide I region of (A) collagen IV (pure), (B) unstained, (C) in-vivo stained and (D) ex-vivo stained human anterior lens capsule. The amide I components are assigned their values. The non-assigned modes belong to the trypan blue dye.

moiety of the collagen IV gives rise to the higher component amide I band at 1672 cm^{-1} and thus can also be attributed as the non-polar region of the secondary structure. The other polar groups constituting the collagen IV capsules like lysine, glutamic acid and aspartic acid forms more tightly bound helices whose amide I component occurs at a lower wavenumber of 1640 cm^{-1} (Figure 6.3A). This double-component amide I band is also reflected in the amide III band which consists of two components at 1241 and 1271 cm^{-1} (see Figure 6.2). The amide III region has distinct modes corresponding to different secondary structural components, unlike amide I where the secondary components lie in the same region and thus have to be de-convoluted [103]. The higher is the amide I band the lower is its amide III component. Therefore the 1241 cm^{-1} corresponds to the non-polar region and the 1271 cm^{-1} mode corresponds to the polar region and thus indicate the presence of two different secondary structural components. Similar observation of the double components of the amide III band of collagen arising from polar and non-polar regions has been reported earlier [104]. It should be noted that the amide I region can also contain components of the glycoproteins like laminin and entactin but does not have any contribution from other carbohydrates present. The presence of a single band with center around 1672 cm^{-1} suggests that the Raman spectrum is dominated mainly with collagen IV moiety which is the most abundant of all the components in the lens capsule. The two component amide I and III modes was verified from the spectrum of pure collagen IV. In the pure collagen IV, the amide I modes (Figure 6.3B) occur at 1651 and 1680 cm^{-1} respectively corresponding to the polar and non-polar regions respectively. The corresponding amide III modes occur at 1246 and 1271 cm^{-1} respectively. The positions of amide modes in pure collagen IV are upshifted by $5-8$ cm^{-1} due to the lack of hydrating water molecules in the lyophilized protein, which loosens up the membrane (reduction in hydrogen bonding). The similar positions of amide modes in the eye capsule and pure collagen IV indicate that similar secondary structural components are present in both the cases.

6.3.1.2 Side chain vibrations and major non-amide bands

The most prominent side chain vibrations arise from amino acid residues like proline, hydroxyproline and phenylalanine. Peak at 1003 cm^{-1} correspond to phenylalanine, 929 and 856 cm^{-1} correspond to proline and 882 cm^{-1} from hydroxyproline (see Figure 6.2) [104]. The carboxyl modes of -OH bending from residues like Asp and Glu can be found at 1078 cm^{-1} [105]. The peak at 813 cm^{-1} corresponds to C-O-C stretching mode arising from the cross linking among the tropocollagens [101; 105]. Bands at 619 and 646 cm^{-1} are assigned to the carboxyl group of proline and hydroxyproline [106]. The signatures for the disulfide bridges which occur around 550-600 cm^{-1} could be seen at 565 cm^{-1}. These disulfide bridges are present in the 7S domain. In the 7S domain C-S stretching vibrations are found at 700 and 728 cm^{-1} [101]. The 700 and 728 cm^{-1} modes can be assigned to P_c-G and P_c-T respectively [107]. P_c refers to the conformation in which the carbon atoms are at trans position to the sulfur atom in -CH_2-CH_2-S group [41]. The notations G and T stands for gauche and trans conformation about -CH_2-S- bond [41]. Pure collagen IV also showed all these modes suggesting that the eye capsules are predominantly made up of collagen IV. Interestingly the 7S domain of pure collagen IV contains the 562 cm^{-1} mode similar to the eye capsule and another band at 519 cm^{-1} indicates a different configuration. Also the C-S stretching mode appears as a broad peak at 720 cm^{-1} (P_c-G) and a peak at 758 cm^{-1}(P_c-T) [107].

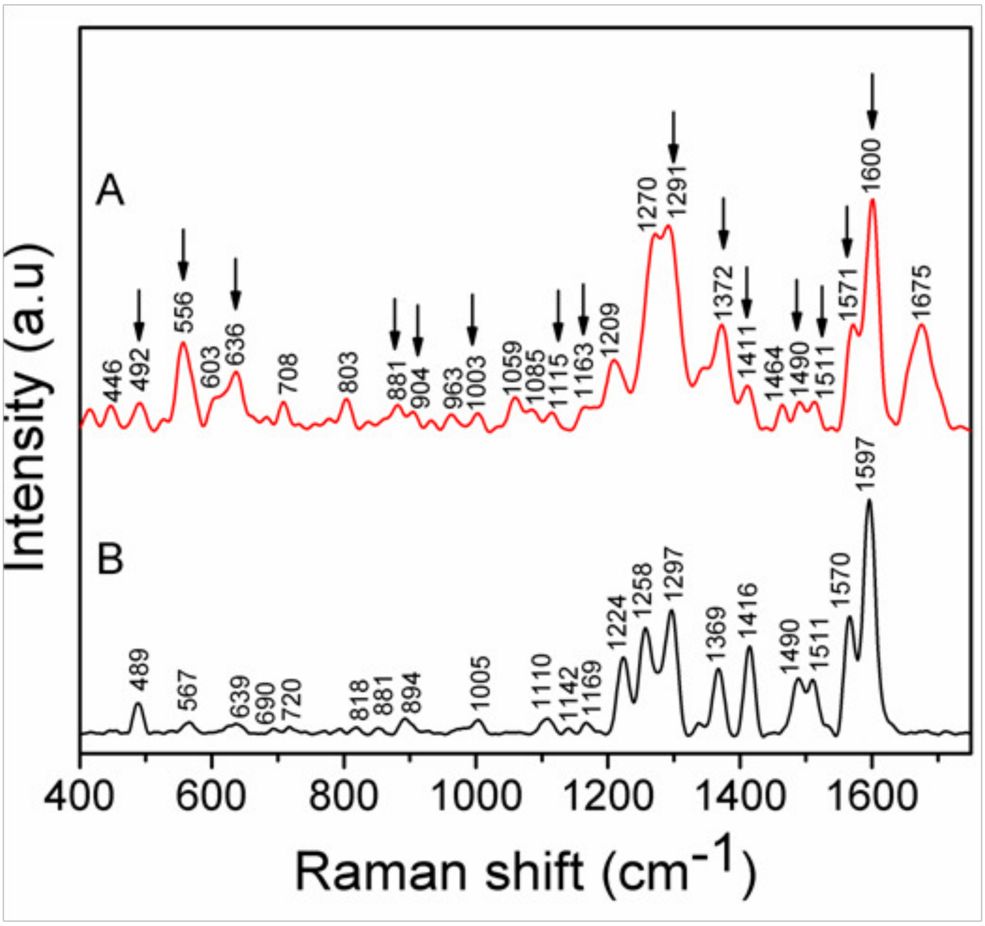

Figure 6.4: FT-Raman spectra of (A) trypan blue stained (in-vivo) anterior lens capsule and (B) trypan blue. The arrows indicate the bands in trypan blue stained anterior lens capsule which overlap with trypan blue modes.

6.3.2 Structural changes in anterior lens capsule on trypan blue staining

The trypan blue stained anterior eye capsules extracted from the normal cataract lens (Figure 6.4 A) showed peaks from the trypan blue. Figure 6.4 B shows the Raman spectrum of trypan blue. Prominent peaks at 1570 and 1600 cm^{-1} are from trypan blue. The region from 1200- 1300 cm^{-1} has many dye peaks overlapping with the lens capsule peak. Hence it is difficult to use the amide III region for any structural analysis. There is an overlap in the region of disulfide bonds at around 550 cm^{-1}. Fortunately, the amide I region, the 7S region and the C-O-C stretch region has no significant overlaps with the trypan blue bands and are significant for analysis of structure. In addition, we have analyzed these modes in the Raman of anterior lens capsule of cataractous lens as well as in hypermature lens capsules (Figure 6.5). We have used the Raman spectra of of the eye capsule treated with glutaraldehyde (Figure 6.6) as a control for studying cross-linking effects since glutaraldehyde is known to be a cross-linking agent and increases the stiffness of the tissue [92].

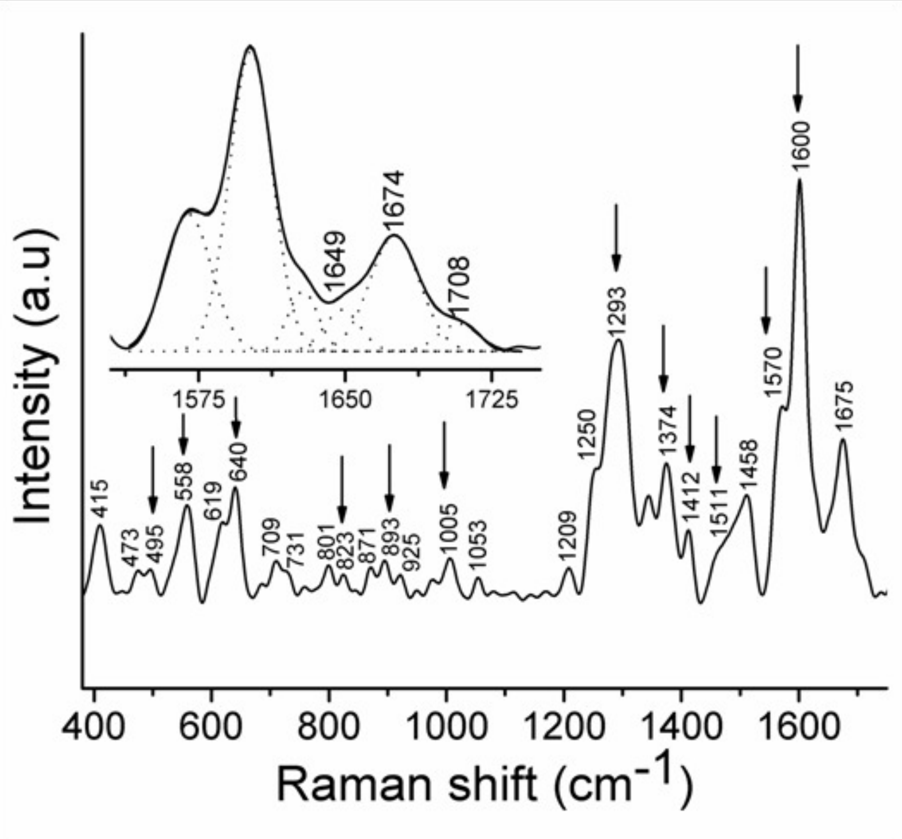

Figure 6.5: FT-Raman spectrum of trypan blue stained (in-vivo) mature anterior lens capsule . The deconvoluted amide I region is shown in inset. The arrows indicate the bands which overlap with the modes of trypan blue dye.

6.3.2.1 Changes in the amide modes

In case of the in-vivo stained eye capsule, the fitted amide I peak are found to be around 1653, 1675 and 1703 cm^{-1} (Figure 6.3C). This implies that the ordered triple helix undergoes a transition to loosely packed structure upon the addition of the trypan blue dye. It is also observed that the polar region is affected more than the non-polar region. The reactive oxygen species formed from the reaction of the dye molecules with the substrate induces the cross linking of the collagen fibers as well as disruption of the hydrogen bonds. We observe a shift in the triple helix peak, namely, 1640 and 1672 cm^{-1} shift to 1653 and 1675 cm^{-1} respectively. In addition we observe the presence of 1703 cm^{-1} peak. The increase in the amide I frequency can be understood arising due to the decrease in the hydrogen bond upon addition of trypan blue. The 1703 cm^{-1} peak is due to the disruption of hydrogen bonding during the formation of ether type of bond due to the cross-linking effect of trypan blue or increase in random coil. Similar observation is made in the case of glutaraldehyde treated collagen IV case as is shown in Figure 6.6. The amide I modes of the capsule obtained from hypermatured cataract also shows similar behavior. We observe amide I bands at 1648 and 1675 cm^{-1}. A peak at 1707 cm^{-1} is also seen suggesting strong cross linking in the hypermature cataract. Since there is a corresponding amide III peak associated with the amide I peak, it is expected that a new peak at lower wave number should come up corresponding to the non-helix secondary structure formed in the case of trypan blue stained samples. In case of trypan blue stained capsules (both normal and mature), there is indeed an appearance of a new band around 1209 cm^{-1} which is lower in frequency than the other two amide III bands at around 1240 and 1270 cm^{-1} and corresponds to the random coil region as suggested earlier. In the glutaraldehyde case (see Figure 6.6), we are not able to see 1209cm^{-1}. It could be that in the case of glutaraldehyde treated samples the reduction in hydrogen bonding destabilizing α-helix is compensated by crosslinking induced by glutaraldehyde [108]. In comparison in the case of trypan blue the reduction in hydrogen bond leads to the origin of random coils.

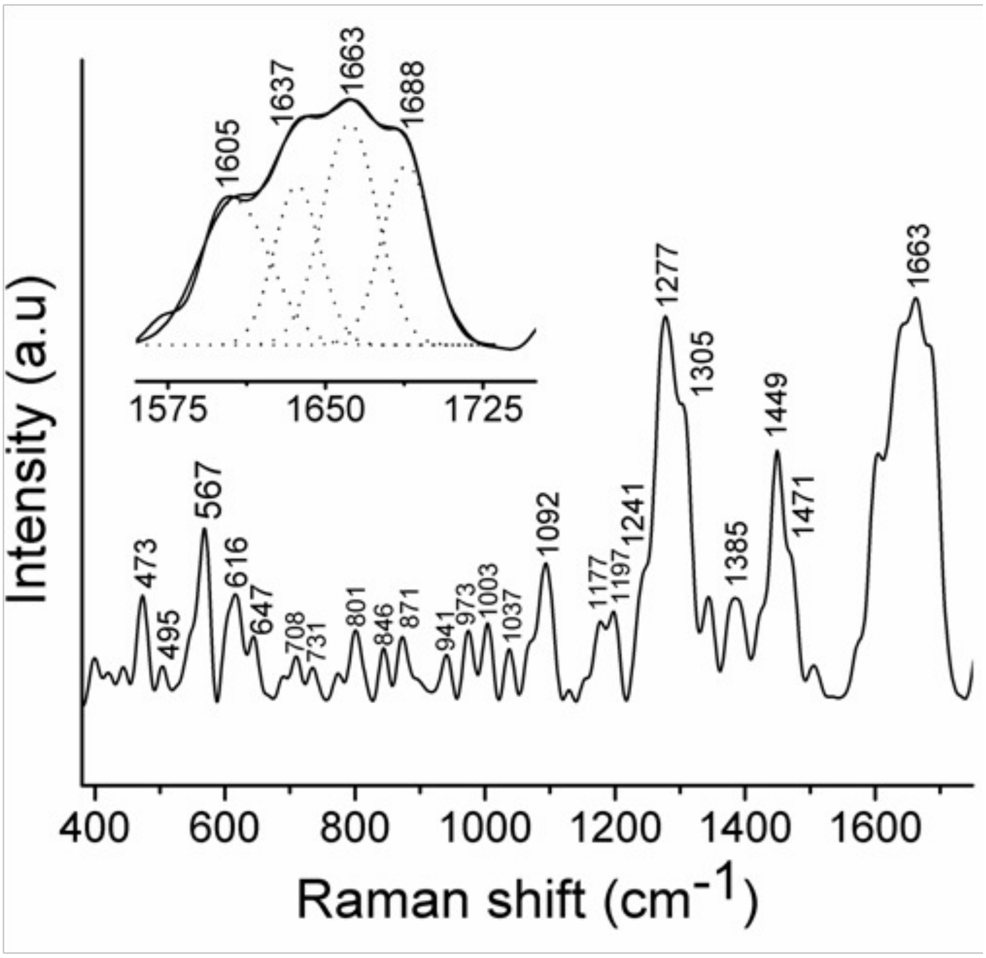

Figure 6.6: FT-Raman spectrum of glutaraldehyde treated anterior lens capsule. The deconvoluted amide I region is shown in the inset.

6.3.2.2 Changes in the side chain vibrations and non-amide modes

The major changes which happened due to dye staining were the changes in the peaks corresponding to C-O-C bending mode and the modes corresponding to the disulfide bridges in the 7S domain. A mode at 815 cm^{-1} is seen in collagens and is assigned to the C-O-C stretching, associated with the glucosyl-galactosyl-hydroxylysinonorleucine cross links between topocollagens [101]. We observe this mode at 813 cm^{-1} in unstained capsule sample. Upon staining with trypan blue this mode shifts to 803 cm^{-1}. Similarly in the case of glutaraldehyde we observe this mode shifting to 801 cm^{-1}. This is a clear evidence for increased crosslinking in the tropocollagen. In addition to this in the case of glutaraldehyde treated sample we observe a new mode at 490 cm^{-1} which is associated with C-O-C deformation [108]. In the trypan blue stained sample we observe a new mode around 472 cm^{-1}. This suggests that trypan blue induces ether type bonds for cross linking. It is interesting to see that another mode around 1085 cm^{-1} in the case of trypan blue and 1094 cm^{-1} in the case of glutaraldehyde appears in the Raman spectra (Figures 6.4-6.6). It is seen that a mode around 1094 cm^{-1} and assigned to C-O-C asymmetric stretching vibration is observed when ether type of bond exists upon cross linking induced by glutaraldehyde in collagen. In case of trypan blue this bond formation can be facilitated by the free radical singlet oxygen generated due to the photosensitizer action of trypan blue which easily reacts with electron rich groups contained in residues like cysteine, methionine, tryptophan, tyrosine and histidine [92]. The bands corresponding to the 7S domain, mainly the C-S stretching mode at 728 cm^{-1} shifts to a lower frequency to 708 cm^{-1} in both trypan blue stained capsules (normal and mature) as well as GA crosslinked capsules. The C-S stretching mode is highly dependent on the configuration of the thiol and the disulfide bonds. This suggests that during the cross-linking or shrinking of the capsule the 7S domain is affected. The electron rich thiol groups can readily react with the singlet oxygen generated by trypan blue. If the number of sulphydryl groups is more, it forms mixed disulfides or sulfonic acids [109]. Therefore trypan blue staining can lead to more disulfide cross-linkings which is also evident from the shift and appearance of C-S stretching mode in the 7S region. The 1449 cm^{-1} peak is associated with CH_2 and CH_3 bending modes. Since in proteins undergoing secondary changes, this mode should be invariant, hence the intensity of 1449 cm^{-1} is used as a normalizing peak for intensity comparison. Surprisingly in both trypan blue stained and glutaraldehyde stained capsule we find the intensity of 1449 cm^{-1} decrease. In earlier glutaraldehyde studies too Jastrzebska et al. [108] observed this behavior. It is known that δ(N-H)[110] and carboxyl group variation [111] from acidic amino acid groups also contribute to this peak. It is suggested that enhanced cross linking between collagen fibers lead to decrease in the 1449 cm^{-1} mode [112]. Thus the decrease in 1449 cm^{-1} intensity in the trypan blue stained capsule suggest enhanced crosslinking in collagen fibers. From the above results it is clear that trypan blue staining of the lens capsule leads to increased crosslinking and reduction in the hydrogen bonding. This suggests that this lens capsule material would stiffen leading to reduced elasticity.

6.3.3 Implications of structural variation on biomechanical characteristics

The effects of trypan blue staining on the mechanical characteristics on anterior lens capsule have been investigated by Dick et. al [89]. Staining led to the decrease in elasticity of the membrane measured with a modified rheometer but increase in the stiffness. Similar results were reported by Jardeleza et. al. [86] by using a nano-indentation technique. Wollensak et. al. [92] reported that in porcine model, the increase in stiffness to about 25% happened when light was irradiated on the capsule [92]. In contrast to these results of increase in stiffness and loss of elasticity, Jaber et. al. [91] reported that on trypan blue staining there was no significant change in the tear resistance during capsulorhexis. We have used Raman spectroscopy to understand the effect of concentration of trypan blue and the length of exposure of trypan blue on the human anterior lens capsule. Raman studies were motivated due to the observation that the changes in biomechanical properties of the lens capsule can be related to photosensitization and cross linking by oxygen free radicals. It has also been reported that cross linking in tissues like collagen fibers in avian dystrophic muscles [113] and Human articular cartilage results in the change in stiffness of these tissues [114]. Spectroscopic characterization along with mechanical methods therefore can give a more accurate and extensive insights on the behavior of tissues subject to mechanical stress as reported earlier in case of collagen fibers [115]. Since both cross-linking as well as hydrogen bond disruption happens in case of trypan blue staining we have calculated the fraction of ordered structural region from the total area of ordered and random coil regions. Ordered structure fraction= $\frac{AT-AR}{AT}$, where AT is the total area of amide I peak and AR is the area under the peak corresponding to the disordered region around 1700 cm^{-1}. Structural characteristics can be directly correlated to the degree of structural orderliness in proteins. The length of flexible domains and extent of cross linking between the monomeric domains determine the flexibility of the elastomeric proteins. Figure 6.7 A shows the concentration dependence of the ordered structure fraction on concentration of trypan blue and figure 6.7 B shows the variation of ordered structure fraction with time for two different concentrations. For time dependence studies two concentrations of 0.06% (stock) and 0.012% (minimum concentration to visualize the capsule [116]) were used and for concentration dependent studies the time of staining was 2 minutes. It has been reported by mechanical studies that the effect of photosensitization and cross linking by the oxygen free radicals and hence the biomechanical changes occur only after 1 minute at a concentration of 0.1% [92]. But Raman studies indicate that even in case of a lower concentration of 0.06%, the structural transition (change in amide I band) starts much earlier at 10s of staining time. Our study points out that till a concentration of 0.0012% and staining of 2 minutes, there were no sign of formation of disordered regions and hence structural alteration was avoided. However this concentration is too dilute for visualization of the capsule. But when a concentration of 0.012% (minimum concentration for visualization) was used to stain the capsules for a time of less than 10s, the structural alterations were not seen. Therefore it can be used as a safe limit (staining with 0.012% dye for 10s) to ensure that no structural alterations of the membrane take place. This can ensure that the mechanical characteristics of the capsule like stiffness does not change thus ruling out possibilities of capsular tears and other complications during surgery. Thus we see that not only concentration, but time of staining is also important for the structural transitions. This also shows that Raman spectroscopy can be used to monitor structural changes more precisely at much lower concentrations and time scales as compared to other macroscopic techniques.

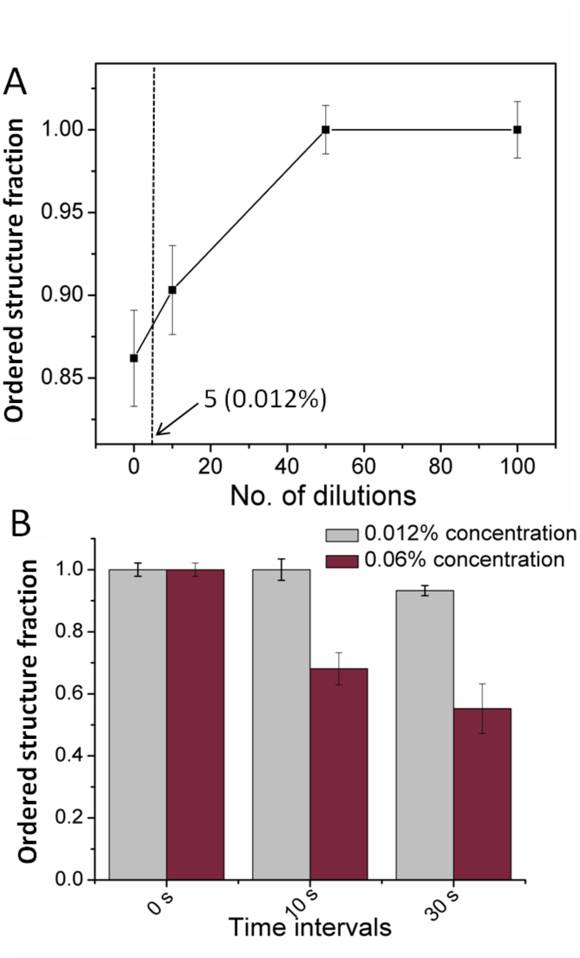

Figure 6.7: The ordered structure fraction at different dilutions of trypan blue used for staining of human anterior lens capsule. The helix fraction was calculated by peak fitting of the amide I band of the Raman spectrum and adding the contribution from the helices. The stock (0 dilution) concentration corresponds to 0.06% trypan blue. The dotted line shows 0.012% or 5 times dilution which is the lowest concentration required fro visible staining of the capsules. (B) The ordered structure fraction at different time intervals of trypan blue stained human anterior lens capsule. The concentrations used were 0.012% and 0.06% trypan blue.

6.4 Conclusions

In this work FT-Raman and Raman microspectroscopic studies were conducted on Human anterior lens capsule which were extracted by capsulorhexis during cataract surgery. The amide I analysis shows a two component system with the higher wavenumber component at 1672 cm^{-1} corresponding to the non-polar proline-rich triple helical region and the lower component at 1640 cm^{-1} corresponding to polar region containing polar amino acids of the collagen IV present in the membrane. The amide III also consists of two bands at around 1240 and 1270 cm^{-1} corresponding to the non-polar and polar region respectively. On staining with trypan blue, an extra amide I band appears at around 1700 cm^{-1} indicating disordered structure or randomly coiled secondary structure. The higher amide I mode has its counterpart in amide III region at around 1209 cm^{-1}. Amide I band at 1640 cm^{-1} shift to a higher wavenumber to about 1653 cm^{-1} indicating hydrogen bond disruptions in the polar region. The cross-linking action of trypan blue is also evident from the appearance of C-O-C bond vibrational modes comparable to that of glutaraldehyde cross-linked samples. Trypan blue staining also affects the 7S region which is responsible for the network forming nature of collagen IV. Concentration and time dependent studies show that onset of structural changes occurs after 50 fold dilution of the stock concentration of dye (0.06%) for a time of 2 min. If the concentration of dye is reduced 5 folds (minimum concentration needed for visualization of capsule), the onset of structural changes start occurring only after 10 seconds. Thus Raman spectroscopy was used to precisely find out the time and concentration of dye responsible for the structural alterations as well as the molecular mechanisms governing the changes in mechanical properties.

CHAPTER 7

EFFECT OF TREHALOSE ON PROTEIN-NANOPARTICLE INTERACTION

7.1 Introduction

Nanoparticles have generated a lot of interest in the field of therapeutics and biodiagnostics. The unique surface and optical properties of the nanoparticles which make them distinct from their bulk counterparts can be harnessed for targeted drug delivery [117] and therapeutics [118] and also for ultrasensitive biodetection [119] and other diagnostic applications [120]. Although, lot of developments are taking place to attach different biomolecules including nucleic acids, sugars and proteins to different nanoparticle systems, the complicated behavior of these molecules on interaction with the nanoparticles are still not completely understood. Proteins are made up of specific sequences of amino acids which fold up to form a unique three-dimensional structure. They are responsible for essential body functions and are used for several therapeutic applications. These include proteins like insulin, erythropoietin, interferons to name a few and can be target delivered to specific sites of the body by using suitable methods. Nanoparticle-protein conjugates have been used to target cytoplasmic or nuclear regions of cells to alter the cellular machinery of the cell [121]. Proteins like GFP have been used for imaging applications [122]. Other than therapeutic uses, nanoparticles have been widely used as highly sensitive probes for elucidating structural aspects of different biological systems. Some of the techniques used are surface plasmon resonance [123], surface enhanced Raman spectroscopy [124] among others. The fundamental aspects of use of each of these analytical techniques as well as therapeutic applications is based upon the understanding of the manner in which the proteins interact or attach with the nanoparticle surface. It has been known that proteins interact with nanoparticles surface and undergoes conformational change. This has an adverse effect on the functions of the proteins [125; 126]. Many studies related to circular dichroism [127] and molecular dynamics simulations [24] have shown local conformational changes of the protein on site of attachment to the nanoparticle surface. Therefore, strategies are needed to be adopted to prevent the denaturation or conformational changes of the proteins in the presence of nanoparticles.

Sugars have been found to provide excellent stability to proteins when subjected to chemical and thermal stress or dehydrated conditions [128]. Trehalose is a non-reducing disaccharide which provides exceptional stability to the proteins from heat or cold stresses. It is used in freeze drying of proteins to conserve their structures [129]. It is also chemically inert since it is a non-reducing sugar. There are different mechanisms proposed for the stabilizing effect of trehalose on proteins. These mechanisms are different in dry and solution states. In the dry state, the protein is stabilized by hydrogen bond formation between the sugar and protein which prevents it from dehydration induced structural changes [130]. Another theory known as vitrification theory, exists in which the sugars form glassy matrix around the proteins preventing their destabilization [131]. But in the solution phase sugars and polyols stabilize the folded structure of proteins due to greater preferential hydration of the unfolded state than the folded state [132; 133]. Trehalose affects the surface tension of the medium and hence leads to preferential hydration of the protein molecules [134]. In addition to surface tension effects, the interaction of sugars with the protein side chains also increases the stability of the protein, providing the fine balance between favorable and unfavorable interaction of the proteins with the solvent molecules in their native and denatured state [129]. The solution stability of the protein molecules can also be correlated to the structural stability [135]. Thermal, chemical, dehydrating stresses and the effects of sugars on the structure in the case of proteins have been investigated, but there has been no direct study of the stress posed by nanoparticles on the protein structure and the role of sugars in it. We have investigated the model case of interaction of lysozyme with silver nanoparticles and the role of trehalose in stabilization of the protein-nanoparticle system.

The structure and property of lysozyme have been widely studied and have been used as a model in many experiments related to protein structure and stability [136]. Lysozyme has been used in food industry and pharmaceuticals [137]. It is as antibacterial agent as it has a lytic action on the cell wall of gram positive bacteria [138]. Lysozyme has been used to study both the dried and the solution phase stabilizing effects of various polyols and sugars, including trehalose. Some of the techniques used to study these effects are circular dichroism [127], differential scanning calorimetry [135] and quasi-elastic light scattering [135] among others.

Lysozyme has been known to form aggregates in presence of citrate capped gold nanoparticles [139]. This nanoparticle induced misfolding of proteins further catalyzes the aggregate formation, which in turn leads to the formation of protein-nanoparticle aggregates. Lysozyme is a 14.7 kDa protein and has 129 amino acids and is a stabilizing agent. Here in this work, we investigate the role of trehalose on the interaction of lysozyme with the silver nanoparticles through a highly surface sensitive technique known as surface enhanced Raman spectroscopy (SERS). In this technique the Raman cross sections of the analyte molecules are enhanced greatly due to the intense electric field generated by the surface plasmons excited by the incoming laser light [140]. Since the electric field intensity in the vicinity of the plasmonic nanoparticles is distance dependent, only the bond vibrations present near to the surface of the nanoparticles gets enhanced thus giving surface-specific information [141]. We show the utility of the trehalose environment in getting information from intact protein structures, which otherwise undergo structural denaturation on interaction with nanoparticles. This can have implications in the area of SERS where the direct use of proteins can be limited due to issues of nanoparticle induced denaturation. Although this can be prevented by using capping agents like poly-ethylene glycol, [139] it lowers the enhancement factor by increasing distance from the nanoparticle surface. Thus, providing the protein with a stabilizer, rather than capping the nanoparticle seems to be more appealing. We have complemented the SERS with secondary structure analysis by circular dichroism and the binding of protein to nanoparticles using fluorescence quenching and UV-absorbance techniques, to provide credible support to our observations.

7.2 Materials and methods

Preparation and characterization of silver nanoparticles: Colloidal silver nanoparticles were synthesized by the following the standard Lee-Meisel method using sodium citrate as a reducing as well as capping agent. The nanoparticles were characterized by transmission electron microscope and UV-visible spectroscopy. The concentration of silver nanoparticles was calculated by beer-lambert law using epsilon values reported in the literature [142].

Zeta potential studies: The zeta potential studies were carried by using Zetasizer Nano ZS (Malvern Instruments). The temperature for all the measurement was kept at 25 °C. The concentration of protein was varied by keeping the concentration of the nanoparticles constant (0.5 nM).

Circular dichroism: The effect of nanoparticles on lysozyme structure in liquid solutions was studied by circular dichroism (CD). The concentration of protein was maintained at around 10 μM in 10 mM potassium phosphate buffer (pH 7.4) using JASCO spectrometer. A quartz cuvette of 1 mm pathlength was used to acquire CD spectrum. Each dataset was an average of three scans between the range of 200 nm to 290 nm. The buffer spectrum was subtracted to obtain the final spectrum (molar residual ellipticity vs wavelength) for analysis of secondary structure. Concentration of nanoparticles was fixed at 0.5 nM. The concentrations of trehalose in the solution used were 0.5 M, 0.05 M and 0.005 M.

Fluorescence quenching studies: Fluorescence quenching of the tryptophan residues on interaction with silver nanoparticles in various concentrations of trehalose (0, 0.5 M and 0.05 M) were studied by excitation at 290 nm and emission at the range of 300-400 nm. The concentration of protein was maintained at 1 μM in 10 mM potassium phosphate buffer. The concentrations of silver nanoparticles solution used were 0.005, 0.167, 0.0167, 0.083, 0.33 and 0.5 nM. The data was fitted using the stern-volmer equation to obtain the binding constant and number of binding sites at different concentrations of trehalose.

UV-absorbance studies: The UV-vis absorbance studies on nanoparticle aggregation were performed in the presence of different concentrations of trehalose (0 M, 0.05 M and 0.5 M) as a function of time. The molar ratio of protein and silver nanoparticle was fixed at 1: 100. The absorbance was measured for the solution at the interval of every 5 minutes. UV-vis study was conducted similarly for sucrose.

SERS studies: SERS samples were prepared by preparing protein-nanoparticle conjugates with different molar ratios of proteins and nanoparticles The spectra were collected in different trehalose concentrations (0, 0.5 and 0.05 M respectively) in solution mode by using water immersion 60x infinity-corrected objective (Nikon Plan Apo, Japan, NA 0.9). A 180° backscattering geometry was used for acquisition of the spectra from a custom made Raman setup and 632.8 nm He-Ne laser (model 30995, Research Electro Optics, Inc., U.S.A.) as a Raman excitation source. The spectrometer consists of a monochromator (Horiba Jobin Yvon, iHR 320) and a Peltier-cooled CCD (Andor iDus). A holographic 1800 grooves mm^{-1} grating was used along with the 200 μm spectrograph entrance slit setting. The typical accumulation time of the spectra were 30s and a 5 point FFT filter was used to smoothen the spectra.

7.3 Results and discussions

7.3.1 Circular dichroism study to determine preservation of protein structure on binding to nanoparticle surface

Circular dichroism is an easy and convenient method to determine the protein secondary structure as well their folding and binding characteristics in aqueous media. CD has been used previously to study protein-nanoparticle interactions and calculate the amount of protein denaturation in the presence of different kinds of nanoparticles [143]. It has been found that the structure of protein has a tendency to undergo structural change or reorganization on interaction with a surface. The

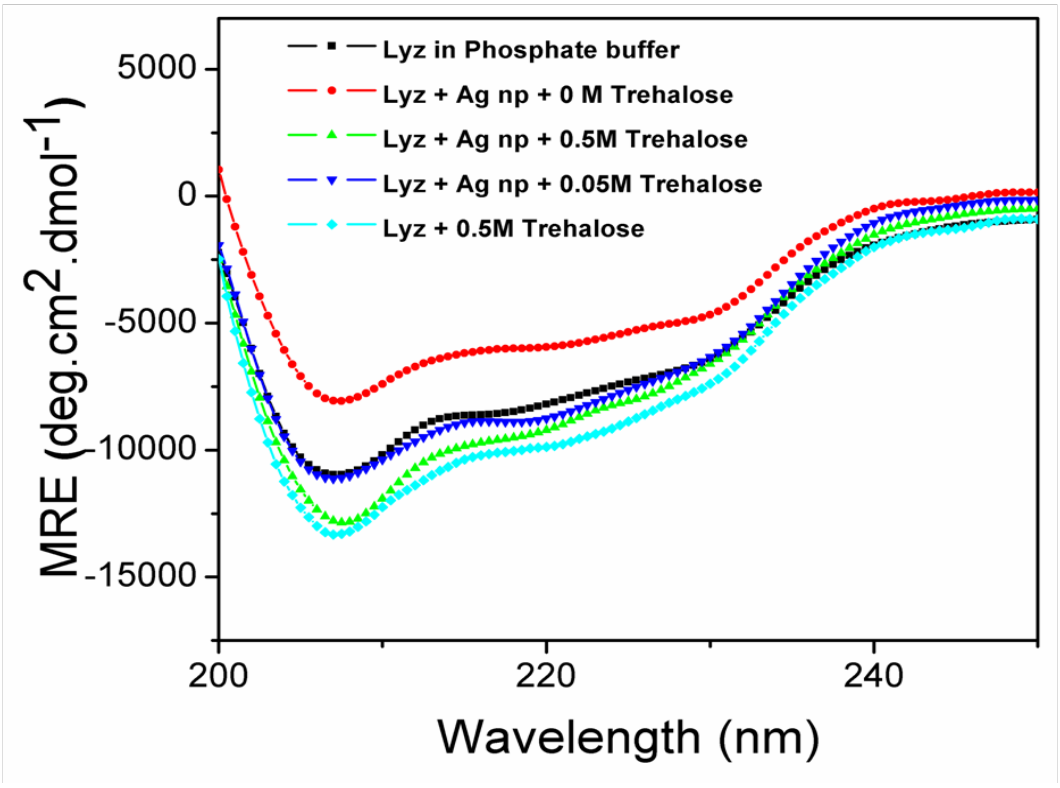

Figure 7.1: Circular dichroism data of Lysozyme (Lyz) in the presence of Ag nanoparticles and different concentrations of trehalose. The nanoparticle concentration was 0.5 M and those of trehalose are mentioned in the figure legend.

nature of surface plays a role in determining the extent and the nature of the change. The α-helix content of a protein, which is a measure of the structure, reduces on interaction with a hydrophilic surface whereas in some cases is increased on interaction with hydrophobic surfaces. Structural changes on adsorbtion to different surfaces have been a cause of concern as it has direct repercussions on the activity of the protein. Therefore, we use CD spectroscopy to analyze the nanoparticle induced stress on lysozyme structure and the effect of trehalose in solution phase. CD gives a measure of the secondary structural components of the protein like α-helix, β-sheet and random coil. The molar residual ellipticity (MRE) was calculated from the mdeg values of the raw data by the formula $\frac{\theta_d M}{10CLN_r}$, where θ_d is the ellipticity in mdeg, M is the molecular weight of lysozyme (14700 Da), C is the concentration of the protein in mg/ml, L is the path length of the cuvette and N$_r$ denotes the number of residues in the protein. The MRE values show a significant increase in negative values on increasing the concentration of trehalose in the solution (Figure 7.1). The helicity, which is proportional to the MRE values, is found to be the most in lysozyme solution in 0.5 M trehalose. When the concentration of silver nanoparticles is kept constant, and the concentration of trehalose was decreased, there was a decrease in the MRE values at 208 nm indicating the loss of α-helix structures. Therefore, we see that trehalose has a role to play in the structural preservation of protein from the stress caused by the interaction with the nanoparticle surface.

7.3.2 Fluorescence quenching by silver nanoparticles

Lysozyme consists of 6 tryptophan residues which are also near to its substrate binding site at the positions 28, 62, 63, 108, 111 and 123. These residues act as the most dominant fluorophores for the study of fluorescence quenching. The binding modes and the number of binding sites can be calculated by the following modified stern-volmer equation (* refer to end of this chapter):

$$\log \frac{F_0 - F}{F} = \log k_b + n \log Q \tag{7.1}$$

where F$_0$ and F are the fluorescence intensities in the absence and presence of the quencher respectively. Figure 7.2 shows the plots obtained from fluorescence quenching experiments. The plot of log k$_b$ vs log Q gives the value of binding constant k$_b$ and the number of binding sites, n. The values of k$_b$ and n are tabulated in Figure 7.2 D for three different concentrations of trehalose which are 0 M, 0.05

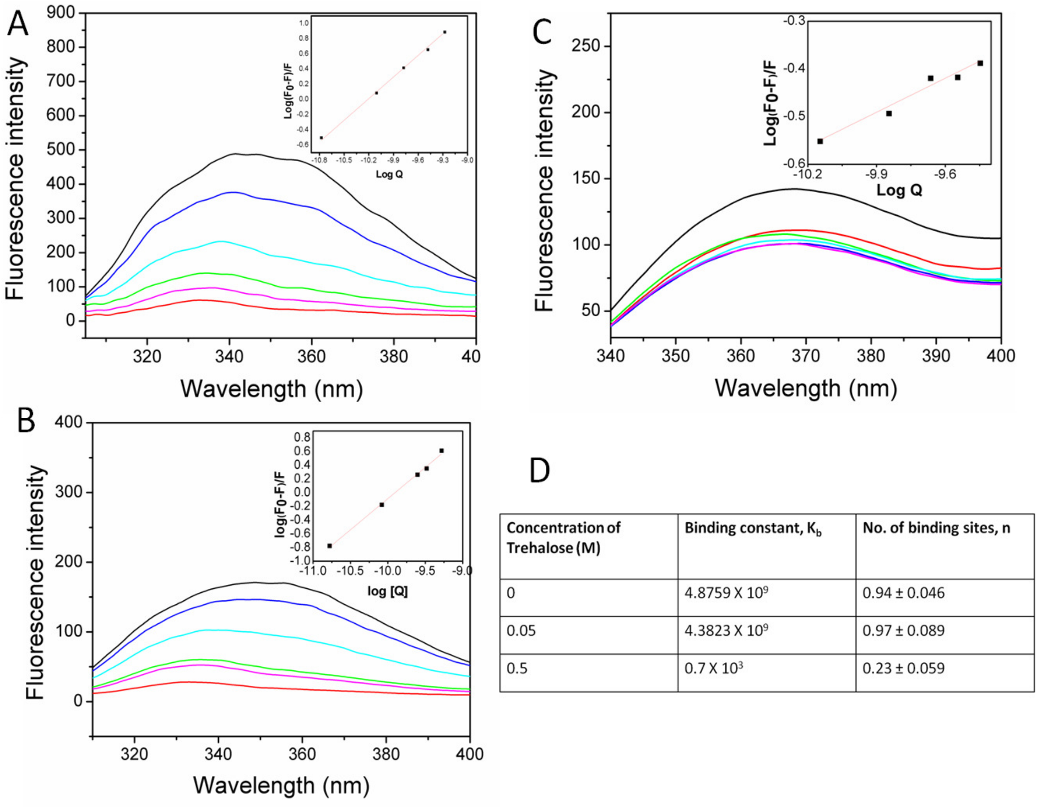

Concentration of Trehalose (M)	Binding constant, K_b	No. of binding sites, n
0	4.8759 X 10^9	0.94 ± 0.046
0.05	4.3823 X 10^9	0.97 ± 0.089
0.5	0.7 X 10^3	0.23 ± 0.059

Figure 7.2: (A), (B) and (C) shows tryptophan fluorescence quenching in the presence of different concentrations of Ag nanoparticles in 0, 0.05 and 0.5 M trehalose solution respectively. (D) shows the binding constants and no. of binding sites of lysozyme in different concentrations of trehalose.

M and 0.5 M respectively. Interestingly, the values of k_b are almost similar for the concentrations of 0 M and 0.05 M trehalose solutions, with a slight decrease in binding for 0.05 M trehalose solution. In case of 0.5 M trehalose solution, the binding constant is greatly reduced. This indicates that a concentration 0.5 M trehalose affects the binding of the protein to the silver nanoparticles to a great extent. The value of n is also much lesser for 0.5 M trehalose solution which leads to the conclusion that lysozyme at a trehalose concentration of 0.5 M trehalose solution cannot efficiently interact with the surface of the silver nanoparticles. The concentration of 0.05 M trehalose permits the interaction of lysozyme and silver nanoparticles as evident from the values of binding constants.

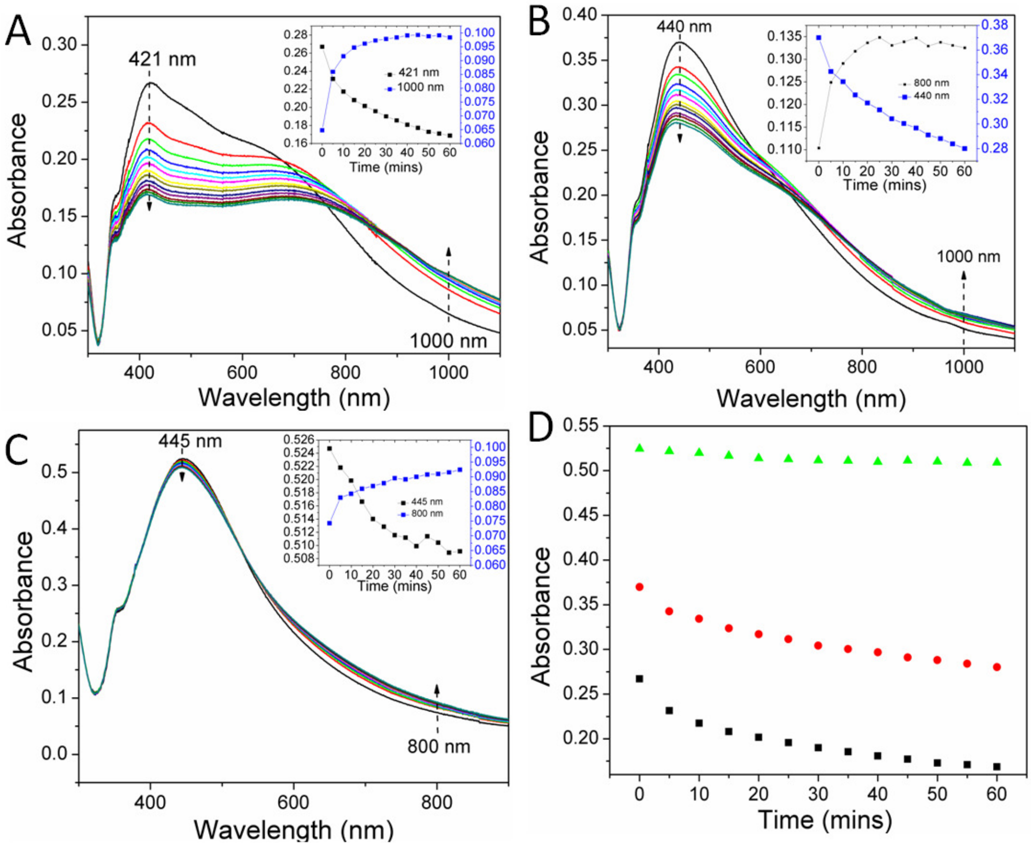

Figure 7.3: UV-vis spectra showing aggregation behavior of Ag nanoparticles in the presence of lysozyme and under different concentrations of trehalose. (A), (B) and (C) corresponds to trehalose concentrations of 0, 0.05 and 0.5 M respectively. (D) shows the reduction of the transverse plasmon mode with time in presence of 0 M (black), 0.05 M (red) and 0.5 M (green) trehalose.

7.3.3 UV-absorbance studies for protein aggregation in the presence of silver nanoparticles

The UV-vis spectra of silver nanoparticles in the presence of lysozyme shows the aggregation behavior of protein- nanoparticle conjugate as earlier reported by Zhang et al. [139] The transverse plasmonic mode, which occurs around 450 nm for

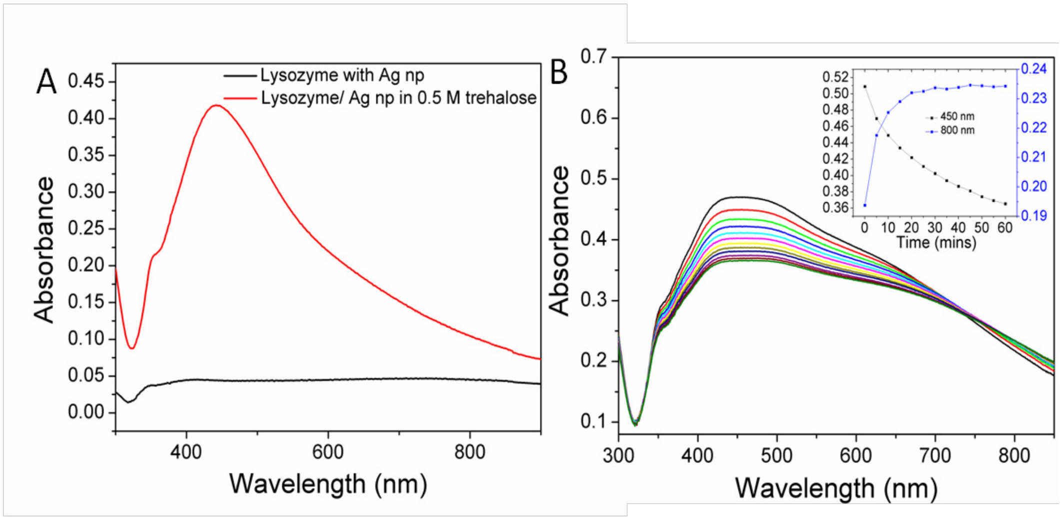

Figure 7.4: (A) UV-vis spectra of lysozyme-nanoparticle conjugate (black) and lysozyme-nanoparticle conjugate in presence of 0.5 M trehalose after 24 hrs. (B)UV-vis spectra of Ag nanoparticles in the presence of 1M sucrose with intervals of 5 mins between successive spectra. Inset shows the intensitiy variation of 450 nm and 800 nm peaks.

silver nanoparticles, decreased in intensity with time whereas the intensity of longitudinal mode increased (Figure 7.3). This point to the aggregation behavior of the protein-nanoparticle system where the interparticle distance between the nanoparticles decreases as the protein aggregation commences. More and more protein aggregates are formed with increasing time as the partially unfolded proteins on the surface of the nanoparticles act as seeds for the formation of protein aggregates on the nanoparticles from the free proteins in solution. The presence of trehalose in protein-nanoparticle solution shows lesser changes in the intensities of the transverse and the longitudinal plasmon modes and shows a trend when the trehalose concentration is increased from 0 to 0.05 M and 0.5 M. There can be two possible reasons for the observation of this behavior. Firstly, as seen from the fluorescence measurements, the reduction in binding of protein to the silver nanoparticles, as evident from the reduced binding constants, decreases the formation of the seeds for the aggregation of protein. Secondly, the free proteins in the trehalose containing solution have a reduced tendency to form protein aggregates on the surface of the silver nanoparticles. The UV-vis spectra obtained even after 24 hours of incubation of the protein- nanoparticle solution shows the presence of the presence of the transverse plasmon mode. Whereas in case of the protein-nanoparticle solution without trehalose, there is almost total reduction of transverse plasmon mode indicates complete aggregation of the protein-nanoparticle conjugates. Even 1 M sucrose, concentration higher than that of the maximum concentration of trehalose used showed decrease in the transverse plasmonic mode (Figure 7.4). The presence of a higher concentration of sucrose could not prevent the aggregation of the protein-nanoparticle conjugate. Thus, trehalose is more effective in prevention of aggregation, more than any other sugar.

7.3.4 SERS studies

SERS can detect minute structural changes on adsorbtion of proteins to nanoparticles surface. The SERS spectrum of lysozyme is dominated by modes from aromatic amino acids Phe, Tyr, Trp, His as well as amide mode vibrations and backbone vibrations. SERS is a surface sensitive technique where the appearance and the intensity of the modes of the protein is governed by the orientation of the proteins to the surface of the nanoparticle. Figure 7.5 shows the SERS spectra of lysozyme in presence and absence of trehalose. SERS spectra of lysozyme could be obtained in 0.05 M trehalose solution. But in case of 0.5 M trehalose solution, we observed very weak modes and the prominent modes from protein was not observed. SERS spectra in 0.05 M trehalose aqueous solution showed some significant differences as compared to the spectra acquired in the absence of tre-

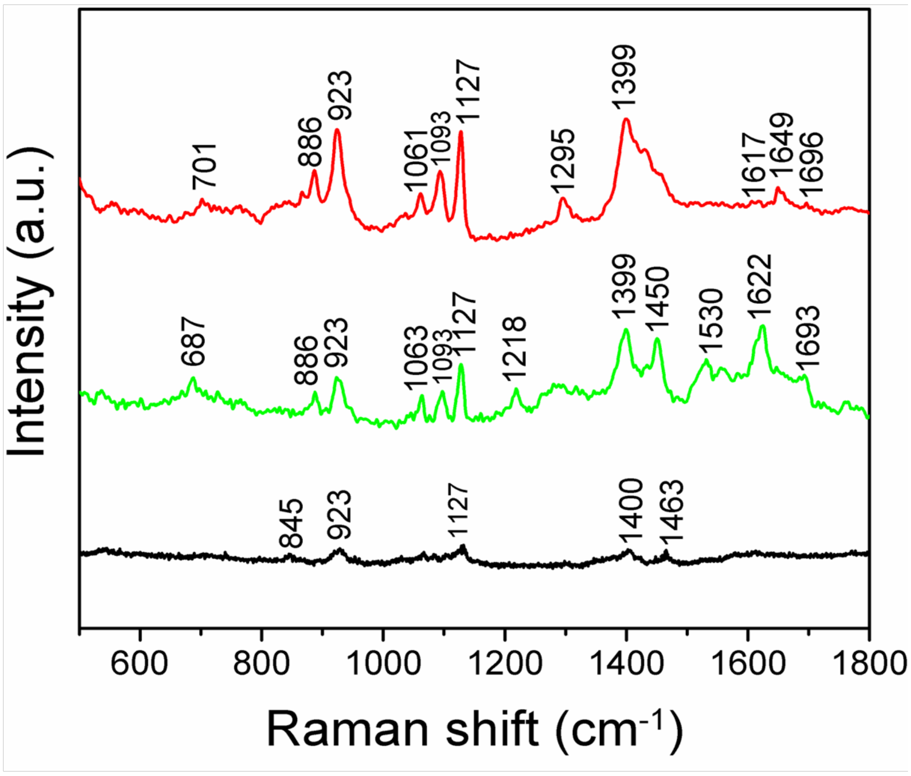

Figure 7.5: SERS spectrum of Lysozyme (red), lysozyme in the presence of 0.05M trehalose (green) and lysozyme in the presence of 0.5M trehalose (black).

halose. The most prominent difference is in the amide I and III regions. In the absence of trehalose, the amide I and III are located at 1649 and 1295 cm^{-1} respectively which corresponds to α-helix. The C-C stretching vibration of α-helix is located at 924 cm^{-1}. The presence of these modes indicates that lysozyme is attached to the surface of the silver nanoparticle through the α-helical domain. But in case of SERS of lysozyme in the presence of 0.05 M trehalose, the amide I peak is located at 1624 cm^{-1} with a higher wavenumber component at 1693 cm^{-1}. This splitting of amide I peak is usually observed in case of antiparallel β-sheets. This is further supported by the observation of amide III band at 1218 cm^{-1}. The peaks at 1532 and 1556 cm^{-1} corresponding to indole ring stretching modes. The observation of these modes in the presence of trehalose indicated the difference in the binding of lysozyme to the surface of the silver nanoparticle. Therefore at 0.05 M trehalose concentration in aqueous medium, the attachment of the protein to the nanoparticles surface shifts from α-helical to β-sheet site.

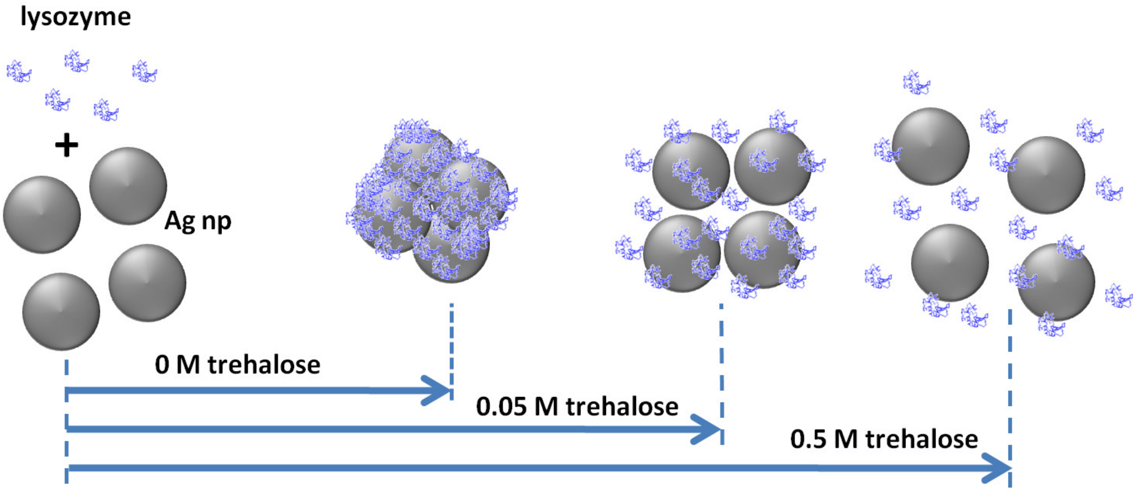

Figure 7.6: Schematic showing the effect of trehalose on protein-nanoparticle aggregation

7.3.5 Significance of protein-nanoparticle conjugate stability

The modulation of aggregation of lysozyme by trehalose is shown in the schematic in Figure 7.6. Although nanoparticles have potential for a vast number of applications in the field of biology and medicine, the adverse effects on protein structure is a major disadvantage and limits its applications. It had been known earlier that nanoparticles produce fibril formations in-vivo. But it has also been shown that under in-vitro conditions, nanoparticles have the ability to form extended aggregates of partially denatured proteins. Our aim has been to create a condition in which the nanoparticles and the proteins co-exist together without having effect on protein structure. This is crucial as it has implications in the field of drug delivery and other applications. In areas of analytical chemistry too it has

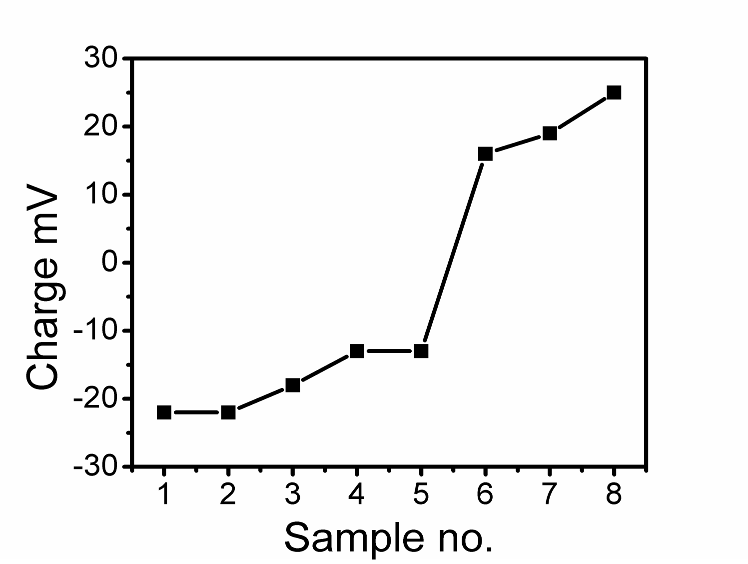

Figure 7.7: Zeta potential measurements on protein-nanoparticle conjugates. Samples 1-8 corresponds to a nanoparticle: protein molar ratio of 10^5:1, 10^4:1, 10^3:1, 10^2:1, 10:1, 1:1, 1:10, 1:10^2 and 1:10^3 respectively.

major repercussions. For instance, SERS applications has been very limited in case of proteins, although it is being used widely in a wide range of areas. Therefore, the ability of trehalose to modulate the protein-nanoparticle interaction provides hope in this area. We see that at higher trehalose concentrations, the interaction between protein and nanoparticles can be reduced to a great extent. This concentration used is lesser than that of other sugar molecules used to bring about similar effects. But, in case of sucrose we see that even at double the maximum concentration of trehalose, it fails to prevent protein-nanoparticle aggregation. This work also shows that at appropriate concentrations, the proteins can actually interact with the nanoparticles without undergoing major structural changes. This fact is confirmed by SERS studies, which provides the information about structure of protein and the specific attachment on the nanoparticle.

The concentration of proteins over the nanoparticle surface is also an important factor for the formation of stable protein- nanoparticle aggregates. Since, electrostatic attachment is the normal way the proteins attach to the nanoparticles, there is a tendency of the system to aggregate on its own. Therefore, it is difficult to distinguish between the protein induced aggregation or purely charge induced aggregation. For this reason, a zeta-potential study was conducted for protein-nanoparticle conjugates at different molar ratios to see the net charge of these aggregates (see Figure 7.7). The negative charge on the nanoparticles is maintained till a nanoparticle-protein ratio of 1:1 after that there is a charge reversal of the entire conjugate. At ratio very close to 1:1, there is a possibility of charge induced aggregation, due to the neutralization of negative charge of the nanoparticle by the protein molecules. Thus for our experiments we have used a ratio of 100:1. At this concentration, the nanoparticle is well dispersed in the solution and has a net negative charge. We have avoided net positively charged aggregates as crowding of proteins on the nanoparticles surface might lead to denaturation. From the flourescence quenching experiments and the UV-vis spectroscopic studies, it is evident that trehalose can control the aggregation of the protein-nanoparticle system.

7.4 Conclusion

Thus, we have shown a possible method for preventing the degradation of a protein system from the stress induced by nanoparticles by using a protein stabilizer. The lysozyme-Ag nanoparticle interaction was studies by using circular dichroism, UV-vis spectroscopy, flourescence quenching eperiments and SERS. It was shown that the protein-nanoparticle system can be stabilized by the introduction of trehalose, which is an exceptional protein stabilizer both at dry and aqueous states. Ag nanoparticles induces aggregation of proteins like lysozyme by the formation of extended aggregates from partially denatured proteins on the surface of the nanoparticles. The prevention of this aggregation behaviour is due to the reduced interaction of lysozyme with the silver nanoparticles at high concentration of trehalose. Even at a lower concentration of trehalose, when there is considerable attachment of protein to the nanoparticle, the structure of the protein is considerably conserved, as seen from the CD experiments. This is an optimum concentration of trehalose which retains the structure of the protein and gives SERS spectra of the protein.This work provides a method of preventing nanoparticle induced protein aggregation for assisting in applications such as use in drug delivery applications as well as in analytical techniques like SERS.

*Note: The equation 7.1 is applicable in cases where the buried fluorophore is not quenched. But in case of binding-related quenching, the fraction of accessible fluorophores is rather an indication of how much fluorescence may be quenched upon full attachment of the quencher to the protein. The different tryptophan residues (for eg. 6 in case of lysozyme) may be quenched by different degrees and does not necessarily reflect how many Trp residues are involved in binding. There are also other detrimental factors like inner-filter effect due to excessive concentration, scattering of light from nanoparticles etc. These factors affect the calculated parameters from this equation and hence may not be relevant for binding related quenching.

CHAPTER 8

OUTLOOK

The emerging optical spectroscopic techniques have provided us new ways to look into nanosytems. Techniques like SERS, surface plasmon resonance (SPR), fluorescence resonance transfer (FRET) have enabled us to probe into molecules at extremely low concentrations with high resolutions and sensitivity. These techniques have achieved the distinction of single molecular level detection. Also, many of these optical techniques are being coupled with other versatile and sensitive techniques like AFM (for example, tip enhanced Raman spectroscopy (TERS)) to extract topological as well as chemical information from molecular systems. These techniques can now be customized for probing delicate biological systems and study their dynamics at physiological conditions. Techniques like SERS, which provide vibrational as well as chemical information, can therefore be used to address challenging problems posed before the biological science community.

One such problems is to find new techniques and new tools for detecting and characterizing protein-small molecule interactions. Although different techniques like SPR, fluorescence, NMR and x-ray crystallography are available for this purpose, they have their own limitations. Any new technique which can complement the above mentioned techniques and thus help in protein-molecule binding studies at ultra-low concentrations, at low volumes and also at physiological conditions can be really advantageous.

SERS, with its unique capability of being able to probe molecules at very low concentrations, low volumes, in aqueous environments. It can provide vibrational and chemical information about molecular systems and can be tailored for analytical technique which becomes a goldmine for biologists. This thesis has demonstrated that it is possible to study protein-ligand interations at much lower concentration than other techniques like x-ray crystallography and NMR. Raman spectroscopy provides information about the secondary structure of proteins and the relative abundance of different amino acids present in the protein. SERS being a surface sensitive technique provides information from those regions which are very close to the surface of the plasmonic nanoparticles. The limited information obtained from SERS can be utilized to derive important information about the protein without complete Raman mode analysis. The most prominent modes observed in SERS are the amide modes which are the combination modes of C=O and N-H bonds and are very sensitive to the secondary structures of proteins. Surface selection rules play an important role as different modes can be present or absent in the spectrum depending on their orientation with respect to the nanoparticle surface. This surface sensitive information can be effectively used for deducing small molecule binding to proteins by considering two different scenarios. Firstly, the bound ligand might shift certain residues away from the nanoparticle surface obscuring these modes. A few modes of the ligand might be seen in the spectra. Secondly, the bound ligand might change the orientation of the protein completely on the surface of the nanoparticle. This is due to the fact that the binding of the protein to the nanoparticle surface is governed by electrostatic as well as hydrophobic/hydrophilic interactions which might be altered due to ligand binding. A preliminary knowledge of the structure of the protein greatly helps in the understanding of the protein interactions at very low concentrations and with high sensitivity in their active state.

Although the surface information obtained from SERS studies can be helpful to elucidate information regarding ligand binding, it might also prove to be detrimental as the ligand might bind in interior pockets of the proteins. This might be a problem and can lead to false negatives unless the active site and its distance from the solvent exposed surface are taken into consideration. But with a detailed knowledge about the structure of protein and its active site and an idea about the site of attachment of protein to the nanoparticle, these issues can be adequately addressed. Also, attachment of proteins to nanoparticles is also a challenge. If they are oppositely charged, leads to electrostatic attachment, the most convenient technique. Otherwise, in case of similar charges, other methods like salt aggregation or chemical functionalization can be used. Another important problem that has to be addressed is the structural alterations of the proteins on interaction with the surface of the nanoparticles. Checking the activity of these protein-nanoparticle composites biochemically is an important step to see whether it can be used for SERS studies. In case of denaturation of proteins by nanoparticles, protein stabilizers like trehalose can be used to preserve the structure of the protein.

Thus, we see that SERS is a technique of enormous potential in the field of biological sciences and therefore needs to be investigated more rigorously in a variety of systems. Along with in-vitro studies of biological systems using SERS, in-vivo studies for Raman imaging of sub-cellular components present interesting areas of research. Rational design of nanostructures with high enhancement factors for direct or targeted detection inside the body of organisms can help us to achieve a better understanding of biological systems.

Thus, this thesis is concluded on a positive note that optical probe techniques like SERS have huge potential in the field of biology. There is still a void of knowledge in this field and a few small steps have already been taken to open new avenues of scientific knowledge and research.

References

[1] L. Rayleigh, *XXXIV. On the transmission of light through an atmosphere containing small particles in suspension, and on the origin of the blue of the sky*, Philosophical Magazine Series 5 **47**, 375 (1899).

[2] A. Smekal, *Zur Quantentheorie der Dispersion*, Naturwissenschaften **11**, 873 (1923).

[3] C. Raman and K. Krishnan, *A new type of secondary radiation*, Nature **121**, 501 (1928).

[4] G. S. Landsberg and L. I. Mandelstam, *Eine neue Erscheinung bei der Lichtzerstreuung in Krystallen*, Naturwissenschaften **16**, 557 (1928).

[5] C. Raman, *A Change of Wave-length in Light Scattering*, Nature **121**, 619 (1928).

[6] G. Placzek, *Quantenmechanik der Strahlung* (Akademische Verlagsgesellschaft mbH, Leipzig, 1934).

[7] P. A. M. Dirac, *The Quantum Theory of the Emission and Absorption of Radiation*, Proceedings of the Royal Society of London. Series A **114**, 243 (1927).

[8] H. Kramers and W. Heisenberg, *Über die Streuung von Strahlung durch Atome*, Zeitschrift für Physik **31**, 681 (1925).

[9] M. Fleischmann, P. Hendra, and A. McQuillan, *Raman spectra of pyridine adsorbed at a silver electrode*, Chemical Physics Letters **26**, 163 (1974).

[10] M. G. Albrecht and J. A. Creighton, *Anomalously intense Raman spectra of pyridine at a silver electrode*, Journal of the American Chemical Society **99**, 5215 (1977).

[11] D. L. Jeanmaire and R. P. V. Duyne, *Surface raman spectroelectrochemistry: Part I. Heterocyclic, aromatic, and aliphatic amines adsorbed on the anodized silver electrode*, Journal of Electroanalytical Chemistry and Interfacial Electrochemistry **84**, 1 (1977).

[12] P. L. Stiles, J. A. Dieringer, N. C. Shah, and R. P. Van Duyne, *Surface-Enhanced Raman Spectroscopy*, Annual Review of Analytical Chemistry **1**, 601 (2008).

[13] E. J. Zeman and G. C. Schatz, *An accurate electromagnetic theory study of surface enhancement factors for silver, gold, copper, lithium, sodium, aluminum, gallium, indium, zinc, and cadmium*, The Journal of Physical Chemistry **91**, 634 (1987).

[14] K. Kneipp *et al.*, *Single Molecule Detection Using Surface-Enhanced Raman Scattering (SERS)*, Phys. Rev. Lett. **78**, 1667 (1997).

[15] S. Nie and S. R. Emory, *Probing Single Molecules and Single Nanoparticles by Surface-Enhanced Raman Scattering*, Science **275**, 1102 (1997).

[16] A. Campion and P. Kambhampati, *Surface-enhanced Raman scattering*, Chem. Soc. Rev. **27**, 241 (1998).

[17] S. Siddhanta and C. Narayana, *Surface Enhanced Raman Spectroscopy of Proteins: Implications in Drug Designing*, Nanotechnology and Nanomaterials **2:1**, (2012).

[18] M. N. Siamwiza *et al.*, *Interpretation of the doublet at 850 and 830 cm-1 in the Raman spectra of tyrosyl residues in proteins and certain model compounds*, Biochemistry **14**, 4870 (1975).

[19] S. Krimm and J. Bandekar, *Vibrational spectroscopy and conformation of peptides, polypeptides and proteins*, Advanced Protein Chemistry **38**, 181 (1986).

[20] A. Barth and C. Zscherp, *What vibrations tell about proteins*, Quarterly reviews of biophysics **35**, 369 (2002).

[21] M. Moskovits and J. S. Suh, *Surface selection rules for surface-enhanced Raman spectroscopy: calculations and application to the surface-enhanced Raman spectrum of phthalazine on silver*, The Journal of Physical Chemistry **88**, 5526 (1984).

[22] G. Pavan Kumar and C. Narayana, *Adapting a fluorescence microscope to perform surface enhanced Raman spectroscopy*, Current Science **93**, 778 (2007).

[23] P. C. Lee and D. Meisel, *Adsorption and surface-enhanced Raman of dyes on silver and gold sols*, The Journal of Physical Chemistry **86**, 3391 (1982).

[24] M.-E. Aubin-Tam and K. Hamad-Schifferli, *Structure and function of nanoparticle–protein conjugates*, Biomedical Materials **3**, 034001 (2008).

[25] A. Hédoux, Y. Guinet, and L. Paccou, *Analysis of the Mechanism of Lysozyme Pressure Denaturation from Raman Spectroscopy Investigations, and Comparison with Thermal Denaturation*, The Journal of Physical Chemistry B **115**, 6740 (2011).

[26] D. Kurouski *et al.*, *Amide I vibrational mode suppression in surface (SERS) and tip (TERS) enhanced Raman spectra of protein specimens*, Analyst **138**, 1665 (2013).

[27] J. Fu, M. Bian, Q. Jiang, and C. Zhang, *Roles of Aurora Kinases in Mitosis and Tumorigenesis*, Molecular Cancer Research **5**, 1 (2007).

[28] M. Carmena and W. C. Earnshaw, *The cellular geography of Aurora Kinases*, Nature Reviews Molecular Cell Biology **4**, 842 (2003).

[29] D. Karthigeyan *et al.*, *Biology of Aurora A kinase: Implications in cancer manifestation and therapy*, Medicinal Research Reviews **31**, 757 (2011).

[30] G. M. T. Cheetham *et al.*, *Crystal Structure of Aurora-2, an Oncogenic Serine/Threonine Kinase*, Journal of Biological Chemistry **277**, 42419 (2002).

[31] J. R. Pollard and M. Mortimore, *Discovery and Development of Aurora Kinase Inhibitors as Anticancer Agents*, Journal of Medicinal Chemistry **52**, 2629 (2009).

[32] A. O. Walter *et al.*, *The mitotic serine/threonine kinase Aurora2/AIK is regulated by phosphorylation and degradation*, Oncogene **19**, 4906 (2000).

[33] H. Ma, S. Deacon, and K. Horiuchi, *The challenge of selecting protein kinase assays for lead discovery optimization*, Expert opinion on Drug Discovery **3**, 607 (2009).

[34] K. Luger *et al.*, *Crystal structure of the nucleosome core particle at 2.8A resolution*, Nature **389**, 251 (1997).

[35] L. Calzolai, F. Franchini, D. Gilliland, and F. Rossi, *ProteinNanoparticle Interaction: Identification of the UbiquitinGold Nanoparticle Interaction Site*, Nano Letters **10**, 3101 (2010).

[36] J. M. Elkins, S. Santaguida, A. Musacchio, and S. Knapp, *Crystal Structure of Human Aurora B in Complex with INCENP and VX-680*, Journal of Medicinal Chemistry **55**, 7841 (2012).

[37] H. Deng *et al.*, *The study of Turnip Mosaic virus coat protein by surface enhanced Raman spectroscopy*, Spectrochimica Acta Part A: Molecular Spectroscopy **49**, 1709 (1993).

[38] K. Kneipp *et al.*, *Surface-enhanced Raman scattering and biophysics*, Journal of Physics: Condensed Matter **14**, R597 (2002).

[39] S. Stewart and P. Fredericks, *Surface-enhanced Raman spectroscopy of peptides and proteins adsorbed on an electrochemically prepared silver surface*, Spectrochimica Acta Part A: Molecular and Biomolecular Spectroscopy **55**, (1999).

[40] S. Siddhanta *et al.*, *Surface enhanced Raman spectroscopy of Aurora kinases: direct, ultrasensitive detection of autophosphorylation*, RSC Adv. **3**, 4221 (2013).

[41] E. Podstawka, Y. Ozaki, and L. M. Proniewicz, *Part I: Surface-Enhanced Raman Spectroscopy Investigation of Amino Acids and Their Homodipeptides Adsorbed on Colloidal Silver*, Applied Spectroscopy **58**, 570 (2004).

[42] M. P. Eastwood, C. Hardin, Z. Luthey-Schulten, and P. Wolynes, *Evaluating protein structure-prediction schemes using energy landscape theory*, IBM Journal of Research and Development **45**, 475 (2001).

[43] L. Ashton, C. Johannessen, and R. Goodacre, *The Importance of Protonation in the Investigation of Protein Phosphorylation Using Raman Spectroscopy and Raman Optical Activity*, Analytical Chemistry **83**, 7978 (2011).

[44] L. Chen *et al.*, *Synchrotron Infrared Measurements of Protein Phosphorylation in Living Single PC12 Cells during Neuronal Differentiation*, Analytical Chemistry **84**, 4118 (2012).

[45] T. T. Chen, C. S. Kuo, Y. C. Chou, and N. T. Liang, *Surface-enhanced Raman scattering of adenosine triphosphate molecules*, Langmuir **5**, 887 (1989).

[46] K. Mantelingu *et al.*, *Activation of p300 Histone Acetyltransferase by Small Molecules Altering Enzyme Structure: Probed by Surface-Enhanced Raman Spectroscopy*, The Journal of Physical Chemistry B **111**, 4527 (2007).

[47] A. D. MacKerell *et al.*, *All-Atom Empirical Potential for Molecular Modeling and Dynamics Studies of Proteins*, The Journal of Physical Chemistry B **102**, 3586 (1998).

[48] A. D. Mackerell, M. Feig, and C. L. Brooks, *Extending the treatment of backbone energetics in protein force fields: Limitations of gas-phase quantum mechanics in reproducing protein conformational distributions in molecular dynamics simulations*, Journal of Computational Chemistry **25**, 1400 (2004).

[49] W. L. Jorgensen *et al.*, *Comparison of simple potential functions for simulating liquid water*, The Journal of Chemical Physics **79**, 926 (1983).

[50] T. Darden, D. York, and L. Pedersen, *Particle mesh Ewald: An N [center-dot] log(N) method for Ewald sums in large systems*, The Journal of Chemical Physics **98**, 10089 (1993).

[51] J.-P. Ryckaert, G. Ciccotti, and H. J. Berendsen, *Numerical integration of the cartesian equations of motion of a system with constraints: molecular dynamics of n-alkanes*, Journal of Computational Physics **23**, 327 (1977).

[52] G. M. Morris *et al.*, *AutoDock4 and AutoDockTools4: Automated docking with selective receptor flexibility*, Journal of Computational Chemistry **30**, 2785 (2009).

[53] M. F. Sanner, *Python: a programming language for software integration and development.*, Journal of molecular graphics & modelling **17**, 57 (1999).

[54] G. M. Morris *et al.*, *Automated docking using a Lamarckian genetic algorithm and an empirical binding free energy function*, Journal of Computational Chemistry **19**, 1639 (1998).

[55] J. C. Phillips *et al.*, *Scalable molecular dynamics with NAMD*, Journal of Computational Chemistry **26**, 1781 (2005).

[56] W. Humphrey, A. Dalke, and K. Schulten, *VMD: Visual molecular dynamics*, Journal of Molecular Graphics **14**, 33 (1996).

[57] M. J. Frisch *et al.*, *Gaussian 03, Revision C.02*, , Gaussian, Inc., Wallingford, CT, 2004.

[58] X. Xu *et al.*, *Two TPX2-Dependent Switches Control the Activity of Aurora A*, PLoS ONE **6**, e16757 (2011).

[59] S. L. Berger, *Histone modifications in transcriptional regulation*, Current Opinion in Genetics and Development **12**, 142 (2002).

[60] N. C. Cross, *Histone modification defects in developmental disorders and cancer*, Oncotarget **2**, 1127 (2011).

[61] A. J. Bannister and T. Kouzarides, *The CBP co-activator is a histone acetyltransferase*, Nature **384**, 641 (1996).

[62] V. V. Ogryzko *et al.*, *The Transcriptional Coactivators p300 and CBP Are Histone Acetyltransferases*, Cell **87**, 953 (1996).

[63] H. M. Chan and N. B. La Thangue, *p300/CBP proteins: HATs for transcriptional bridges and scaffolds*, Journal of Cell Science **114**, 2363 (2001).

[64] A. Giordano and M. L. Avantaggiati, *p300 and CBP: Partners for life and death*, Journal of Cellular Physiology **181**, 218 (1999).

[65] R. H. Goodman and S. Smolik, *CBP/p300 in cell growth, transformation, and development*, Genes and Development **14**, 1553 (2000).

[66] N. G. Iyer, h. Ozdag, and C. Caldas, *p300/CBP and cancer*, Oncogene **23**, 4225 (2004).

[67] C. Das and T. Kundu, *Transcriptional Regulation by the Acetylation of Nonhistone Proteins in Humans - A New Target for Therapeutics*, IUBMB Life **57**, 137 (2005).

[68] M. Delvecchio *et al.*, *Structure of the p300 catalytic core and implications for chromatin targeting and HAT regulation*, Nature structural and molecular biology **20**, 1040 (2013).

[69] K. Mantelingu *et al.*, *Specific Inhibition of p300 HAT Alters Global Gene Expression and Represses HIV Replication*, Chemistry and Biology **14**, 645 (2007).

[70] M. Arif, G. V. P. Kumar, C. Narayana, and T. K. Kundu, *Autoacetylation Induced Specific Structural Changes in Histone Acetyltransferase Domain of p300: Probed by Surface Enhanced Raman Spectroscopy*, The Journal of Physical Chemistry B **111**, 11877 (2007).

[71] M. D. Vasudevarao *et al.*, *Naphthoquinones Mediated Inhibition of Lysine Acetyltransferase KAT3B/p300, Basis for Non-toxic Inhibitor Synthesis*, Journal of Biological Chemistry (2014).

[72] K. C. Ravindra *et al.*, *Inhibition of lysine acetyltransferase KAT3B/ p300 activity by a naturally occurring, hydroxynaphthoquinone, plumbagin.*, Journal of Biological Chemistry (2009).

[73] X. Liu *et al.*, *The structural basis of protein acetylation by the p300/CBP transcriptional coactivator*, Nature 846 (2008).

[74] Schrödinger, LLC, *The PyMOL Molecular Graphics System, Version 1.3r1*, (2010).

[75] G. V. Pavan Kumar *et al.*, *Surface-Enhanced Raman Scattering Studies of Human Transcriptional Coactivator p300*, The Journal of Physical Chemistry B **110**, 16787 (2006).

[76] V. Reipa and J. J. Horvath, *Surface-Enhanced Raman Study of Benzylpenicillin*, Appl. Spectrosc. **46**, 1009 (1992).

[77] R. Petry, M. Schmitt, and J. Popp, *Raman Spectroscopy—A Prospective Tool in the Life Sciences*, ChemPhysChem **4**, 14 (2003).

[78] P. Matousek, *Deep non-invasive Raman spectroscopy of living tissue and powders*, Chem. Soc. Rev. **36**, 1292 (2007).

[79] P. R. Carey, *Raman Spectroscopy, the Sleeping Giant in Structural Biology, Awakes*, Journal of Biological Chemistry **274**, 26625 (1999).

[80] G. J. Thomas, *Raman spectroscopy of protein and nucleic acid assemblies*, Annual Review of Biophysics and Biomolecular Structure **28**, 1 (1999).

[81] R. Tuma, *Raman spectroscopy of proteins: from peptides to large assemblies*, Journal of Raman Spectroscopy **36**, 307 (2005).

[82] B. M. Bussian and C. Sander, *How to determine protein secondary structure in solution by Raman spectroscopy: practical guide and test case DNase I*, Biochemistry **28**, 4271 (1989).

[83] P. R. Carey and J. Dong, *Following Ligand Binding and Ligand Reactions in Proteins via Raman Crystallography*, Biochemistry **43**, 8885 (2004).

[84] B. P. Danysh and M. K. Duncan, *The lens capsule*, Experimental Eye Research **88**, 151 (2009).

[85] H. V. Gimbel and T. Neuhann, *Development, advantages, and methods of the continuous circular capsulorhexis technique*, Journal of Cataract and Refractive Surgery **16**, 31 (1990).

[86] m. S. R. Jardeleza *et al.*, *Effect of trypan blue staining on the elastic modulus of anterior lens capsules of diabetic and nondiabetic patients*, Journal of Cataract and Refractive Surgery **35**, 318 (2009).

[87] G. R. J. Melles, P. W. T. de Waard, J. H. Pameyer, and W. H. Beekhuis, *Trypan blue capsule staining to visualize the capsulorhexis in cataract surgery*, Journal of Cataract and Refractive Surgery **25**, 7 (1999).

[88] A. J. Singh *et al.*, *A histological analysis of lens capsules stained with trypan blue for capsulorrhexis in phacoemulsification cataract surgery*, Eye **17**, 567 (2003).

[89] H. B. Dick, S. E. Aliyeva, and F. Hengerer, *Effect of trypan blue on the elasticity of the human anterior lens capsule*, Journal of Cataract and Refractive Surgery **34**, 1367 (2008).

[90] N. R. Rangaraj, M. Ariga, and J. Thomas, *Comparison of anterior capsule electron microscopy findings with and without trypan blue staining*, Journal of Cataract and Refractive Surgery **30**, 2241 (2004).

[91] R. Jaber *et al.*, *Comparison of capsulorhexis resistance to tearing with and without trypan blue dye using a mechanized tensile strength model*, Journal of Cataract and Refractive Surgery **38**, 507 (2012).

[92] G. Wollensak, E. Sporl, and D.-T. Pham, *Biomechanical changes in the anterior lens capsule after trypan blue staining*, Journal of Cataract and Refractive Surgery **30**, 1526 (2004).

[93] S. Fukushi and R. G. Spiro, *The Lens Capsule: Sugar and amino acid composition*, Journal of Biological Chemistry **244**, 2041 (1969).

[94] Y. Wang and P. Spencer, *Analysis of acid-treated dentin smear debris and smear layers using confocal Raman microspectroscopy*, Journal of Biomedical Materials Research **60**, 300 (2002).

[95] I. A. Karampas, M. G. Orkoula, and C. G. Kontoyannis, *A quantitative bioapatite/collagen calibration method using Raman spectroscopy of bone*, Journal of Biophotonics **6**, 573 (2013).

[96] J. J. Cárcamo *et al.*, *Raman study of the shockwave effect on collagens*, Spectrochimica Acta Part A: Molecular and Biomolecular Spectroscopy **86**, 360 (2012).

[97] Y. Xiao *et al.*, *Wavelength-Dependent Conformational Changes in Collagen after Mid-Infrared Laser Ablation of Cornea*, Biophysical Journal **94**, 1359 (2008).

[98] A. N. Anigbogu, A. C. Williams, B. W. Barry, and H. G. Edwards, *Fourier transform raman spectroscopy of interactions between the penetration enhancer dimethyl sulfoxide and human stratum corneum*, International Journal of Pharmaceutics **125**, 265 (1995).

[99] R. Kalluri, *Basement membranes: structure, assembly and role in tumour angiogenesis*, nature Reviews Cancer **3**, 422 (2003).

[100] Z.-M. Zhang *et al.*, *An intelligent background-correction algorithm for highly fluorescent samples in Raman spectroscopy*, Journal of Raman Spectroscopy **41**, 659 (2010).

[101] T. T. Nguyen *et al.*, *Characterization of Type I and IV COllagens by Raman Microspectroscopy: Identification of Spectral Markers of the Dermo-Epidermal Junction*, Spectroscopy: An International Journal **27**, 421 (2012).

[102] N. C. Maiti *et al.*, *Raman Spectroscopic Characterization of Secondary Structure in Natively Unfolded Proteins: -Synuclein*, Journal of the American Chemical Society **126**, 2399 (2004).

[103] G. Anderle and R. Mendelsohn, *Thermal denaturation of globular proteins. Fourier transform-infrared studies of the amide III spectral region*, Biophysical Journal **52**, 69 (1987).

[104] B. G. Frushour and J. L. Koenig, *Raman scattering of collagen, gelatin, and elastin*, Biopolymers **14**, 379 (1975).

[105] T. Ikoma *et al.*, *Physical properties of type I collagen extracted from fish scales of Pagrus major and Oreochromis niloticas*, International Journal of Biological Macromolecules **32**, 199 (2003).

[106] J. J. Carcamo *et al.*, *Proline and hydroxyproline deposited on silver nanoparticles. A Raman, SERS and theoretical study*, Journal of Raman Spectroscopy **43**, 750 (2012).

[107] N. Nogami, H. Sugeta, and T. Miyazawa, *C-S Stretching Vibrations and Molecular Conformations of Isobutyl Methyl Sulfide and Related Alkyl Sulfides*, Bulletin of the Chemical Society of Japan **48**, 2417 (1975).

[108] M. Jastrzebska *et al.*, *Raman spectroscopic study of glutaraldehyde-stabilized collagen and pericardium tissue*, Journal of Biomaterials Science, Polymer Edition **14**, 185 (2003).

[109] G. R. Buettner and R. D. Hall, *Superoxide, hydrogen peroxide and singlet oxygen in hematoporphyrin derivative-cysteine, -NADH and -light systems*, Biochimica et Biophysica Acta (BBA) - General Subjects **923**, 501 (1987).

[110] N. T. Yu and E. J. East, *Laser Raman spectroscopic studies of ocular lens and its isolated protein fractions.*, Journal of Biological Chemistry **250**, 2196 (1975).

[111] I. Siebinga *et al.*, *Ageing and changes in protein conformation in the human lens: A Raman microspectroscopic study*, Experimental Eye Research **54**, 759 (1992).

[112] F. N. R. Petersen and C. H. Nielsen, *Raman Spectroscopy as a Tool for Investigating Lipid-Protein Interactions*, Spectroscopy **24**, 1 (2009).

[113] H. Feit, M. Kawai, and A. S. Mostafapour, *The role of collagen crosslinking in the increased stiffness of avian dystrophic mucle*, Muscle and Nerve **12**, 486 (1989).

[114] N. Verzijl *et al.*, *Crosslinking by advanced glycation end products increases the stiffness of the collagen network in human articular cartilage: A possible mechanism through which age is a risk factor for osteoarthritis*, Arthritis and Rheumatism **46**, 114 (2002).

[115] M. G. Glogowska *et al.*, *Structural alteration of collagen fibres - spectroscopic and mechanical studies*, Acta of Bioengineering and Biomechanics **Vol. 12, nr 4**, 55 (2010).

[116] H. Yetik, K. Devranoglu, and S. Ozkan, *Determining the lowest trypan blue concentration that satisfactorily stains the anterior capsule*, Journal of Cataract and Refractive Surgery **28**, 988 (2002).

[117] O. C. Farokhzad and R. Langer, *Impact of Nanotechnology on Drug Delivery*, ACS Nano **3**, 16 (2009).

[118] O. Veiseh, J. W. Gunn, and M. Zhang, *Design and fabrication of magnetic nanoparticles for targeted drug delivery and imaging*, Advanced Drug Delivery Reviews **62**, 284 (2010), targeted Delivery Using Inorganic Nanosystem.

[119] F. T. Docherty *et al.*, *Multiple labelled nanoparticles for bio detection*, Faraday Discuss. **126**, 281 (2004).

[120] N. L. Rosi and C. A. Mirkin, *Nanostructures in Biodiagnostics*, Chemical Reviews **105**, 1547 (2005).

[121] S. S. Bale *et al.*, *Nanoparticle-Mediated Cytoplasmic Delivery of Proteins To Target Cellular Machinery*, ACS Nano **4**, 1493 (2010).

[122] J. Ellenberg, J. Lippincott-Schwartz, and J. F. Presley, *Dual-colour imaging with {GFP} variants*, Trends in Cell Biology **9**, 52 (1999).

[123] J. A. Maynard *et al.*, *Surface plasmon resonance for high-throughput ligand screening of membrane-bound proteins*, Biotechnology Journal **4**, 1542 (2009).

[124] X. Han, B. Zhao, and Y. Ozaki, *Surface-enhanced Raman scattering for protein detection*, Analytical and Bioanalytical Chemistry **394**, 1719 (2009).

[125] H. Pan *et al.*, *How Do Proteins Unfold upon Adsorption on Nanoparticle Surfaces?*, Langmuir **28**, 12779 (2012).

[126] S. Saptarshi, A. Duschl, and A. Lopata, *Interaction of nanoparticles with proteins: relation to bio-reactivity of the nanoparticle*, Journal of Nanobiotechnology **11**, 26 (2013).

[127] S. Laera *et al.*, *Measuring Protein Structure and Stability of Protein–Nanoparticle Systems with Synchrotron Radiation Circular Dichroism*, Nano Letters **11**, 4480 (2011).

[128] K. Imamura, T. Ogawa, T. Sakiyama, and K. Nakanishi, *Effects of types of sugar on the stabilization of protein in the dried state*, Journal of Pharmaceutical Sciences **92**, 266 (2003).

[129] J. K. Kaushik and R. Bhat, *Why Is Trehalose an Exceptional Protein Stabilizer?*, Journal of Biological Chemistry **278**, 26458 (2003).

[130] S. Allison, B. Chang, T. W. Randolph, and J. F. Carpenter, *Hydrogen Bonding between Sugar and Protein Is Responsible for Inhibition of Dehydration-Induced Protein Unfolding*, Archives of Biochemistry and Biophysics **365**, 289 (1999).

[131] S. B. Leslie *et al.*, *Trehalose and sucrose protect both membranes and proteins in intact bacteria during drying.*, Applied and Environmental Microbiology **61**, 3592 (1995).

[132] G. Xie and S. N. Timasheff, *The thermodynamic mechanism of protein stabilization by trehalose*, Biophysical Chemistry **64**, 25 (1997), 10 Years of the Gibbs Conference on Biothermodynamics.

[133] G. Xie and S. N. Timasheff, *Mechanism of the stabilization of ribonuclease a by sorbitol: Preferential hydration is greater for the denatured than for the native protein*, Protein Science **6**, 211 (1997).

[134] T.-Y. Lin and S. N. Timasheff, *On the role of surface tension in the stabilization of globular proteins*, Protein Science **5**, 372 (1996).

[135] S. James and J. J. McManus, *Thermal and Solution Stability of Lysozyme in the Presence of Sucrose, Glucose, and Trehalose*, The Journal of Physical Chemistry B **116**, 10182 (2012).

[136] G. Merlini and V. Bellotti, *Lysozyme: A paradigmatic molecule for the investigation of protein structure, function and misfolding*, Clinica Chimica Acta **357**, 168 (2005).

[137] V. A. Proctor, F. E. Cunningham, and D. Y. C. Fung, *The chemistry of lysozyme and its use as a food preservative and a pharmaceutical*, C R C Critical Reviews in Food Science and Nutrition **26**, 359 (1988).

[138] B. M. Chassy and A. Giuffrida, *Method for the lysis of Gram-positive, asporogenous bacteria with lysozyme.*, Applied and Environmental Microbiology **39**, 153 (1980).

[139] D. Zhang *et al.*, *Gold Nanoparticles Can Induce the Formation of Protein-based Aggregates at Physiological pH*, Nano Letters **9**, 666 (2009).

[140] M. Moskovits, in *Surface-Enhanced Raman Scattering*, Vol. 103 of *Topics in Applied Physics*, edited by K. Kneipp, M. Moskovits, and H. Kneipp (Springer Berlin Heidelberg, , 2006), pp. 1–17.

[141] S. Schlücker, *SERS Microscopy: Nanoparticle Probes and Biomedical Applications*, ChemPhysChem **10**, 1344 (2009).

[142] J. Yguerabide and E. E. Yguerabide, *Light-Scattering Submicroscopic Particles as Highly Fluorescent Analogs and Their Use as Tracer Labels in Clinical and Biological Applications: I. Theory*, Analytical Biochemistry **262**, 137 (1998).

[143] M. Lundqvist, I. Sethson, and B.-H. Jonsson, *Protein Adsorption onto Silica Nanoparticles: Conformational Changes Depend on the Particles' Curvature and the Protein Stability*, Langmuir **20**, 10639 (2004).